



SOUTHWEST AUSTRALIA NETWORK (SWAN): PASSIVE SEISMIC IMAGING AND HAZARD ANALYSIS

RE Murdie and MS Miller (compilers)



Australian
National
University



THE UNIVERSITY OF
WESTERN AUSTRALIA



DFES
Department of Fire &
Emergency Services



Australian Government
Geoscience Australia



Institute of Geology and Geophysics,
Chinese Academy of Sciences



清华大学
Tsinghua University



Department of **Energy, Mines,
Industry Regulation and Safety**

REPORT 255

Southwest Australia Network (SWAN): passive seismic imaging and hazard analysis

RE Murdie and MS Miller (compilers)

PERTH 2024



**Geological Survey of
Western Australia**

MINISTER FOR MINES AND PETROLEUM
Hon David Robert Michael MLA

DIRECTOR GENERAL, DEPARTMENT OF ENERGY, MINES, INDUSTRY REGULATION AND SAFETY
Richard Sellers

EXECUTIVE DIRECTOR, GEOLOGICAL SURVEY AND RESOURCE STRATEGY
Michele Spencer



A catalogue record for this
book is available from the
National Library of Australia

REFERENCE

The recommended reference for the whole publication is:

Murdie, RE and Miller, MS (compilers) 2024, Southwest Australia Network (SWAN): passive seismic imaging and hazard analysis: Geological Survey of Western Australia, Report 255, 77p.

The recommended reference format for a contribution in this publication is:

Murdie, RE, Yuan, H and Pickle, R 2024, SWAN deployment, *in* South West Australia Network: passive seismic imaging and hazard analysis *compiled by* RE Murdie and MS Miller: Geological Survey of Western Australia, Report 255, p. 19–21.

ISBN 978-1-74168-048-5

ISSN 1834-2280

Grid references in this publication refer to the Geocentric Datum of Australia 1994 (GDA94). All locations are quoted to at least the nearest 100 m.



Australian
National
University



THE UNIVERSITY OF
WESTERN AUSTRALIA



Australian Government
Geoscience Australia



Institute of Geology and Geophysics,
Chinese Academy of Sciences



清华大学
Tsinghua University

Disclaimer

This product uses information from various sources. The Department of Energy, Mines, Industry Regulation and Safety (DEMIRS) and the State cannot guarantee the accuracy, currency or completeness of the information. Neither the department nor the State of Western Australia nor any employee or agent of the department shall be responsible or liable for any loss, damage or injury arising from the use of or reliance on any information, data or advice (including incomplete, out of date, incorrect, inaccurate or misleading information, data or advice) expressed or implied in, or coming from, this publication or incorporated into it by reference, by any person whatsoever.

Acknowledgement of Country

The Department of Energy, Mines, Industry Regulation and Safety (DEMIRS) respectfully acknowledges Aboriginal peoples as being the traditional custodians of Western Australia. We acknowledge the enduring connection Aboriginal people continue to share with the land, sea and sky through both their ancestral ties and custodianship to Country. We pay our respect to Elders both past and present, and acknowledge the value brought to our department through the collective contribution of Aboriginal and Torres Strait Islander peoples across Western Australia.

Published 2024 by the Geological Survey of Western Australia

This Report is published in digital format (PDF) and is available online at <www.demirs.wa.gov.au/GSWApublications>.



© State of Western Australia (Department of Energy, Mines, Industry Regulation and Safety) 2024

With the exception of the Western Australian Coat of Arms and other logos, and where otherwise noted, these data are provided under a Creative Commons Attribution 4.0 International Licence. (<https://creativecommons.org/licenses/by/4.0/legalcode>)

Further details of geoscience products are available from:

First Floor Counter
Department of Energy, Mines, Industry Regulation and Safety
100 Plain Street
EAST PERTH WA 6004
Telephone: +61 8 9222 3459 Email: publications@demirs.wa.gov.au
www.demirs.wa.gov.au/GSWApublications

Cover image: Installing SWN12 station near Brookton

Contents

Southwest Australia Seismic Network (SWAN).....	1
Tectonic units, tectonic setting and seismicity of southwestern Western Australia	4
The seismicity of southwest Western Australia	14
SWAN deployment.....	19
A detailed earthquake catalogue for southwest Australia 2020–23 using data from the SWAN and WA Array networks	22
Centroid moment tensor (CMT) solutions for earthquakes in southwest Australia, enabled by the SWAN network	30
3D V_s model of the Earth's crust in southwest Western Australia from ambient noise tomography	36
Imaging the lithospheric mantle of southwest Western Australia using finite-frequency P-wave tomographic inversion of the SWAN dataset.....	42
P-wave receiver function models from SWAN data	50
Site classification and V_{S30} determination for seismic hazard evaluation in the SWAN seismic network, Western Australia	58
An updated Fourier spectral attenuation model for southwestern Western Australia	68
The importance of contemporary earthquake knowledge to inform emergency management	76

Figures

1. Map of earthquake epicentres for events $M > 2.0$ 1960 to July 2020.....	2
2. Principal tectonic units and geology of southwest Western Australia.....	5
3. Simplified geology and tectonic subdivisions of the southwestern Yilgarn Craton	6
4. Geology and geophysics of southwest Western Australia as data layers	7
5. Geology and tectonic subdivisions of the Albany–Fraser Orogen.....	8
6. Perth Basin stratigraphy	10
7. Earthquakes of southwest Western Australia 2009 to 2020	15
8. Focal mechanisms of selected earthquakes in southwest Western Australia.....	16
9. The Arthur River swarm earthquake locations.....	17
10. Tectonic features surrounding the Australian continent.....	17
11. Location of seismic stations active during the SWAN project.....	20
12. Field photos of SWAN seismometer setup	20
13. Installation of a SmartSolo seismometer at Arthur River site SWNNB	21
14. Map of seismic stations overlain on the Bouguer gravity anomaly map	23
15. Map of located events	25
16. M_{la} magnitude and number of phase picks vs number of events	26
17. M_{la} magnitude distribution vs number of events.....	26
18. Map of located events and algorithmically detected cluster grouping	27
19. Precision map of Arthur River events	28
20. Depth vs time figure of Arthur River events.....	28
21. Frequency distribution of Arthur River events.....	28
22. Earthquake epicentres in southwest Australia 1960 to 2022	31
23. Results of the CMT inversion for Event #1	32
24. Waveform fits for the optimum CMT solution.....	32
25. Depth and double-couple (DC) percentages for five events.....	33
26. Estimated CMT solutions overlain on the region's topography.....	34
27. Seismic stations used for ambient noise tomography.....	37
28. Cross-correlation functions in the time domain for the SWAN stations	37
29. Horizontal slices at depths of 4, 10, 16 and 28 km through the 3D V_s model.....	38
30. Vertical W–E and N–S profiles through the 3D V_s model.....	39
31. Horizontal slices of the checkerboard resolution test.....	40
32. Distribution of seismic stations in southwest Western Australia.....	43
33. Distribution of teleseismic events	44
34. Average crustal P-wave velocity model	44
35. Average crustal correction for stations	44
36. L-curve for select regularization factor.....	45
37. Histograms of relative travel-time residuals	45
38. P-wave tomographic model slices at different depths.....	46
39. P-wave velocity variation cross-sections	47
40. P-wave velocity variations averaged from 70 to 150 km depths	48
41. P-wave velocity variations averaged from 50 to 200 km depths	48
42. SWAN area map and stations used in the receiver function analysis.....	51
43. H- κ stacking for station SWAN03	53
44. H- κ stacking for station SWAN14	53
45. H- κ stacking for station SWAN25	53
46. Common-conversional-point (CCP) stacking ray path coverage.....	54
47. Map views of the average crustal thickness and V_p/V_s ratio	55
48. CCP and V_s variation models along the blue profile	55

49.	CCP and V_s variation models along the green profile.....	56
50.	CCP and V_s variation models for the active-source SW1 line	56
51.	Spatial distribution of estimated V_{s30} values for SWAN seismic stations.....	59
52.	Examples of array geometries used to acquire ambient vibrations	61
53.	Inversion results for station SWN15 to address V_s uncertainty.....	62
54.	Example of HVSR measurement for station SWN24.....	63
55.	Result of shear-wave velocity profile inversion for station SWN24.....	64
56.	HVSR curves for stations without a clear peak in fundamental frequency.....	66
57.	Magnitude–hypocentral distance distribution of the southwest Western Australia dataset	69
58.	Example fit to normalized Fourier spectral amplitude data for 2.0 and 5.0 Hz	70
59.	Fourier acceleration spectra passing signal-to-noise tests	71
60.	Frequency-dependent site-correction terms for representative stations.....	72
61.	Logarithm of residuals (observed – predicted) for 2.0 and 5.0 Hz	73
62.	Comparison of Fourier displacement amplitude models for 0.50 and 5.0 Hz.....	73
63.	Western Australia’s earthquake hazard guidance publications.....	77

Tables

1.	SWAN temporary seismometer installation information	3
2.	M >6 events in Western Australia and other notable earthquakes.....	15
3.	Source parameters of earthquakes in this study.....	33
4.	Frequency bands used for picking seismic-wave travel times	44
5.	Average crustal thickness (H) and V_p/V_s ratio (κ)	52
6.	Seismic site classification in Australia.....	59
7.	Natural frequency and V_{s30} values from geological proxy-based and slope-based inversions	65
8.	Distance to nearest seismometer required for event selection.....	69

Southwest Australia Seismic Network (SWAN)

MS Miller¹, R Pickle¹, RE Murdie, H Yuan, TI Allen², K Gessner, P Zhang¹, S Mousavi¹,
BLN Kennett¹ and J Whitney³

1. Research School of Earth Sciences, The Australian National University, Acton ACT 0200

2. Geoscience Australia, Symonston ACT 2609

3. Department of Fire and Emergency Services, Western Australia (now at Department of Premier and Cabinet, Perth WA 6009)

Abstract

The southwest of Western Australia has had the most earthquakes of any region in continental Australia during the past five decades. To improve our understanding of why this region is so seismically active, a group of scientists from The Australian National University, Geological Survey of Western Australia and Geoscience Australia, in collaboration with the Department of Fire and Emergency Services, deployed a temporary network of seismic instruments for approximately 3.5 years from mid-2020 until late 2023. This Southwest Australia Seismic Network (SWAN) project consisted of a temporary network of 27 broadband seismometers that continuously recorded ground motions from both nearby earthquakes and distant earthquakes. This research is equally critical from a scientific standpoint and from an emergency management standpoint: it aims to increase our knowledge about Earth's evolution and will ultimately lead to enhanced safety, in terms of earthquake hazard, for the Western Australian community.

KEYWORDS: earthquakes, lithosphere imaging, seismic hazard, southwest Australia

Introduction

The Southwest Australia Seismic Network (SWAN) was designed to provide a compilation of 3D models of the crust and lithosphere of southwest Western Australia. This region appears to have a distinct contrast in geophysical properties and also has some of the highest levels of seismicity on the continent (Fig. 1). For example, an M_L 5.7 earthquake was felt widely across the Perth metropolitan area on 16 September 2018 followed by and another slightly smaller M_L 5.3 event on 8 November 2018 both of which originated near Lake Muir. Despite this relatively high seismicity, and the fact that over 90% of the state's population resides within this region, Western Australia has previously had only limited coverage with seismic stations. Seismic monitoring and improved understanding of earthquake hazard is critical to effective emergency management.

The lithosphere of southwestern Australia is dominated by the western margin of the Archean Yilgarn Craton. This margin underwent complex reorganization during the Phanerozoic continental breakup of Gondwana as India and Antarctica broke away from Australia. Despite the currently stable structure, far from active plate boundaries, this southwestern region has been the most seismically active in continental Australia during the past five decades. To improve our understanding of these earthquakes, and to image the three-dimensional (3D) velocity structure of the lithosphere across the region, we deployed a temporary network of seismic instrumentation.

The Southwest Australia Seismic Network (SWAN) consisted of 27 broadband seismometers installed for nearly four years from late 2020 through 2023 (Fig. 1, Table 1). The network was designed to record local earthquakes and

distant earthquakes and was successful in both these objectives. This was essential for better characterization of the location, depth and attenuation of the events, which is important for understanding earthquake hazard. The earthquakes also provided the data source required for imaging of 3D seismic structure in the crust and mantle lithosphere. During the deployment of these instruments, a significant earthquake swarm occurred around the community of Arthur River starting in January 2022. The swarm included five earthquakes of local magnitude 4.0 and larger, and six additional short-term nodal seismometers were rapidly deployed at 11 separate sites in early 2022 to monitor this swarm activity (Fig. 1, Table 1). All waveform data and resulting models are archived online at the Federation of Digital Seismograph Networks Foundation (FDSN) recognized Australian Passive Seismic Data Centre (auspass.edu.au/data.html).

The SWAN experiment was funded by an ARC Linkage grant 'Enhanced 3D Seismic structure for Southwest Australia' Discovery Project LP180101118. It is a result of collaboration between The Australian National University (ANU), Geoscience Australia (GA), the University of Macquarie, the Geological Survey of Western Australia (GSWA) and the Department of Fire and Emergency Services of Western Australia (DFES).

Data and resources

The project uses 24 broadband seismometers and data recorders from the Australian National Seismic Imaging

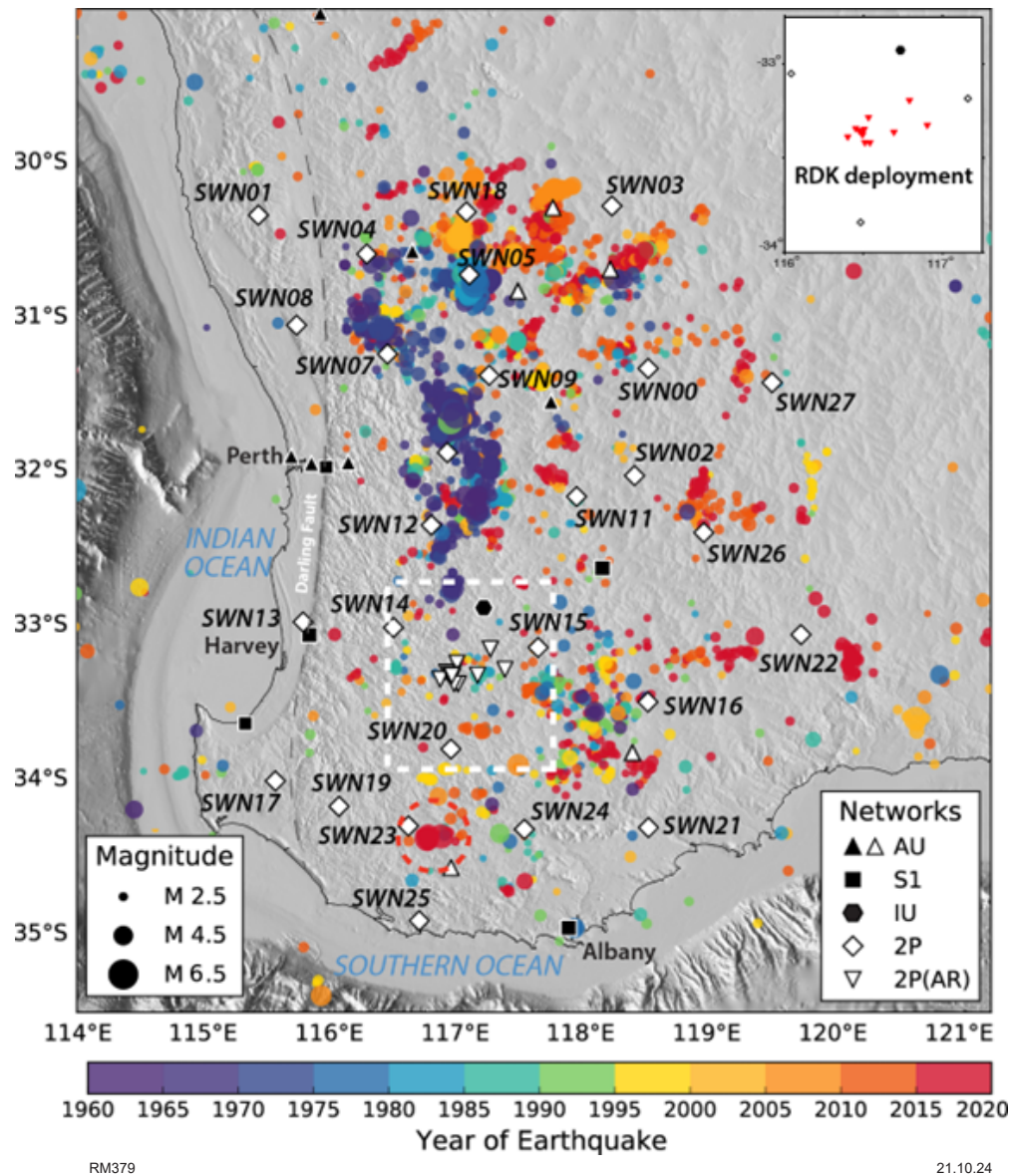


Figure 1. Map of earthquake epicentres for events $M > 2.0$ from 1960 to July 2020 (prior to the deployment of the SWAN instruments) coloured by date and scaled by magnitude. The largest events are superimposed over smaller-magnitude earthquakes. The 17 broadband station locations for the SWAN – 2P network are shown as white diamonds. Other temporary stations in the AU network are also shown as white symbols. Long-term broadband stations currently operating in the region are indicated with black symbols: AU – Australian National Seismic Network (10); S1 – Australian Seismometers in Schools (5); IU – Global Seismograph Network (1); 2P(AR) – Arthur River swarm rapid deployment kits (RDK; 8). The red dashed-line circle indicates the 2018 Lake Muir M_w 5.3 and M_w 5.2 events and associated aftershocks. The white dashed-line rectangle indicates the region of 2022 Arthur River swarm, and RDK deployment locations are shown by red inverted triangles in the inset in the upper right corner of the map

Resource facility (ANSIR; www.auscope.org.au/ansir) pool of instrumentation, and three broadband seismometers from the Geological Survey of Western Australia (GSWA). The rapid deployment kit deployed during the Arthur River swarm used six short period seismometers from GSWA. This project was enabled by AuScope and the Australian Government via the National Collaborative Research Infrastructure Strategy (NCRIS; www.auscope.org.au).

The metadata and waveforms from all the instruments are available from the Australian Passive Seismic Server (AusPass; <https://auspass.edu.au>) as network 2P and will be openly available in December 2025 following the 2-year data embargo (doi:10.7914/SN/2P_2020; www.fdsn.org/networks/detail/2P_2020/).

Uniformly processed engineering ground motion parameters from the moderate-magnitude earthquakes recorded by this network will be made available through a Geoscience Australia online database and mirrored at AusPass. Interested readers may contact the authors for access to the prototype database ahead of its formal release.

Digital models, images and other associated data will be made available through the Department of Energy, Mines, Industry Regulation and Safety (DEMIRS) data server GeoVIEW.WA (www.dmp.wa.gov.au/geoview) in December 2024.

Table 1 SWAN temporary seismometer installation information

Station name	Latitude (deg)	Longitude (deg)	Location	Sensor type	Install date
SWN00	-31.37287	118.49077	Burracoppin, WA	Güralp 6TD	27-Aug-20
SWN01	-30.36867	115.55577	Badgingarra, WA	Trillium Compact 120s Posthole	23-Sep-20
SWN02	-32.06812	118.39443	Narembeen, WA	Güralp 6TD	01-Oct-20
SWN03	-30.32251	118.20749	Bonnie Rock, WA	Trillium Compact 120s Posthole	30-Sep-20
SWN04	-30.63021	116.36565	Bindi Bindi, WA	Trillium Compact 120s	23-Sep-20
SWN05	-30.76903	117.13635	Cadoux, WA	Trillium Compact 120s	30-Sep-20
SWN07	-31.27954	116.51481	Bolgart, WA	Trillium Compact 120s	23-Sep-20
SWN08	-31.08505	115.82961	Red Gully, WA	Trillium Compact 120s	23-Sep-20
SWN09	-31.4215	117.2849	Ynattering, WA	Trillium Compact 120s	30-Sep-20
SWN10	-31.921	116.9642	Green Hills, WA	Trillium Compact 120s	10-Sep-20
SWN11	-32.20588	117.95199	Bilbarin, WA	Trillium Compact 120s Posthole	10-Sep-20
SWN12	-32.38999	116.83852	Brookton, WA	Trillium Compact 120s	18-Sep-20
SWN13	-33.0088	115.8442	Harvey2, WA	Trillium Compact 120s Posthole	28-Aug-20
SWN14	-33.05163	116.54143	Quindanning, WA	Trillium Compact 120s	18-Sep-20
SWN15	-33.18453	117.65945	Dumbleyung, WA	Trillium Compact 120s	13-Aug-20
SWN16	-33.53399	118.51226	Pingrup, WA	Trillium Compact 120s	10-Sep-20
SWN17	-34.03496	115.60883	Darradup, WA	Trillium Compact 120s	16-Sep-20
SWN18	-30.36201	117.11603	Kalennie, WA	Trillium Compact 120s	30-Sep-20
SWN19	-34.20616	116.10282	Ringbarkers, WA	Trillium Compact 120s	16-Sep-20
SWN20	-33.84098	116.98074	Muradup, WA	Trillium Compact 120s	17-Sep-20
SWN21	-34.34672	118.52608	Gnowellen, WA	Trillium Compact 120s	11-Sep-20
SWN22	-33.08253	119.69009	Lake King, WA	Trillium Compact 120s Posthole	10-Sep-20
SWN23	-34.33802	116.64501	Lake Unicap, WA	Trillium Compact 120s	14-Aug-20
SWN24	-34.36214	117.55348	Tenterden, WA	Trillium Compact 120s	17-Sep-20
SWN25	-34.95166	116.72426	Walpole, WA	Trillium Compact 120s	17-Sep-20
SWN26	-32.4326	118.92857	Hyden, WA	Trillium Compact 120s	01-Jan-21
SWN27	-31.4539	119.43164	Marvel Loch, WA	Güralp 6TD	01-Oct-20
Additional stations added during monitoring of the Arthur River swarm					
SWNNA	-33.32605	117.40191	Puntapin Rock, WA	Smart Solo IGU-BD3C	10-Jan-22
SWNNB	-33.36294	117.19092	Warup, WA	Smart Solo IGU-BD3C	10-Jan-22
SWNNC	-33.19388	117.28902	Piesseville, WA	Smart Solo IGU-BD3C	10-Jan-22
SWNND	-33.41912	117.03954	East Arthur River, WA	Smart Solo IGU-BD3C	10-Jan-22
SWNNE	-33.28442	117.0303	Arthur River, WA	Smart Solo IGU-BD3C	10-Jan-22
SWNNF	-33.34386	116.9502	Mialling Pool, WA	Smart Solo IGU-BD3C	10-Jan-22
SWNNG	-33.41822	117.00788	Clifton Park, WA	Smart Solo IGU-BD3C	10-Jan-22
SWNNH	-33.38816	116.8996	Tuchbrook, WA	Smart Solo IGU-BD3C	10-Jan-22
SWNNI	-33.35815	116.9755	Coalfields Rd 1, WA	Smart Solo IGU-BD3C	06-May-22
SWNNJ	-33.36556	116.9908	Coalfields Rd 2, WA	Smart Solo IGU-BD3C	06-May-22

Tectonic units, tectonic setting and seismicity of southwestern Western Australia

RE Murdie, TJ Ivanic, R Quentin de Gromard, CM Thomas, K Gessner, V Markwitz and PW Haines

Scientific abstract

The geology of southwest Western Australia comprises the Archean Yilgarn Craton and its Proterozoic and Phanerozoic margins. In the area, granites and greenstone of the South West Terrane and the Youanmi Terrane are bounded by Proterozoic orogens, including the Albany–Fraser Orogen to the south, and the Pinjarra Orogen to the west. The Yilgarn Craton and the Pinjarra Orogen are overlain by the Paleozoic to Cenozoic Perth Basin. The complex crustal architecture of southwest Western Australia is the result of tectonic processes that can be traced back to Neoarchean cratonization and several episodes of amalgamation and rifting during Proterozoic and Phanerozoic supercontinent cycles. The dominant tectonic feature of southwest Western Australia is the Darling Fault, a long-lived, but currently inactive fault zone that separates key tectonic units in the State and can be mapped by geophysical data over a length of about 1500 km in north–south orientation. Southwest Western Australia produces precious metals, base metals, critical minerals, basic raw materials, and energy resources that include petroleum, natural hydrogen and reservoirs for hydrogen and carbon storage.

KEYWORDS: Albany–Fraser Orogen, Darling Fault, Perth Basin, Pinjarra Orogen, Yilgarn Craton

Lay abstract

Southwest Western Australia is made up of ancient continental fragments, some of which can be traced back billions of years. During its long geological history, this part of the Australian continent experienced episodes of crustal melting, mountain building, volcanism, erosion, and continental breakup. The oldest portion of continental crust in this area, the more than 2.6-billion-year-old Yilgarn Craton is surrounded by geological units that include sedimentary, magmatic and metamorphic rocks that formed over the last 2 billion years. The Darling Fault, a more than 1200 km long, currently inactive fault zone is the dominant tectonic feature of southwest Western Australia. Southwest Western Australia contains economical quantities of mineral and petroleum resources, and has the potential for carbon and hydrogen storage.

Present-day tectonic configuration

The geology of southwestern Western Australia is dominated by the Archean Yilgarn Craton, which is bounded by the Proterozoic Albany–Fraser Orogen to the south and the Proterozoic Pinjarra Orogen and the Paleozoic to Cenozoic Perth Basin to the west. The Pinjarra Orogen is exposed to the west of the Darling Fault the as the Leeuwin, Mullingar and Northampton Inliers and most likely constitutes basement to the Perth Basin (Fig. 2). The Pinjarra Orogen also comprises remnants of the Proterozoic Badgeradda, Moora, Cardup and Yandanooka basins, which are exposed along either side of the Darling Fault. Southwestern Western Australia has been shaped by Archean and Proterozoic crustal growth and reworking events, and by Phanerozoic continental rifting and breakup. Together with the submerged Naturaliste Plateau, the area makes up the southwestern-most continental portion of the Australian Plate, which is surrounded by passive continental margins of the Indian and Southern Oceans.

Yilgarn Craton

The Yilgarn Craton comprises granite–greenstone terrain and high-grade gneisses which formed between 3.73 and 2.60 Ga (Fig. 3). The southwest Yilgarn Craton includes the southern part of the Youanmi Terrane and the entire South West Terrane. The boundary between these two terranes has been defined by integrating interpretations of aeromagnetic and gravity data (Quentin de Gromard et al., 2021) with metamorphic history (Korhonen et al., 2021), geochronology (Lu et al., 2021), greenstone geochemistry (Ivanic et al., 2021) and granite geochemistry (Smithies et al., 2021, 2023). The terrane boundary separates granulite-facies meta-igneous rocks of the Corrigin Tectonic Zone (CTZ, Domain 3, Fig.3) in the hanging wall from the underlying South West Terrane. The CTZ is a strongly deformed, high-grade metamorphic equivalent of the northern Youanmi Terrane. The recently completed active seismic reflection survey 23GSWA-SW1 (MAGIX file 72447 [MAGIX]) has been undertaken to provide further insight into the deep structure of this part of the Yilgarn Craton, and of the Pinjarra Orogen and the Perth Basin.

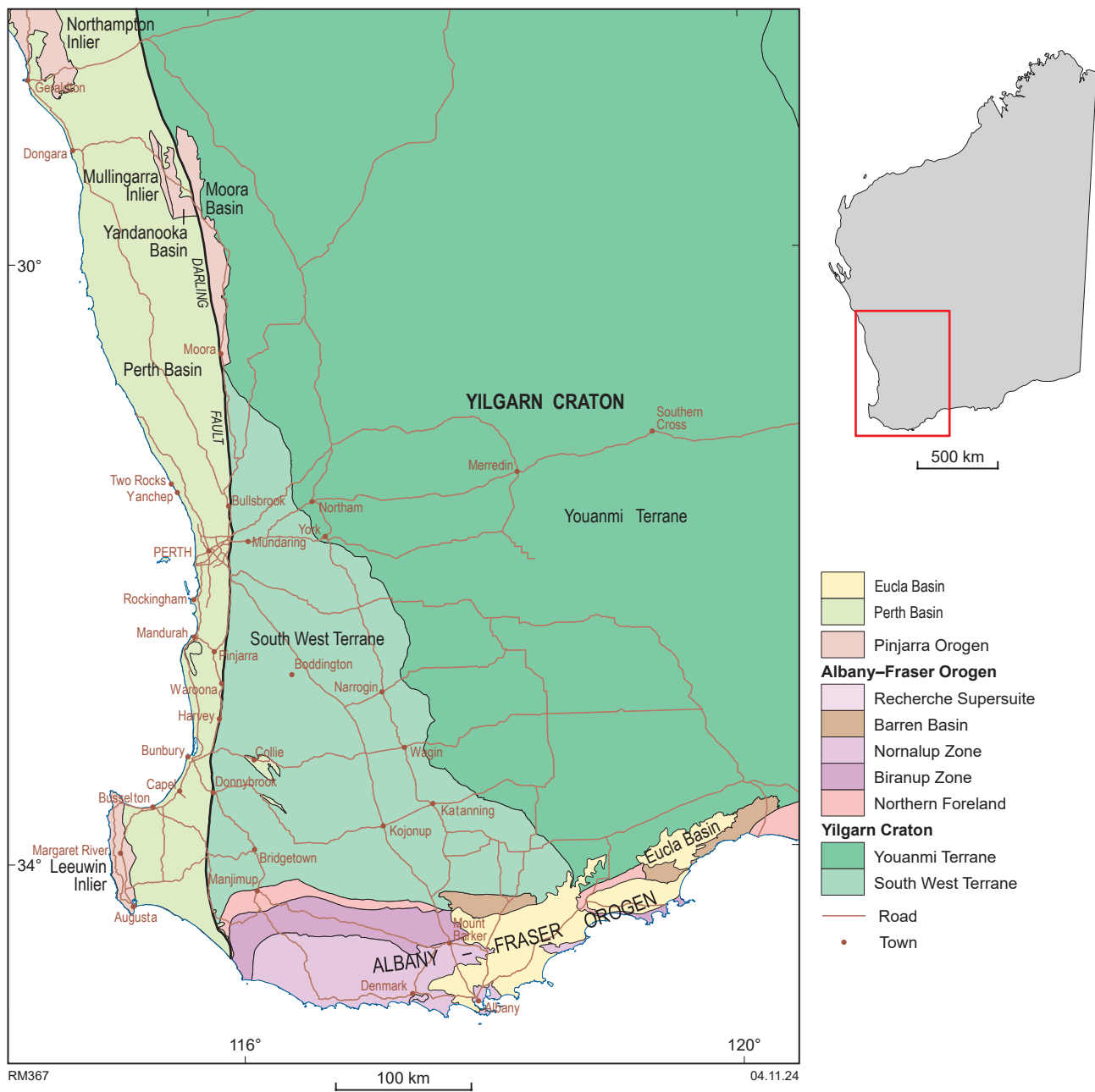


Figure 2. Tectonic units of southwest Western Australia

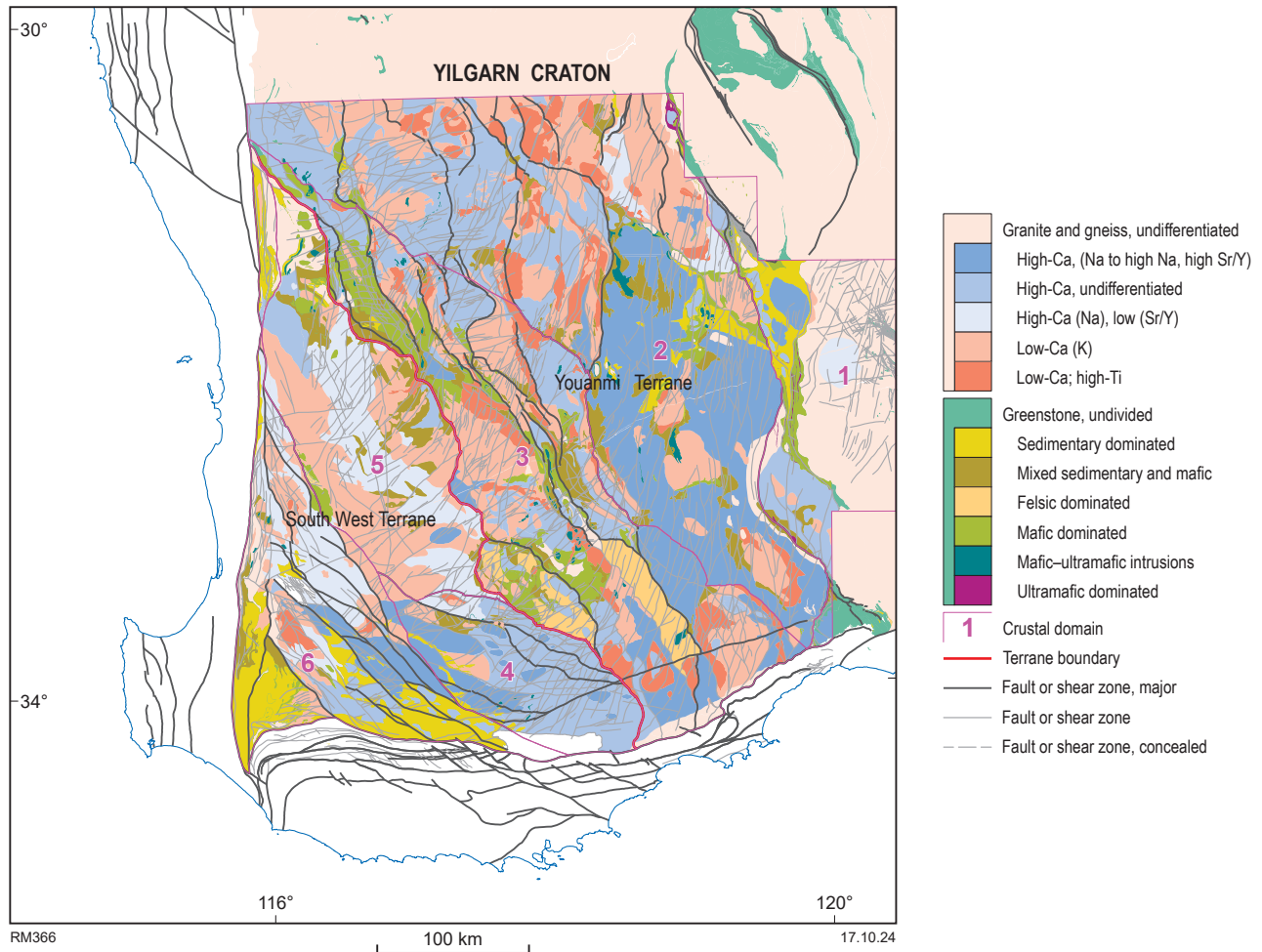


Figure 3. Simplified geology and tectonic subdivisions of the southwestern Yilgarn Craton. Granitic rocks are differentiated by geochemistry (after Smithies et al., 2023) and greenstones are characterized by their dominant lithological components (after Quentin de Gromard et al., 2024). Older interpreted tectonic units are taken from the 1:500 000 tectonic units digital layer (GSWA, 2021)

Yilgarn Craton granitic rocks have been classified by Smithies et al. (2023) on the basis of geochemical composition. This granite classification allows the mapping of crustal and lithospheric architecture based on granite melt source characteristics.

The greenstones comprise stratigraphic packages of ultramafic, mafic and felsic to intermediate volcanic rocks, siliciclastic sedimentary rocks, and chemical sedimentary rocks such as chert-rich rocks. These are typically intruded by mafic–ultramafic sills or layered intrusions at several time intervals (Smithies et al., 2017). Greenstones in the South West Terrane are currently understood to be younger than those in the Youanmi Terrane (Quentin de Gromard et al., 2021).

A prominent feature of the southwestern Yilgarn is intrusion of nine mafic dyke suites (Fig. 4a) with ages ranging from c. 2615 to 733 Ma, (Wingate, 2007, 2017; Stark et al., 2018, 2019; Austin et al., 2022; Quentin de Gromard and Ivanic, 2024). Each of these suites comprises hundreds of individual dykes, some of which are hundreds of kilometres long. Dykes are prominent in aeromagnetic imagery (Fig. 4c) with both positive and negative polarities, depending on their age.

The Yilgarn Craton is highly prospective for deposits of gold, nickel, lithium, copper, zinc, iron, tantalum, aluminium,

uranium and other metals. The demand for these minerals is driving the need for an understanding of deeper lithospheric features, which may be imaged using passive seismic techniques.

An interpretation of the deep-crustal reflection seismic line 23GSWA-SW1 is currently underway and planned to be released in 2025. However, initial observations and correlations with detailed field mapping permits an insight into the different crustal domains of the Craton (Fig. 4c, d). Description of five individual crustal domains of the South West and southern Youanmi Terranes is detailed in Quentin de Gromard and Ivanic (2024) and briefly summarized here. Domains 1 and 2 show typical Archean granite–greenstone configuration as seen elsewhere in the Youanmi Terrane (e.g. Chen et al., 2001). Domain 1 has a lower metamorphic grade (greenschist to amphibolite facies) than Domain 2 (amphibolite to granulite facies), which is thought to have been exhumed from mid-crustal levels. These domains are separated by the transcrustal Youanmi Shear Zone. Basement rocks of Domain 2, mainly tonalite–trondhjemite–granodiorite (TTG) gneisses with high Ca and high Sr/Y ratios (Smithies et al., 2023), appear as north-north-westerly trending lozenges between anastomosing shear zones. The greenstones are manifest as dismembered rafts within the granites and along shear zones (Quentin de Gromard et al., 2021).

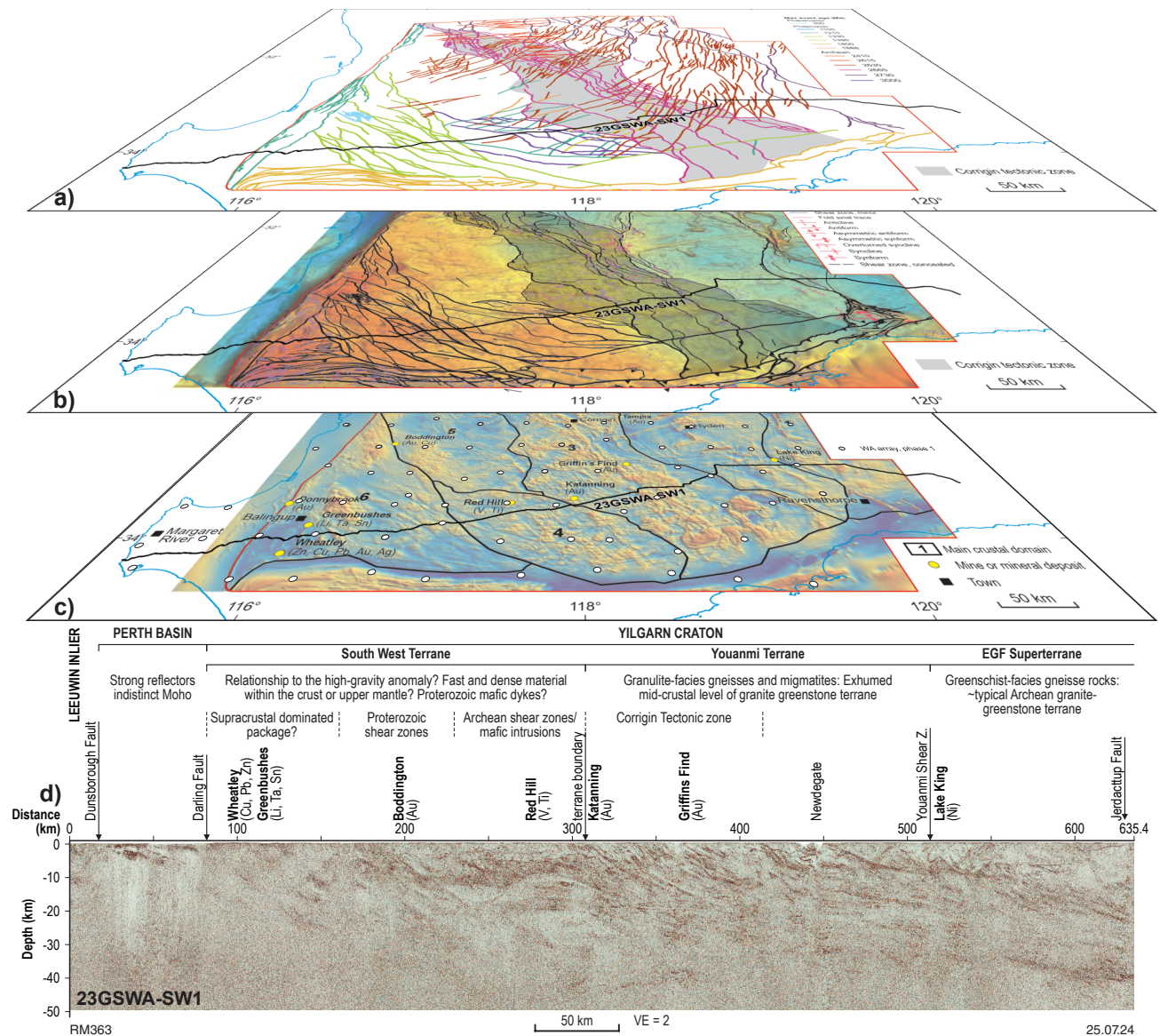


Figure 4. Geology and geophysics of southwest Western Australia as data layers: a) dykes; b) Bouguer anomaly; c) total magnetic intensity (TMI), faults and domains; d) 24GSA-SW1 active seismic section with annotation after Quentin de Gromard (2024). Location of the seismic line is shown on each image

The Corrigin Tectonic Zone (Domain 3) is a migmatitic, granulite-facies domain within the southern Youanmi Terrane. The CTZ is highly deformed by northeast-dipping thrusts and northwest-striking shear zones showing a sinistral movement. The basement rocks are mainly TTG gneisses intruded by tabular sheets of monzogranites and syenogranites emplaced along shear zones. The CTZ is interpreted as a portion of the Youanmi Terrane which has been exhumed from mid-crustal levels and thrust over the South West Terrane (Quentin de Gromard et al., 2021).

The South West Terrane (Domains 5 and 6) has an anomalously high Bouguer gravity signal (Fig. 4b) that has been attributed to any of a denser basement into which the plutons were intruded (Quentin de Gromard et al., 2021), an underplate, or a higher density of mafic dykes (Dentith et al., 2000). Further work is required to model solutions to this pattern of gravity responses.

Domain 5 of the South West Terrane is interpreted as an upper-crustal domain based on its lower metamorphic grade (greenschist facies). The southwestern part of the South West Terrane (Domain 6) has a significant Proterozoic overprint with shear zones parallel to the Darling Fault, or parallel to the Albany–Fraser Orogen, or closely spaced and northwest striking (Fig. 3).

Albany–Fraser Orogen

The Paleo- to Mesoproterozoic Albany–Fraser Orogen (AFO) is an arcuate orogenic belt that borders the southern and southeastern margin of the Archean Yilgarn Craton (Fig. 5). Most work on the AFO has been done in its eastern portion, partly due to the high-prospectivity potential of the mafic rocks of the Fraser Zone (Spaggiari et al., 2009, 2014a, 2015). The western AFO is an east-striking belt dominated by Mesoproterozoic granitic rocks and gneisses dissected by major east-striking shear zones bounding the various tectonic units described below. The east-striking fabric of the western AFO is displaced along northwest-striking faults with an apparent dextral sense of movement based on interpretation of the aeromagnetic data. The faults are possibly linked to the northwest-striking shear zones of Domain 6 of the southwestern South West Terrane (Standen et al., 2020; Quentin de Gromard et al., 2021).

Barren Basin

Sedimentary rocks of the Barren Basin (1815–1600 Ma) were laid down in an extensive extensional basin on the edge of the Yilgarn Craton (Spaggiari et al., 2015) and were largely derived from the Yilgarn Craton and its Proterozoic covering. They are now preserved in thrust sheets emplaced during the Albany–Fraser Orogeny (Myers, 1995a; Nelson et al., 1995; Spaggiari et al., 2015) and sit as present-day topographic highs; for example, the Stirling Ranges and peaks of Fitzgerald River National Park.

Northern Foreland

The Northern Foreland comprises greenschist-facies rocks reworked from the Yilgarn Craton, which have been later intruded by Paleoproterozoic and Mesoproterozoic magmatic rocks and subsequently deformed and metamorphosed during the Albany–Fraser Orogeny (Myers, 1990, 1995a; Nelson et al., 1995; Spaggiari et al., 2009, 2011, 2014b; Kirkland et al., 2011). These rocks are still clearly identifiable as products derived from the Yilgarn Craton. The Munglinup Gneiss is a higher-metamorphic grade component of the Northern Foreland, which has been

exhumed from a deeper crustal level (Beeson et al., 1988; Spaggiari et al., 2009, 2011, 2014a). The Northern Foreland is bounded to the north by the Manjimup Fault (Wilde and Low, 1978; Wilde and Walker, 1981)

Kepa Kurl Booya Province

The Kepa Kurl Booya Province comprises the Biranup Zone and Nornalup Zone. The Biranup Zone consists of strongly deformed orthogneiss derived from late Archean and Paleo- and Mesoproterozoic granitic rocks that were metamorphosed during the Mesoproterozoic Albany–Fraser Orogeny (Nelson et al., 1995; Spaggiari et al., 2009; Kirkland et al., 2011). It is separated from the Nornalup Zone by the Northcliffe Fault.

The Nornalup Zone is the southern and eastern most unit of the Albany–Fraser Orogen (Clark et al., 2014). It consists of a Paleoproterozoic basement of ortho- and paragneiss which are heavily intruded by granitic intrusions of the 1330–1280 Ma Recherche Supersuite and the 1200–1140 Ma Esperance Supersuite, two major magmatic events that coincided with Stages I and II of the Albany–Fraser Orogeny, respectively (Nelson et al., 1995; Clark et al., 2000; Spaggiari et al., 2011; Smithies et al., 2014). The peaks of the Porongurup Ranges are examples of the Esperance Supersuite.

Tectonic history of the Albany–Fraser Orogen

Paleoproterozoic tectonic events include dominantly felsic magmatism during the Salmon Gums Event (1815–1800 Ma), the Ngadju Event (1780–1760 Ma), and the Biranup Orogeny (1710–1650 Ma) (Kirkland et al., 2011; Spaggiari et al., 2011, 2014b).

Mesoproterozoic tectonism is defined as the Albany–Fraser Orogeny, which is separated into two stages: Stage I (1330–1260 Ma) and Stage II (1225–1140 Ma) (Clark et al., 2000; Bodorkos and Clark, 2004; Spaggiari et al., 2014b). Stage I was a widespread coeval felsic and mafic magmatic event

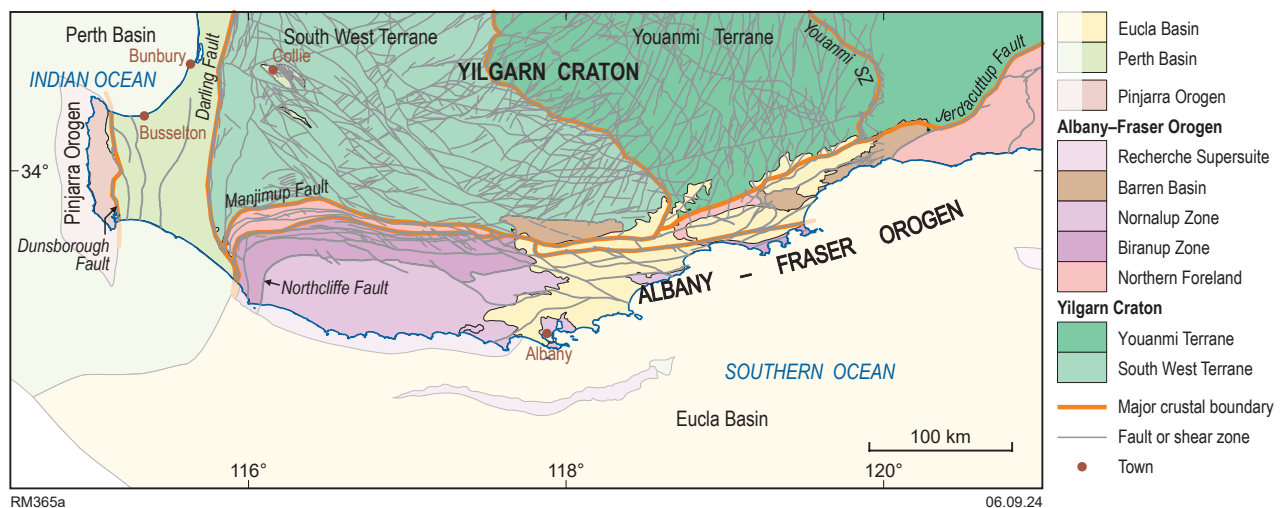


Figure 5. Generalized tectonic subdivisions and associated major crustal boundaries of the southwest of Western Australia

attributed to the collision between West Australian and Mawson Cratons (Nelson et al., 1995; Clark, 1999; Bodorkos and Clark, 2004; Spaggiari et al., 2014b). Geochemical, isotopic, and geophysical data indicate that the orogen developed on hyperextended Yilgarn Craton crust (Smithies et al., 2014, 2015); hence, the Albany–Fraser Orogen was always part of the West Australian Craton. Stage II is interpreted as an intracratonic orogenesis with craton-verging thrusting, high temperatures, moderate pressure and felsic magmatism (Myers, 1995b; Clark et al., 2000; Dawson et al., 2003; Spaggiari et al., 2009, 2011, 2014a).

Pinjarra Orogen

The north–south oriented Pinjarra Orogen extends for more than 1000 km along the western margin of the West Australian Craton. It forms the basement to the Perth Basin and is thought to comprise discrete terranes assembled during multiple orogenic events associated with the Proterozoic assembly of Gondwana, now collectively known as the Pinjarra Orogeny (Janssen et al., 2003). Drilling has only reached basement in the interbasin highs; hence, few details are known. However, it is thought to consist of several terranes of different ages accreted by strike-slip movement (Fletcher and Libby, 1993). Fault-bounded outcrops of basement can be seen in three main inliers, of which the Leeuwin Inlier is the only one covered by the SWAN project area. The Pinjarra Orogen also includes remnants of four Proterozoic sedimentary basin exposed along either side of the Darling Fault. Only the Cardup and Moora Basins are exposed within the study area.

Leeuwin Inlier

The Leeuwin Inlier is a block of granitic orthogneiss bounded by the Dunsborough Fault (Fig. 5) on its eastern margin, and extending offshore. Crystalline rocks of the Pinjarra Orogen underwent a prolonged and complex tectonic history, including metamorphic events such as high-grade amphibolite- to granulite-facies deformation in gneisses and migmatites.

U–Pb SHRIMP zircon data show that three magmatic episodes form the protoliths of the inlier, the oldest dating to 1100–1000 Ma (Nelson, 1996, 1999, 2002; Collins, 2003; Ksienzyk et al., 2012). Magmatism at 800–650 Ma corresponds to the time of the breakup of Rodinia, the late Mesozoic to early Neoproterozoic supercontinent (Powell et al., 1994; Pisarevsky et al., 2003). The youngest magmatism in the Leeuwin Complex at 550–500 Ma is associated with oblique collision of India with Australia along the Pinjarra Orogen (Collins, 2003; Janssen et al., 2003; Boger, 2011).

Based on the MINDEX database, the Leeuwin Inlier metagranitic unit contains historic gold mine shafts, heavy mineral sands deposits, PGE and gold targets, and basic raw material resources.

Cardup Basin

Rocks of the Cardup Basin (Cardup Group) are exposed as narrow slivers east of the Darling Fault in the vicinity

of Perth. The preserved succession, about 500 m thick, is predominantly shale and slate with minor sandstone, conglomerate and silicified carbonate (Playford et al., 1976). The age is not well constrained. A detrital zircon sample provides a conservative maximum deposition age of c. 1450 Ma (Wingate et al., 2018), while intruding dolerite dykes are undated but may belong to the 1218–1202 Ma Boyagin Dolerite. If the latter is correct, a mid-Mesoproterozoic depositional age can be inferred.

Moora Basin

Rocks of the Moora Basin (Moora Group) are intermittently exposed in a narrow belt just east of the Darling Fault in the northern part of the study area. The succession is up to 3500 m thick and comprises siliciclastic and carbonate rocks (commonly silicified), mostly of shallow marine origin (Playford et al., 1976). Local basaltic volcanic rocks (Morawa Lavas) are present near the base of the sequence north of the study area. The group is mildly deformed and most units are intruded by mafic dykes of multiple generations. The age of the Moora Group is only loosely constrained. The Morawa Lavas in the north have yielded an imprecise Rb–Sr isochron of 1390 ± 140 Ma (Compston and Arriens, 1968; Giddings, 1976). Given the methods, uncertainties and vintage of the data, this result needs confirmation by modern techniques. A detrital zircon sample from the middle of the group yielded mostly Archean zircons, with only one younger zircon dated at c. 1800 Ma (Wingate et al., 2022). Some of the intruding dykes are assigned to the 1218–1202 Ma Boyagin Dolerite. If correct, this provides a minimum age for most of the group, although the youngest unit may post-date the dolerite intrusions.

Perth Basin

The western continental margin of Western Australia is the result of a long history of amalgamation and rifting of continental fragments that eventually led up to the separation of Greater India from Australia and the breakup of Gondwana in the Early Cretaceous (Gibbons et al., 2012), with the closing of the Neotethys ocean and formation of the Indian Ocean. It forms part of the present-day passive margin. The geology of the southern end of the western margin of Western Australia today comprises the Perth Basin with several inliers of older Proterozoic basement (Pinjarra Orogen; Fig. 2). The broad architecture of the Perth Basin comprises northerly trending, westwards shallowing depocenters bounded by a series of en echelon normal faults later linked by relay ramp breaching (Thomas, 2018).

The Perth Basin is filled with up to 15 km of mid-Carboniferous to Lower Cretaceous sedimentary rocks, which record a long-lived, mainly non-marine depositional environment in the southern part of the basin, with occasional marine incursions (Fig. 6). Extensional events are interpreted in the pre-Permian to earliest Permian, Late Triassic to Early Jurassic, and Late Jurassic to Early Cretaceous, as evidenced by thickened sedimentary sequences which accumulated against the major faults (Iasky, 1993; Harris, 1994; Song and Cawood, 2000; Goleby et al., 2003; Nicholson et al., 2008; Thomas, 2018).

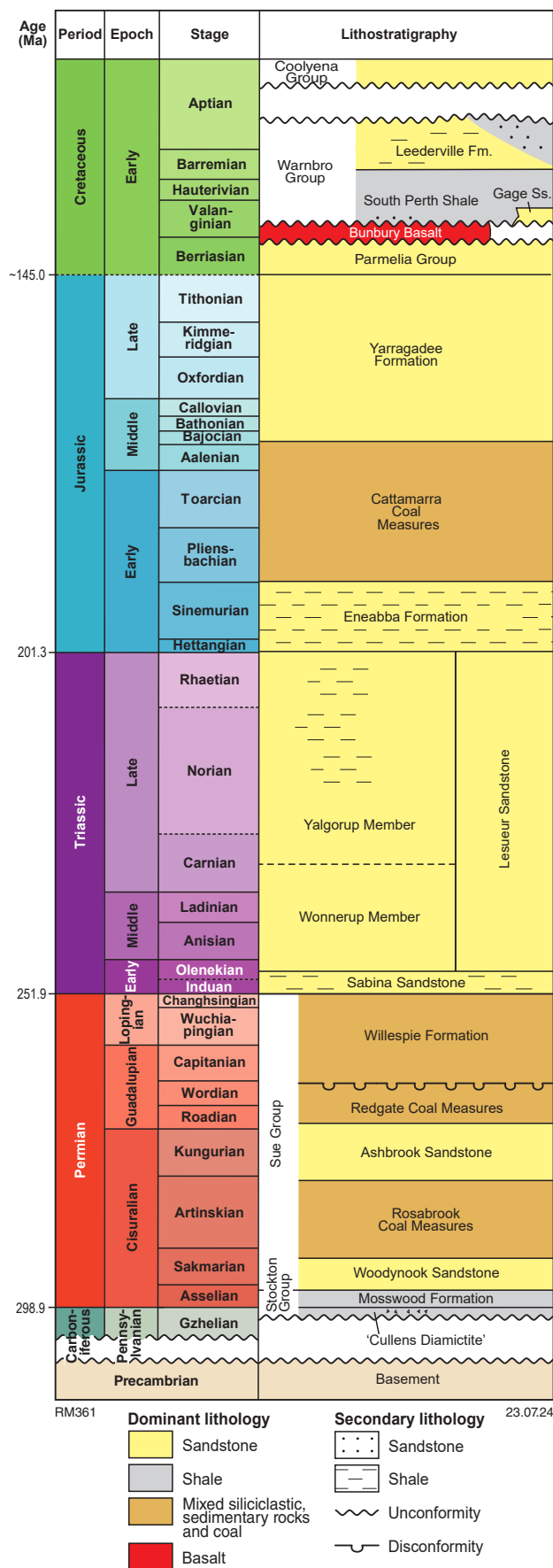


Figure 6. Perth Basin stratigraphy after Thomas (2018)

Extension in the early Permian was likely oriented east–west and later Mesozoic rifting that led to breakup is interpreted to have been oriented northwest–southeast with a dextral shear-sense component on major northerly striking faults such as the Darling Fault (Harris, 1994; Thomas, 2014). This was influenced by the earlier east–west fabric. The final stages of rifting in the Middle Jurassic to earliest Cretaceous resulted in the breakup of Gondwana and took part in two-phases (Jones et al., 2011): an initial phase of slow rifting, followed by high-velocity rifting. This is common for rifts that lead to continental breakup (Brune et al., 2016). The final superstructure is a series of sub-basins seen in the gravity signal (Brett, 2020).

The Greater India – Australia breakup was accompanied by extrusion of the Bunbury Basalt dated from c. 137 to 130 Ma (Olierook et al., 2015). These basalts filled paleovalleys and are prominent in the magnetic intensity maps. Marine sedimentary rocks are recorded post-rifting. Since the Cretaceous, there is a record of thermal subsidence and minor tectonism, but no major upheavals affecting the Perth Basin (Thomas, 2018).

Lower to mid-Permian rocks preserved in <20 km-long outliers of the Collie, Wilga and Boyup Sub-basins are all that remain of an up to 2 km-thick sediment package that extended from the Perth Basin across the western Yilgarn Craton (Norvick and Smith, 2001).

Rifting of Australia's southern margin with Antarctica began at 165–160 Ma (Williams et al., 2011), with sea-floor spreading established by c. 84 Ma (White et al., 2013) and complete separation by 40 Ma (Mory, 2023). It is unclear how this event affected the structure and stratigraphy of the southern Perth Basin.

The rocks of the Perth Basin are today mainly exploited for natural gas, coal (in the Collie Sub-basin only) and heavy mineral sands. It is also being investigated for carbon dioxide storage potential. Limestone is quarried for the construction industry. Aquifers in the sandstone formations are a source of fresh water for communities and agriculture.

Exploration onshore for petroleum began in the mid-1960s; this saw the drilling of exploration wells and acquisition of seismic reflection lines. The basin has a relatively dense coverage of industry seismic reflection lines, but in the southern part of the basin the quality of the majority of lines is poor to moderate due to their vintage. These lines do not image the Moho as they record generally only up to 5 seconds of data; however, a deep-crustal seismic reflection survey was acquired in late 2023 and this recorded 20 seconds of data. Interpretation of this dataset is ongoing. A passive seismic imaging campaign (Murdie et al., 2020) had limited success in imaging the Moho.

Darling Fault

The Darling Fault (Wilde and Low, 1975, 1978) separates the Yilgarn Craton from most parts of the Pinjarra Orogen and the Perth Basin. It forms a c. 1500 km-long topographic feature which corresponds to the boundary between a Bouguer low over the Perth Basin and a gravity high over the Yilgarn Craton (Brett, 2020). The Darling Fault has been imaged in a deep seismic reflection survey NN92-01 (Middleton et al., 1993) and passive seismic studies (Murdie

et al., 2020) as a steeply west-dipping planar fault extending to the mantle. Archean fabrics show that deformation along the Darling Fault has a long history (Zibra and Peterzell, 2024). It was active episodically in the Proterozoic to Cambrian, during the assembly of Gondwana, and as a sinistral strike-slip zone during the oblique suturing of India to Australia (Janssen et al., 2003). Subsequent tectonic events during the Phanerozoic reactivated the original fabric (Dentith et al., 1993; Fitzsimons, 2003; Janssen et al., 2003; Pisarevsky et al., 2003). During the various Permo–Cretaceous rifting phases of eastern Gondwana, the Darling Fault was the eastern edge of an intracontinental rift which later evolved into a passive margin (Song and Cawood, 2000). Despite topographic relief that can amount to several hundred metres, the Darling Fault is currently seismically inactive.

References

- Austin, JM, Hayman, PC, Murphy, DT, Wingate, MTD, Lu, Y, Lowrey, J and Rose, K 2022, The voluminous 2.81–2.71 Ga goldfields Tholeiitic super event: implications for basin architecture in the Yilgarn Craton and global correlations: *Precambrian Research*, v. 369, article no. 106528, published online 30 December 2021, doi:10.1016/j.precamres.2021.106528.
- Beeson, J, Delour, CP and Harris, LB 1988, A structural and metamorphic traverse across the Albany Mobile Belt, Western Australia: *Precambrian Research*, 40–41, p. 117–136, doi:10.1016/0301-9268(88)90064-2.
- Beslier, MO, Whitmarsh, RB, Wallace, PJ and Girardeau, J (editors) 2001, *Proceedings of the Ocean Drilling Program, Scientific Results*, v. 173.
- Bodorkos, S and Clark, DJ 2004, Evolution of a crustal-scale transpressive shear zone in the Albany–Fraser Orogen, SW Australia: 1. P–T conditions of Mesoproterozoic metamorphism in the Coramup Gneiss: *Journal of Metamorphic Geology*, v. 22, no. 8, p. 691–711, doi:10.1111/j.1525-1314.2004.00543.x.
- Borissova, I 2002, Geological framework of the Naturaliste Plateau: Geoscience Australia, Canberra, ACT, Record 2002/20, 44p.
- Brett, JW 2020, 400 m Bouguer gravity merged grid of Western Australia 2020 version 1: Geological Survey of Western Australia; data layer, <www.dmp.wa.gov.au/geophysics>.
- Brune, S, Williams, SE, Butterworth, NP and Muller, RD 2016, Abrupt plate accelerations shape rifted continental margins: *Nature*, v. 536, no. 7615, p. 201–204, doi:10.1038/nature18319.
- Chen, SF, Witt, WK and Liu, S 2001, Transpression and restraining jogs in the northeastern Yilgarn Craton, Western Australia: *Precambrian Research*, v. 106, p. 309–328.
- Clark, C, Kirkland, CL, Spaggiari, CV, Oorschot, C, Wingate, MTD and Taylor, RJ 2014, Proterozoic granulite formation driven by mafic magmatism: An example from the Fraser Range Metamorphics, Western Australia: *Precambrian Research*, v. 240, p. 1–21, doi:10.1016/j.precamres.2013.07.024.
- Clark, DJ 1999, Thermo-tectonic evolution of the Albany–Fraser Orogen, Western Australia: University of New South Wales, Sydney, New South Wales, PhD thesis (unpublished).
- Clark, DJ, Hensen, BJ and Kinny, PD 2000, Geochronological constraints for a two-stage history of the Albany–Fraser Orogen, Western Australia: *Precambrian Research*, v. 102, no. 3, p. 155–183, doi:10.1016/S0301-9268(00)00063-2.
- Collins, AS 2003, Structure and age of the northern Leeuwin Complex, Western Australia: constraints from field mapping and U–Pb isotopic analysis: *Australian Journal of Earth Sciences*, v. 50, p. 585–599.
- Compston, W and Arriens, PA 1968, The Precambrian geochronology of Australia: *Canadian Journal of Earth Sciences*, v. 5, p. 561–583, doi:10.1139/e68-052.
- Dawson, GC, Krapež, B, Fletcher, IR, McNaughton, N and Rasmussen, B 2003, 1.2 Ga thermal metamorphism in the Albany–Fraser Orogen of Western Australia: Consequence of collision or regional heating by dyke swarms? *Journal of the Geological Society, London*, v. 160, p. 29–37.
- Dentith, MC, Bruner, I, Long, A, Middleton, MF and Scott, J 1993, Structure of the Eastern Margin of the Perth Basin, Western Australia: *Exploration Geophysics*, v. 24, no. 3–4, p. 455–461, doi:10.1071/EG993455.
- Dentith, MC, Dent, VF and Drummond, BJ 2000, Deep crustal structure in the southwestern Yilgarn Craton, Western Australia: *Tectonophysics*, v. 325, p. 227–255.
- Fitzsimons, ICW 2003, Proterozoic basement provinces of southern and southwestern Australia, and their correlation with Antarctica: Geological Society, London, Special Publications, v. 206, p. 93–130.
- Fletcher, IR and Libby, WG 1993, Further isotopic evidence for the existence of two distinct terranes in the southern Pinjarra Orogen, Western Australia, in *Professional papers: Geological Survey of Western Australia*, Report 34, p. 81–84.
- Geological Survey of Western Australia 2021, 1:10 000 000 tectonic units of Western Australia: Geological Survey of Western Australia; digital data layer, <www.dmirs.wa.gov.au/geoview>.
- Giddings, JW 1976, Precambrian palaeomagnetism in Australia I: Basic dykes and volcanics from the Yilgarn Block: *Tectonophysics*, v. 30, p. 91–108, doi:10.1016/0040-1951(76)90138-4.
- Gibbons, AD, Barckhausen, U, den Bogaard, P, Hoernle, K, Werner, R, Whittaker, JM and Muller, RD 2012, Constraining the Jurassic extent of Greater India: Tectonic evolution of the West Australian margin: *Geochemistry Geophysics Geosystems* G3, v. 13, no. 5, p. 1–25.
- Harris, LB 1994, Structural and tectonic synthesis of the Perth Basin, Western Australia: *Journal of Petroleum Geology*, v. 17, p. 129–156.
- Iasky, RP 1993, A structural study of the southern Perth Basin, Western Australia: Geological Survey of Western Australia, Report 31, 56p.
- Ivanic, TJ, Lowrey, JR and Smithies, RH 2021, New geochemical constraints on the mafic and ultramafic rocks of the southwest Yilgarn: Geological Survey of Western Australia, digital data layer, in *Accelerated Geoscience Program extended abstracts compiled by Geological Survey of Western Australia: Geological Survey of Western Australia*, Record 2021/4, p. 104–107.
- Janssen, DP, Collins, AS and Fitzsimons, ICW 2003, Structure and tectonics of the Leeuwin Complex and Darling Fault Zone, southern Pinjarra Orogen, Western Australia – a field guide: Geological Survey of Western Australia, Record 2003/15, 33p.
- Jones, AT, Kennard, JM, Nicholson, CJ, Bernardel, G, Mantle, D, Grosjean, E, Boreham, CJ, Jorgensen, DC and Robertson, D 2011, New exploration opportunities in the offshore northern Perth Basin: *The APPEA Journal*, p. 45–78.
- Kirkland, CL, Spaggiari, CV, Pawley, MJ, Wingate, MTD, Smithies, RH, Howard, HM, Tyler, IM, Belousova, EA and Poujol, M 2011, On the edge: U–Pb, Lu–Hf, and Sm–Nd data suggests reworking of the Yilgarn Craton margin during formation of the Albany–Fraser Orogen: *Precambrian Research*, v. 187, no. 3–4, p. 223–247, doi:10.1016/j.precamres.2011.03.002.
- Korhonen, FJ, Blereau, ER, Kelsey, DE, Fielding, IOH and Romano, SS 2021, Metamorphic evolution of the southwest Yilgarn, in *Accelerated Geoscience Program extended abstracts compiled by Geological Survey of Western Australia: Geological Survey of Western Australia*, Record 2021/4, p. 108–115.
- Leonard, M 2002, The Burakin WA earthquake sequence Sept 2000 – June 2002, in *Australian Earthquake Engineering Society Conference 2002: Australian Earthquake Engineering Society Conference 2002*, Adelaide, South Australia.
- Leonard, M, Ripper, ID and Yue, L 2002, Australian earthquake fault plane solutions: Geoscience Australia, Record 2002/19.

- Lu, Y, Wingate, MTD, Champion, DC, Smithies, RH, Johnson, SP, Mole, DR, Poujol, M, Zhao, J, Maas, R and Creaser, RA 2021, Samarium–neodymium isotope map of Western Australia, *in* Accelerated Geoscience Program extended abstracts *compiled by* Geological Survey of Western Australia: Geological Survey of Western Australia, Record 2021/4, p. 10–12.
- Middleton, MF, Long, A, Wilde, SA, Dentith, M and Evans, BA 1993, A preliminary interpretation of deep seismic reflection and other geophysical data from the Darling Fault Zone, Western Australia: *Exploration Geophysics*, v. 24, no. 3–4, p. 711–717, doi:10.1071/EG993711.
- Mory, AJ 2023, Mesozoic transformation of Western Australia: rifting and breakup of Gondwana: Geological Survey of Western Australia, Perth, Western Australia, 73p.
- Murdie, RE, Yuan, H and Lin, X 2020, A passive seismic experiment in the Perth Basin, Western Australia: Geological Survey of Western Australia, Report 208, 19p.
- Myers, JS 1990, Albany–Fraser Orogen, *in* Geology and mineral resources of Western Australia *edited by* Geological Survey of Western Australia: Geological Survey of Western Australia, Memoir 3, p. 255–263.
- Myers, JS 1995a, Geology of the Esperance 1:1 000 000 sheet: Geological Survey of Western Australia, 1:1 000 000 Geological Series Explanatory Notes, 10p.
- Myers, JS 1995b, The generation and assembly of an Archaean supercontinent: Evidence from the Yilgarn Craton, Western Australia, *in* Early Precambrian processes *edited by* MP Coward and AC Reis: The Geological Society of London, Special Publication 95, p. 143–154, doi:10.1144/GSL.SP.1995.095.01.09.
- Nelson, DR 1996, Compilation of SHRIMP U–Pb zircon geochronology data, 1995: Geological Survey of Western Australia, Record 1996/5, 168p.
- Nelson, DR 1999, Compilation of geochronology data, 1998: Geological Survey of Western Australia, Record 1999/2, 222p.
- Nelson, DR 2002, Compilation of geochronology data, 2001: Geological Survey of Western Australia, Record 2002/2, 282p.
- Nelson, DR, Myers, JS and Nutman, AP 1995, Chronology and evolution of the Middle Proterozoic Albany–Fraser Orogen, Western Australia: *Australian Journal of Earth Sciences*, v. 42, p. 481–495, doi:10.1080/08120099508728218.
- Nicholson, CJ, Borissova, I, Krassay, AA, Boreham, CJ, Monteil, E, Neumann, V, Di Primio, R and Bradshaw, BE 2008, New exploration opportunities in the southern Vlaming Sub-basin: The APPEA Journal, v. 2008, p. 371–380.
- Norvick, MS and Smith, MA 2001, Mapping the plate tectonic reconstruction of southern and southeastern Australia and implications for petroleum systems: The APPEA Journal, v. 41, no. 1, p. 15–35.
- Olierook, HKH, Timms, NE, Merle, RE, Jourdan, F and Wilkes, PG 2015, Paleodrainage and fault development in the southern Perth Basin, Western Australia during and after the breakup of Gondwana from 3D modelling of the Bunbury Basalt: *Australian Journal of Earth Sciences*, p. 289–305, doi:10.1080/08120099.2015.1030774.
- Pisarevsky, SA, Wingate, MTD, Powell, CMcA, Johnson, SP and Evans, DAD 2003, Models of Rodinia assembly and fragmentation: Geological Society, London, Special Publications, v. 206, no. 1, p. 35–55, doi:10.1144/GSL.SP.2003.206.01.04.
- Playford, PE, Cockbain, AE and Low, GH 1976, Geology of the Perth Basin, Western Australia: Geological Survey of Western Australia, Bulletin 124, 311p.
- Powell, CMcA, Preiss, WV, Gatehouse, CG, Krapež, B and Li, ZX 1994, South Australian record of a Rodinian epicontinental basin and its mid-Neoproterozoic breakup (~700 Ma) to form the Palaeo-Pacific Ocean: *Tectonophysics*, v. 237, p. 113–140.
- Quentin de Gromard, R, Ivanic, TJ and Zibra, I 2021, Pre-Mesozoic interpreted bedrock geology of the southwest Yilgarn, 2021, *in* Accelerated Geoscience Program extended abstracts *compiled by* Geological Survey of Western Australia: Geological Survey of Western Australia, Record 2021/4, p. 122–144.
- Quentin de Gromard, R and Ivanic, TJ (compilers) 2024, 6IAS: Redefining Archean terrane boundaries, a radical update within the Yilgarn Craton – a field guide: Geological Survey of Western Australia, Record 2023/9, 41p.
- Smithies, RH, Lowrey, JR, Champion, DC, Lu, Y and Gessner, K 2023, Spatial trends and relationships emerging from the systematic classification of granitic rocks of the Yilgarn Craton: Geological Survey of Western Australia; Record 2023/5, 33p.
- Smithies, RH, Lu, Y, Lowrey, JR, Ivanic, TJ, Champion, DC and Wilde, SA 2021, Variations in granite geochemistry in the southwest Yilgarn, *in* Accelerated Geoscience Program extended abstracts *compiled by* Geological Survey of Western Australia: Geological Survey of Western Australia, Record 2021/4, p. 149–153.
- Smithies, RH, Morris, PA, Wyche, S, De Paoli, MC and Sapkota, J 2017, Towards a geochemical barcode for Eastern Goldfields Superterrane greenstone stratigraphy – preliminary data from the Kambalda–Kalgoorlie area: Geological Survey of Western Australia, Record 2017/7, 26p.
- Smithies, RH, Spaggiari, CV and Kirkland, CL 2015, Building the crust of the Albany–Fraser Orogen; constraints from granite geochemistry: Geological Survey of Western Australia, Report 150, 49p.
- Smithies, RH, Spaggiari, CV, Kirkland, CL and Maier, WD 2014, Geochemistry and petrogenesis of igneous rocks in the Albany–Fraser Orogen, *in* Albany–Fraser Orogen seismic and magnetotelluric (MT) workshop 2014: extended abstracts *compiled by* CV Spaggiari and IM Tyler: Geological Survey of Western Australia, Record 2014/6, p. 77–88.
- Song, T and Cawood, PA 2000, Structural styles in the Perth Basin associated with the Mesozoic break-up of Greater India and Australia: *Tectonophysics*, v. 317, no. 1–2, p. 55–72, doi:10.1016/S0040-1951(99)00273-5.
- Spaggiari, CV, Bodorkos, S, Barquero-Molina, M, Tyler, IM and Wingate, MTD 2009, Interpreted bedrock geology of the south Yilgarn and central Albany–Fraser Orogen, Western Australia: Geological Survey of Western Australia, Record 2009/10, 84p.
- Spaggiari, CV, Kirkland, CL, Pawley, MJ, Smithies, RH, Wingate, MTD, Doyle, MG, Blenkinsop, TG, Clark, C, Oorschot, CW, Fox, LJ and Savage, J 2011, The geology of the east Albany–Fraser Orogen – a field guide: Geological Survey of Western Australia, Record 2011/23, 97p.
- Spaggiari, CV, Kirkland, CL, Smithies, RH, Occhipinti, SA and Wingate, MTD 2014a, Geological framework of the Albany–Fraser Orogen, *in* Albany–Fraser Orogen seismic and magnetotelluric (MT) workshop 2014: extended abstracts *compiled by* CV Spaggiari and IM Tyler: Geological Survey of Western Australia, Record 2014/6, p. 12–27.
- Spaggiari, CV, Kirkland, CL, Smithies, RH and Wingate, MTD 2014b, Tectonic links between Proterozoic sedimentary cycles, basin formation and magmatism in the Albany–Fraser Orogen, Western Australia: Geological Survey of Western Australia, Report 133, 63p.
- Spaggiari, CV, Kirkland, CL, Smithies, RH, Wingate, MTD and Belousova, EA 2015, Transformation of an Archean craton margin during Proterozoic basin formation and magmatism: the Albany–Fraser Orogen, Western Australia: *Precambrian Research*, v. 266, p. 440–466, doi:10.1016/j.precamres.2015.05.036.
- Stark, JC, Wang, X-C, Denyszyn, SW, Li, Z-X, Rasmussen, B, Zi, J-W, Sheppard, S and Liu, Y 2019, Newly identified 1.89 Ga mafic dyke swarm in the Archean Yilgarn Craton, Western Australia suggests a connection with India: *Precambrian Research*, v. 329, p. 156–169, doi:10.1016/j.precamres.2017.12.036.
- Stark, JC, Wilde, SA, Söderlund, U, Li, Z-X, Rasmussen, B and Zi, J-W 2018, First evidence of Archean mafic dykes at 2.62 Ga in the Yilgarn Craton, Western Australia: links to cratonisation and the Zimbabwe Craton: *Precambrian Research*, v. 317, p. 1–13, doi:10.1016/j.precamres.2018.08.004.
- Thomas, CM 2018, Regional seismic interpretation and structure of the southern Perth Basin: Geological Survey of Western Australia,

Report 184, 52p.

- White, LT, Gibson, GM and Lister, GS 2013, A reassessment of paleogeographic reconstructions of eastern Gondwana: Bringing geology back into the equation: *Gondwana Research*, v. 24, p. 984–998.
- Wilde, SA and Low, GH 1975, Explanatory notes on the Perth 1:250 000 geological sheet, Western Australia: Geological Survey of Western Australia, Record 1975/6, 67p.
- Wilde, SA and Low, GH 1978, Explanatory notes on the Pinjarra 1:250 000 geological sheet, Western Australia: Geological Survey of Western Australia, Record 1978/5, 63p.
- Wilde, SA and Walker, IW 1981, Explanatory notes on the Pemberton – Irwin Inlet 1:250 000 geological sheet, Western Australia: Geological Survey of Western Australia, Record 1981/10, 75p.
- Williams, SE, Whittaker, JM and Muller, RD 2011, Full-fit, palinspastic reconstruction of the conjugate Australian-Antarctic margins: *Tectonics*, v. 30, TC6012, doi:10.1029/2011TC002912.
- Wingate, MTD 2007, Proterozoic mafic dykes in the Yilgarn Craton, *in* Proceedings of Geoconferences (WA) Inc. Kalgoorlie '07 Conference, 26–27 September, Kalgoorlie, Western Australia *edited by* FP Bierlein and CM Knox-Robinson: Geoscience Australia, Record 2007/14, p. 80–84.
- Wingate, MTD 2017, Mafic dyke swarms and large igneous provinces in Western Australia get a digital makeover, *in* GSWA 2017 extended abstracts: promoting the prospectivity of Western Australia: Geological Survey of Western Australia, Record 2017/2, p. 4–8.
- Wingate, MTD, Lu, Y and Haines, PW 2018, 199482: quartzite, Austral Bricks quarry; Geochronology Record 1535: Geological Survey of Western Australia, 6p.
- Wingate, MTD, Lu, Y, Fielding, IOH, Haines, PW and Allen, HJ 2022, 215316: metasandstone, Midlands Road; Geochronology Record 1850: Geological Survey of Western Australia, 8p.
- Zibra, I and Petermann, M 2024, The Chattering Metamorphic Belt, Yilgarn Craton: structural setting, microstructures and quartz crystallographic preferred orientation: Geological Survey of Western Australia, Record 2024/3, 31p.

The seismicity of southwest Western Australia

RE Murdie

Scientific abstract

For a region far removed from tectonic boundaries, southwest Western Australia experiences an unusually large number of earthquakes. The largest of these intraplate events are recorded in the topographic features which are testament to the damage produced by large earthquakes over the past 3 Ma. In living memory, First Nations stories include Earth shaking events as part of their oral history. Earthquake monitoring started at the turn of the last century and has become more important as reliance on infrastructure affects the lives of more people in Western Australia.

KEYWORDS: craton, intraplate earthquakes, swarms

Lay abstract

Southwest Western Australia is remarkable for the number of small earthquakes which often happen in swarms of tens to hundreds of events lasting from weeks to months. Occasionally larger damaging earthquakes also occur as exemplified by the Meckering 1968 earthquake. Knowledge of the probability of location, magnitude and frequency has implications for building codes and emergency management.

Seismicity of southwest Western Australia

The SWAN project area is situated in continental crust of the Australian Plate and bounded by passive margins to the west and south with the Indian and Southern Oceans, respectively. Far to the north, the margin of the Australian Plate is the down-going slab at a convergent boundary with the Sunda Plate. However, the area of the SWAN deployment is within the stable continental area, far from areas of active tectonic displacements. The potential for earthquakes in continental regions is correlated with the seismic properties of the lithosphere. Under cratonic areas, lithospheric strength is generally high due to lower temperatures and dehydration in the lower crust and depleted lithospheric root (McKenzie and Priestley, 2016; Cawood et al., 2018). Hence, Archean and Paleoproterozoic cratons with cold, stable continental lithospheric roots generally have fewer crustal earthquakes with lower magnitudes than those in tectonically active areas or over pronounced lateral gradients in the lithosphere (Abbott et al., 2013).

This would suggest that the southwest of Western Australia is not an area expected to have many earthquakes. However, it is one of the most seismically active areas in Australia: the South West Seismic Zone (SWSZ; Everingham, 1965; Doyle, 1971) has many intraplate earthquakes (Fig. 7).

During the history of earthquake observation in Western Australia (since the 1900s), there have been six M6 or greater events (Table 2, Fig. 7). The Archean Yilgarn Craton is an ancient continent with an ancient topography. Its generally low-level undulating topography has fairly low (0.2 – 5 m/Ma) erosion rates (Belton et al., 2004;

Quigley et al., 2010). This has allowed assessment of the frequency of recurrence of large historic earthquakes by examining Neotectonic fault scarps, i.e. scarps formed over the past 5–10 million years (Clark, 2010). These are mainly oriented north–south, corresponding to the focal mechanisms of modern earthquakes which show east–west compression (Fig. 8; Lin et al., 2021). Since the Australian Plate is moving in a north-northeasterly direction, this compression direction is at a high angle to the plate motion, suggesting local factors play an important role in the seismicity as well as the large-scale plate tectonic forces.

In the Albany–Fraser Orogen, studies of the 2018 Lake Muir sequence showed a range of focal mechanisms reflecting the interplay of stresses acting on older structures and dykes (Clark et al., 2020; Lin et al., 2021; Standen et al., 2021).

The size of the Neotectonic scarps indicate that M7 events have happened in the region (Crone et al., 2003; Estrada-Roldan, 2008; Clark et al., 2012; Whitney et al., 2022), which has implications for seismic hazard. Many scarps are not in locations where contemporary seismicity has been recorded (Clark et al., 2012). This is a reminder that we have only been locating earthquakes for a short period of geological time and that the current earthquake locations are not necessarily indicative of where large events might happen in the future in Western Australia (Clark, 2010).

The most frequent occurrences of seismic activity in Western Australia are swarms of low-magnitude events that can consist of hundreds of events over several months;

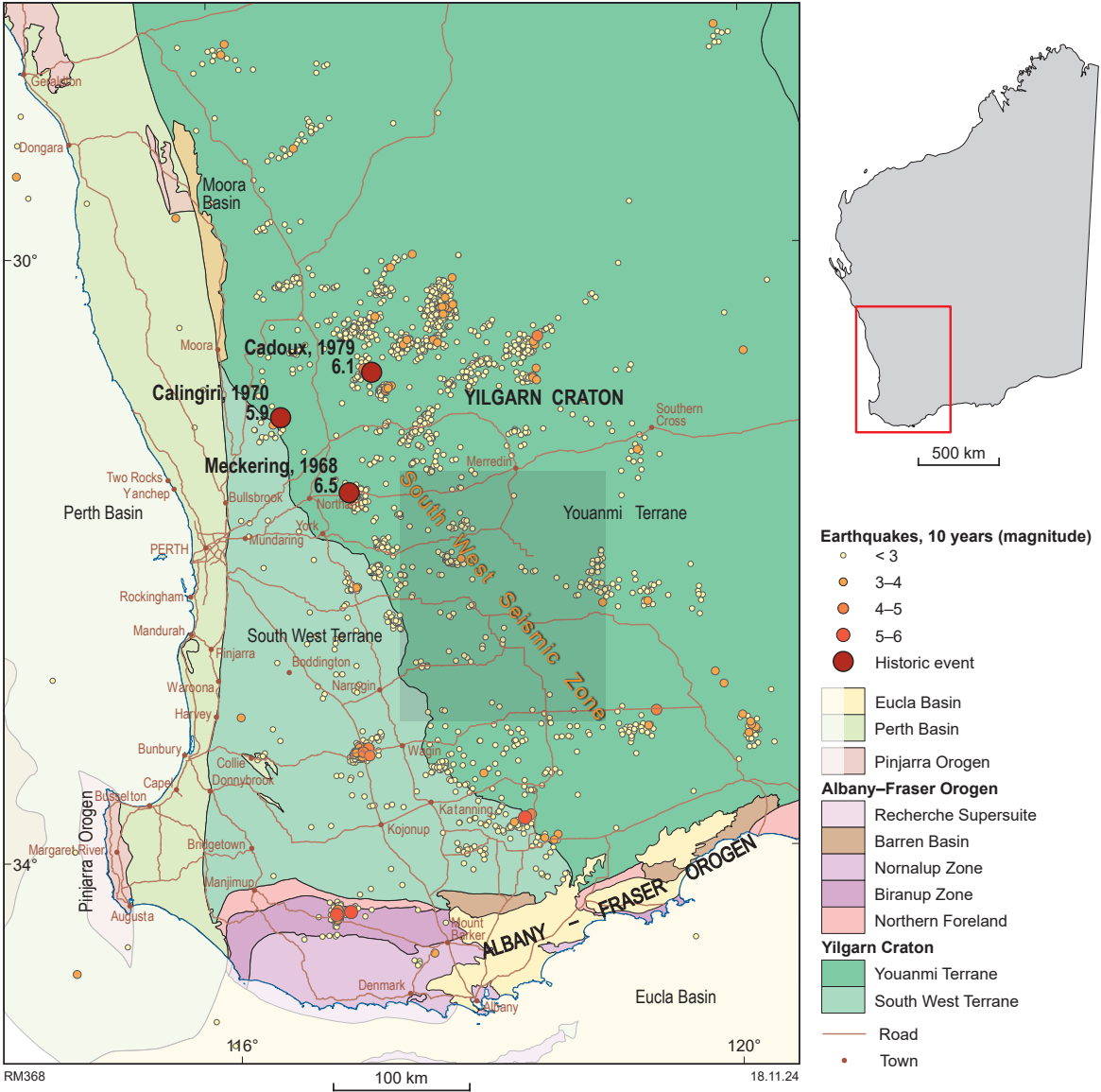


Figure 7. Earthquakes of southwest Western Australia for the period 2009 to 2020 as recorded by GA and the M> 6 events in historic times.

Table 2 M >6 events in Western Australia and other notable earthquakes recorded in Western Australia since mechanized recording began

Location	Latitude	Longitude	Depth	Magnitude	Date
Meeberrie	-26.92	115.8	0	6.3	April 1941
Derby WA	-17.71	123.16	33	5.9	March 1964
Meckering, WA.	-31.62	116.98	10	6.5	October 1968
West of Lake Mackay	-22.05	126.61	8	6	March 1970
Calingiri	-31.11	116.47	1	5.9	March 1970
Broome WA	-16.66	120.27	26	5.9	April 1974
Cadoux, WA.	-30.827	117.179	3	6.1	June 1979
Collier Bay, WA.	-16.0503	124.4227	10	6.2	August 1997
Kalgoorlie	-30.787	121.489	2	5	April 2010
Lake Muir	-34.315	116.759	3	5.7	Sept 2018
Offshore Broome	-18.2622	120.294685	20	6.6	July 2019

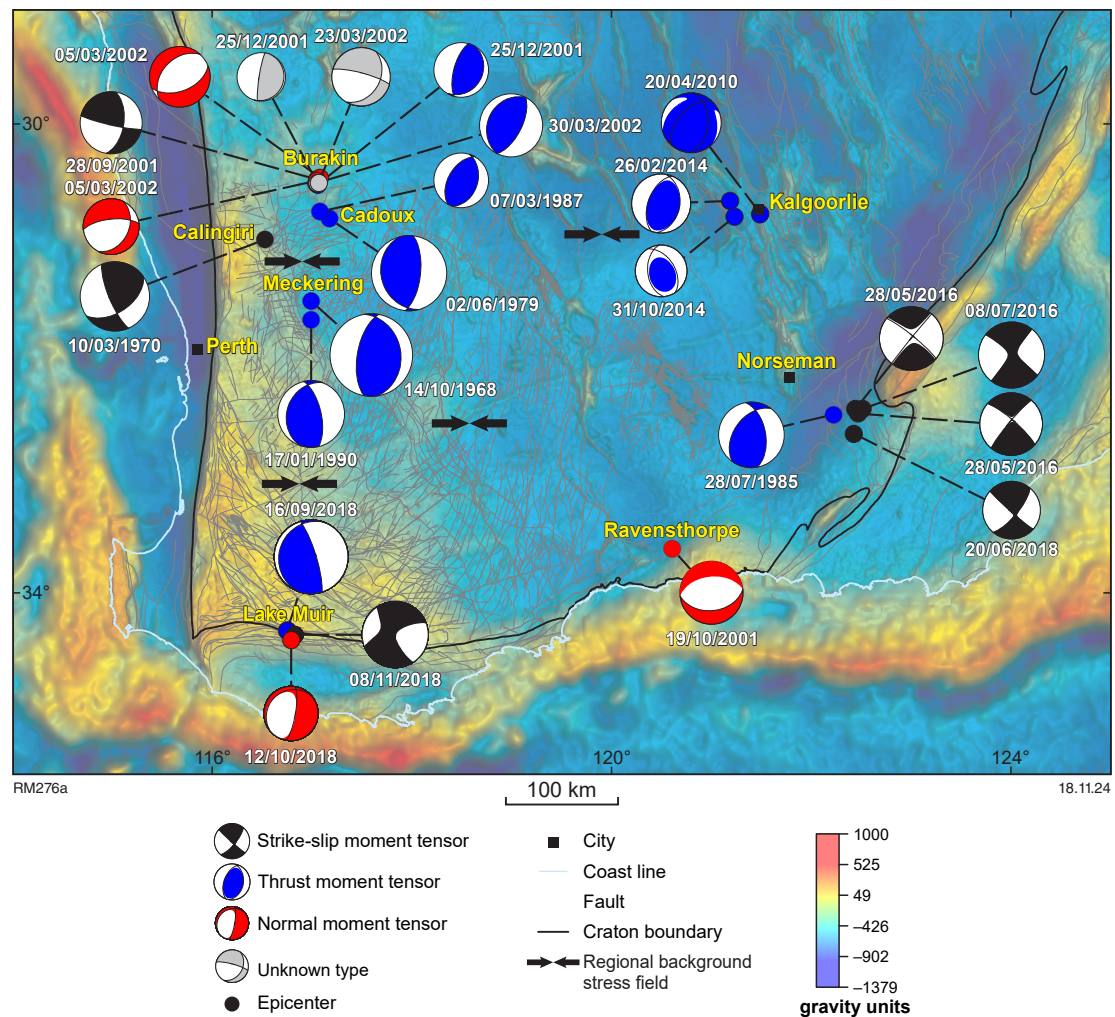


Figure 8. Focal mechanisms of selected earthquakes in southwest Western Australia after Lin et al. (2021) and Leonard et al. (2002)

for example, Burakin in 2001 (18 000 events in only a few months; Leonard, 2002) and Arthur River in 2022–23 (Murdie et al., 2022). Some swarms have associated mainshocks, such as the four events of M 4 or greater associated with the Arthur River swarm (Fig. 9). Others have no associated main shock.

Damage caused by these swarms is low, partly due to the low magnitude of the events, but also due to the low population density in these areas. However, the potential for disruptive damage is shown by the 1968 M 6.5 Meckering earthquake. This resulted in the formation of a 37 km-long and up to 2 m high scarp (Gordon and Lewis, 1980). Detailed mapping of the scarp showed that the location of Proterozoic dykes had affected the shape of the surface ruptures (Dentith et al., 2009). This ground motion affected not only on the local community (many buildings in Meckering township were completely destroyed) but also caused wider problems such as disrupting the main infrastructure and transport corridor between Perth and the eastern states by breaking the water pipe, the highway and the trainline (Johnson and White, 2018). This highlights the need to take seismic hazard in Western Australia seriously.

Notably, the Darling Fault, one of the largest faults and topographic features in Western Australia, does not appear to be seismically active, nor do faults at the northern edges

of the Yilgarn Craton. However, the southern and eastern margin with the Albany–Fraser Orogen does produce a number of events; for example, the Lake Muir events of 2017 (Fitzsimons, 2003; Standen et al., 2021).

Monitoring local seismicity is an obvious benefit to the local community. However, in the search for new mineral resources, knowledge of the deeper structure under Western Australia is also important, as determining the geometry of important boundaries in the crust and lithosphere can help identify features relevant to mineral systems. These include mantle-tapping faults (Hronsky, 2004; Begg et al., 2010; Walshe et al., 2014; McCuaig and Hronsky, 2017) and gradients in the lithosphere–asthenosphere boundary (Hoggard et al., 2020). These, in turn, help identify different geological domains and possible tectonic events which have affected the region, and hence the prospectivity.

Imaging this deep into the Earth is achieved by looking at the incoming energy from earthquakes that have happened elsewhere in the world. The Australian Plate is surrounded by active margins in the north and east and passive margins in the south and west (Fig. 10). Oceanic ridges are relatively quiet regarding seismic activity, but the Central Indian and the Southeast Indian Ridges under the Indian and Southern Oceans do release a number of M > 5 events that have been recorded by SWAN.

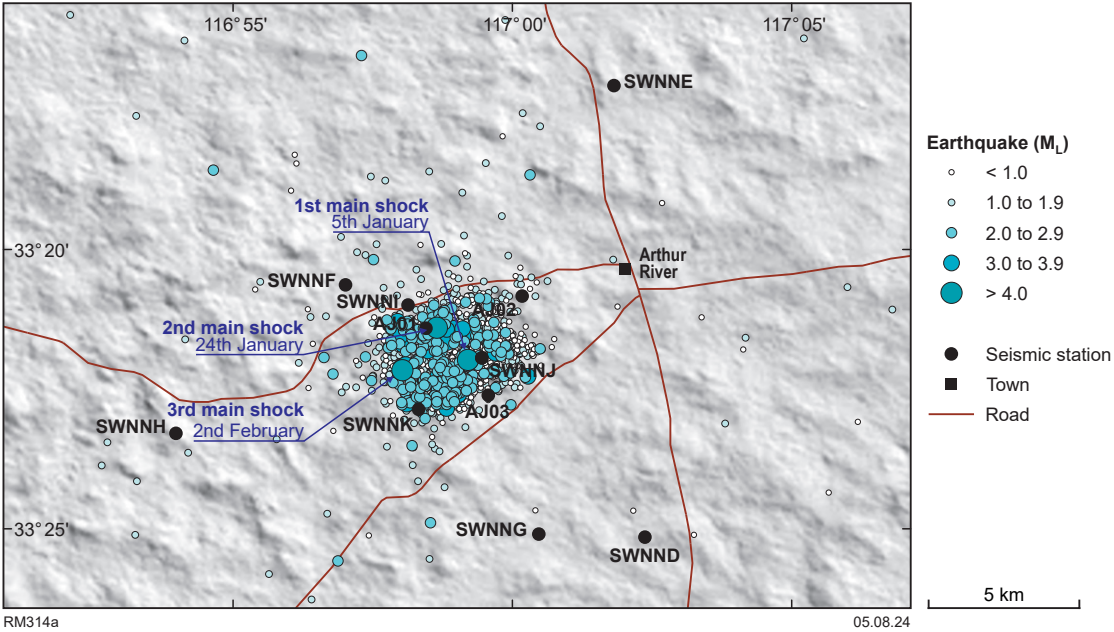


Figure 9. The Arthur River swarm. Earthquake locations as determined by using the ANSN, AuSIS, SWAN and a set of rapid deployment stations from 10 to 27 June 2022

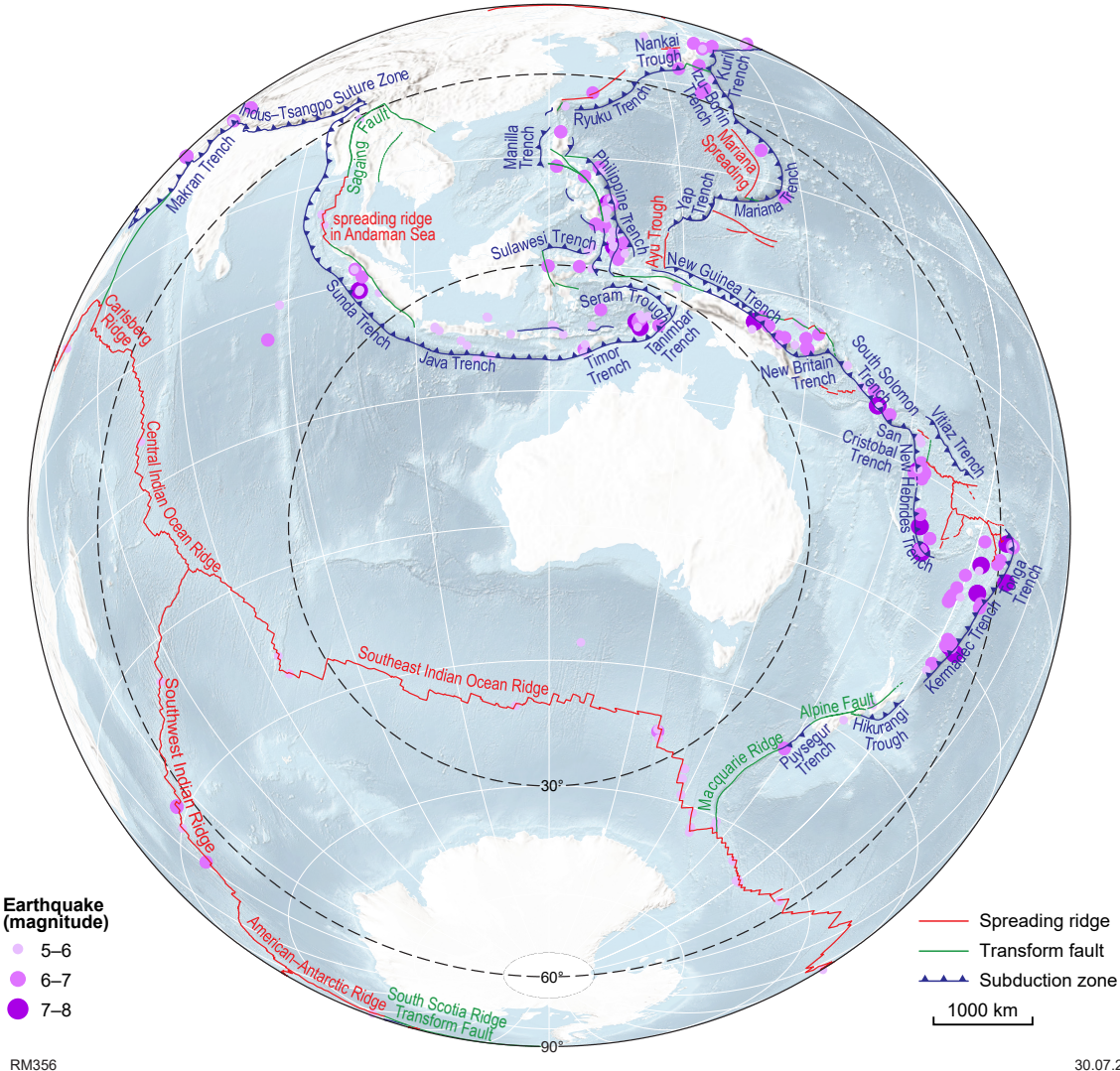


Figure 10. Tectonic features surrounding the Australian continent which produce earthquakes large enough to register in Western Australia

The main source of earthquakes close to Australia are the subduction zones along the northern and eastern margins (Fig. 10). Regions farther afield, such as the Philippines and Japan, also produce earthquakes useful for seismic imaging in Western Australia. Methods such as seismic anisotropy use earthquakes that have travelled through the core of the Earth before arriving at Western Australia.

Techniques using these teleseismic events are detailed in the following sections on ambient noise, P-wave tomography and receiver functions.

References

- Abbott, DH, Mooney, WD and Vantongerren, JA 2013, The character of the Moho and lower crust within Archean cratons and the tectonic implications.: *Tectonophysics*, v. 609, p. 690–705, doi:10.1016/j.tecto.2013.09.014.
- Begg, GC, Hronsky, JMA, Arndt, NT, Griffin, WL, O'Reilly, S and Hayward, N 2010, Lithospheric, cratonic, and geodynamic setting of Ni-Cu-PGE sulfide deposits: *Economic Geology*, v. 105, p. 1057–1070.
- Belton, DX, Brown, RW, Kohn, BP, Fink, D and Farley, KA 2004, Quantitative resolution of the debate over antiquity of the central Australian landscape: implications for the tectonic and geomorphic stability of cratonic interiors: *Earth and Planetary Science Letters*, v. 219, no. 1–2, p. 21–34, doi:10.1016/S0012-821X(03)00705-2.
- Cawood, PA, Hawkesworth, CJ, Pisarevsky, SA, Dhuime, B, Capitanio, FA and Nebel, O 2018, Geological archive of the onset of plate tectonics: *Philosophical Transactions of the Royal Society A: Mathematical, Physical and Engineering Sciences*, v. 376, article no. 0170405, 30p., doi:10.1098/rsta.2017.0405.
- Clark, D 2010, Identification of Quaternary scarps in southwest and central west Western Australia using DEM-based hill shading: application to seismic hazard assessment and neotectonics: *International Journal of Remote Sensing*, v. 31, no. 23, p. 6297–6325, doi:10.1080/01431161003631592.
- Clark, D, McPherson, A and van Dissen, R 2012, Long-term behaviour of Australian stable continental region (SCR) faults: *Tectonophysics*, 566–567, p. 1–30.
- Clark, DJ, Brennand, S, Brenn, G, Garthwaite, MC, Dimech, J, Allen, TI and Standen, S, 2020, Surface deformation relating to the 2018 Lake Muir earthquake sequence, southwest Western Australia: new insight into stable continental region earthquakes: *Solid Earth*, v. 11, p. 691–717, doi: 10.5194/se-11-691-2020.
- Crone, AJ, Martini, PM de, Machette, MN, Okumura, K and Prescott, JR 2003, Paleoseismicity of two historically quiescent faults in Australia: Implications for fault behavior in stable continental regions: *Bulletin of the Seismological Society of America*, v. 93, no. 5, p. 1913–1934, doi:10.1785/0120000094.
- Dentith, MC, Dent, VF and Drummond, BJ 2000, Deep crustal structure in the southwestern Yilgarn Craton, Western Australia: *Tectonophysics*, v. 325, p. 227–255.
- Doyle, HA 1971, Australian seismicity: *Nature Physical Science*, v. 234, no. 52, p. 174–175, doi:10.1038/physci234174a0.
- Estrada-Roldan, B 2008, Neotectonic and palaeoseismologic studies in the south-west of western Australia: University of Western Australia, Western Australia, PhD thesis (unpublished).
- Everingham, IB 1965, The crustal structure of the south-west of Western Australia: Bureau of Mineral Resources, Geology and Geophysics, Record 1965/97.
- Fitzsimons, ICW 2003, Proterozoic basement provinces of southern and southwestern Australia, and their correlation with Antarctica: Geological Society, London, Special Publications, v. 206, p. 93–130.
- Gordon, FR and Lewis, JD 1980, The Meckering and Calingiri earthquakes October 1968 and March 1970: Geological Survey of Western Australia, Bulletin 126, 229p.
- Hoggard, MJ, Czarnota, K, Richards, FD, Huston, DL, Jaques, AL and Ghelichkhan, S 2020, Global distribution of sediment-hosted metals controlled by craton edge stability: *Nature Geoscience*, v. 13, no. 7, p. 504–510, doi:10.1038/s41561-020-0593-2.
- Hronsky, JMA 2004, The science of exploration targeting, in SEG 2004: Predictive mineral discovery under cover edited by J Muhling: The University of Western Australia, Centre for Global Metallogeny, Publication, p. 129–133.
- Johnston, JF and White, SR 2018, Understanding the Meckering earthquake: Western Australia, 14 October 1968: Geological Survey of Western Australia, 26p.
- Leonard, M 2002, The Burakin WA earthquake sequence Sept 2000 - June 2002, in Australian Earthquake Engineering Society Conference 2002 edited by MC Griffith, D Love, P McBean, A McDougall and B Butler: AEES 2002, Adelaide, South Australia: Australian Earthquake Engineering Society, Total risk management in the privatised era, p. 22.
- Lin, X, Yuan, H, Dentith, MC, Murdie, R, Gessner, K and Nayak, A 2021, Improved full waveform moment tensor inversion of cratonic intraplate earthquakes in southwest Australia: *Geophysical Journal International*, v. 227, no. 1, p. 123–145, doi:10.1093/gji/ggab214.
- McCuaig, TC and Hronsky, JMA 2017, The mineral systems concept: the key to exploration targeting: *Applied Earth Science*, v. 126, no. 2, p. 77–78, doi:10.5382/SP.18.08.
- McKenzie, D and Priestley, K 2016, Speculations on the formation of cratons and cratonic basins: *Earth and Planetary Science Letters*, v. 435, p. 94–104, doi:10.1016/j.epsl.2015.12.010.
- Murdie, RE, Pickle, R, Yuan, H, Love, D, Dent, V, Miller, MS and Whitney, J 2022, Observations from the 2022 Arthur River, Western Australia, Earthquake Swarm, in 2022 National Conference proceedings, Mount Macedon, Victoria, 24–25 November: Australian Earthquake Engineering Society, 11p.
- Quigley, MC, Clark, D and Sandiford, M 2010, Tectonic geomorphology of Australia, in Australian landscapes edited by P Bishop and B Pillans: The Geological Society of London, Special Publication, v. 346, p. 243–265.
- Standen, S, Dentith, M and Clark, D 2021, A geophysical investigation of the 2018 Lake Muir earthquake sequence: reactivated Precambrian structures controlling modern seismicity: *Australian Journal of Earth Sciences*, v. 68, no. 5, p. 717–730, doi:10.1080/08120099.2021.1848924.
- Walshe, JL, Bath, AB, Cloutier, J and Hough, RM 2014, High-grade Au deposits: Processes to prediction: Geological Survey of Western Australia, Report 145, 183p.
- Whitney, B, Hengesh, J and Clark, D 2022, Age constraints on surface deformation recorded by fossil shorelines at Cape Range, Western Australia: Comment: *Bulletin of the Geological Society of America*, v. 134, no. 5–6, p. 1614–1620, doi:10.1130/B36135.1.

SWAN deployment

RE Murdie, H Yuan and R Pickle¹

1. Research School of Earth Sciences, The Australian National University, Acton ACT 0200

Scientific abstract

Earthquake monitoring for the South West Australia Network (SWAN) passive seismic monitoring project started in September 2020. The complete network of 27 stations comprised instruments deployed specifically for this project, and permanent stations of the Australian National Seismograph Network and the Seismometers in Schools projects. Seven additional seismometers were deployed in a high-density network in response to a swarm of earthquakes in the Arthur River region.

KEYWORDS: Australian National University, Department of Fire and Emergency Services, deployment, seismometer, Western Australia

Lay abstract

The South West Australia Network (SWAN) passive seismic monitoring project ran from 2020 to 2023 in southwest Western Australia. Twenty-seven temporary and permanent seismometers were used to gather data across the region for the full period of deployment, and additional seismometers were deployed at short notice to monitor aftershocks from a swarm of earthquakes in the Arthur River region.

South West Australia Network (SWAN) stations

Deployment for the South West Australia Network (SWAN) started in September 2020. This was during the COVID pandemic when state borders were closed and no scientists from The Australian National University (ANU) or Geoscience Australia (GA) were able to participate in the initial deployment. However, as the project progressed, the border restrictions were eased and all staff members were able to visit the sites.

For their part in the project, Western Australia's Department of Fire and Emergency Services (DFES) facilitated locations for the deployment of seismic stations. They coordinated with the regional Bush Fire Brigades, including the use of sites around local bushfire sheds. However, some bushfire sheds were too exposed, creating a potential for the seismic station to be either driven over or stolen, so alternative locations were found. Two stations (SWN15, SWN20) re-occupied sites which had previously been used during the for the Lake Muir swarm aftershock campaign in 2018 (Allen et al., 2019).

Twenty-seven stations in total were installed (Fig. 11). Twenty-four comprised ANU TerraSAWR digitisers and Nanometrics trillium compact 120s or posthole seismometers provided by AuScope. Three stations were Güralp 6TDs provided by GSWA. All stations were installed in a hole a spade depth down, and the base of the hole was lined with bricklaying sand. The seismometer was placed on a terracotta plate which had been pushed into the sand

(Fig. 12a). The seismometer was oriented, levelled, enclosed in a plastic bag, covered with an inverted tub and buried. The digitiser with an integral battery and GPS was placed on the surface, next to the seismometer, wrapped in a tarpaulin and covered with a thin layer of soil, so that the GPS signal was not obscured but the digitiser box did have some protection from the heat. All stations had a 10 W external solar panel to keep the battery charged (Fig. 12b) and, in most cases, this provided continuous power. Data were set to record at 250 Hz.

Stations were visited every six months to download data. The project, initially scheduled for two years, was extended to three years because funds were still available in the budget. By this time a larger project, WA Array (Murdie et al., 2024), was starting. SWAN stations that coincided with WA Array were kept running as late as November 2023. Other stations were removed starting from November 2022.

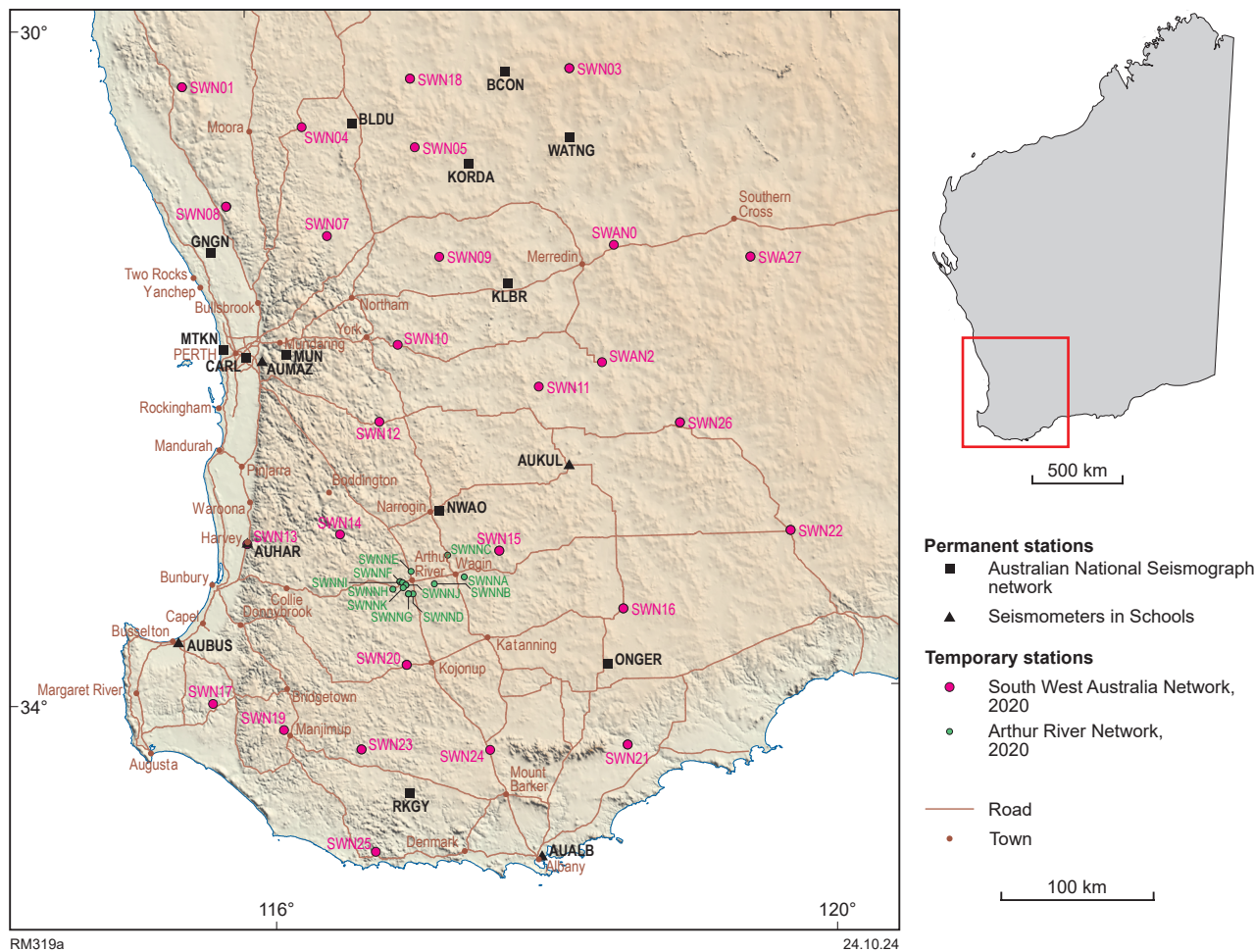


Figure 11. Location of the ANSN and AuSIS seismic stations active at the time of the SWAN project, SWAN array, and Arthur River aftershock monitoring stations



Figure 12. Field photos of SWAN seismometer setup: a) components of a seismic station as it is being installed, including a protective tub that will cover the seismometer before being buried, solar panel, digitizer and seismometer in the hole on a terracotta plate; b) installed seismic station at Quindanning Bush Fire Shed

Arthur River rapid deployment stations

During the monitoring period of the SWAN array, an earthquake M4.0 hit the community of Arthur River. GSWA was able to provide an aftershock monitoring kit of seven additional SmartSolo BD3C-5 seismometers (Fig. 13). These were progressively moved across 11 different sites for approximately 10 months with the aim of monitoring the aftershocks and, as it happened, two further main shocks, and to see if we could image a fault plain (Pickle et al., 2024).

Permanent stations in the region

Australian National Seismograph Network (ANSN)

The Australian National Seismograph Network (ANSN) is the permanent network of stations in Western Australia and is run by GA (Costelloe et al., 2016) with additional inputs from GSWA. There are 12 stations in southwest Western Australia (Fig. 11) sending data to the National Alerts Centre in Canberra. Station NWA0 is an international station, and is

an auxiliary station for the Comprehensive Nuclear Test Ban Treaty Organisation Homepage | CTBTO, so is built to very high standards and, therefore, provides high-quality data.

Australian Seismometers in Schools (AuSIS)

The Australian Seismometers in Schools (AuSIS) network is a program run by AuScope, which puts seismometers in schools as an educational outreach program. These instruments have a narrower band width; they have a sensitivity which has maximum period is 30 s compared to the broadband stations which have a maximum period of 120 s as preferred for use in SWAN. Also, during the day, the AuSIS stations can be very noisy. There are five AuSIS stations in southwest Western Australia (Fig. 11).

Conclusions

This deployment set the scene for a comprehensive three-year monitoring project which provided the best-resolution data so far in Western Australia. Data from the network were used to provide high-resolution models as described in the following sections of this Report.

References

- Allen, TI, Clark, D, Lawrie, S, Brenn, G, Dimech, J, Garthwaite, M, Glanville, H, Kemp, T, Lintvelt, C, Lumley, D, Pejic, T, Sayin, E and Standen, S 2019, The 2018 Lake Muir earthquakes: Australia's ninth surface rupturing earthquake sequence in 50 years: *Seismological Research Letters* v. 90, p. 951.
- Costelloe, M, Bugden, C, Bathgate, J, Wang, L, Lewis, A, Jones, B, Li, Y, Butterfield, A, Becher, S, Ruysenaers J, McLauchlan L, Burke, P, Jacka, R, Eacott, D and Barton, T 2016, Geoscience Australia's Geophysical Network: critical infrastructure and observed and derived data for earth monitoring and community safety: *ASEG Extended Abstracts*, 2016, v. 1, p. 1–5, doi:10.1071/ASEG2016ab226.
- Murdie, RE, Yuan, H, O'Donnell, JP, Johnson, SP, Ebrahimi, R, and Rashidifard, M 2024, WA Array: A high-resolution passive-source seismic survey to image the West Australian lithosphere, *Seismological Research Letters*, v. 95, no. 5, p. 3093–3108, doi:10.1785/0220230415.
- Pickle, R, Miller, MS, Murdie, RE and Allen, TI 2024, A detailed earthquake catalogue for southwest Australia 2020–23 using data from the SWAN and WA Array networks, *in* South West Australia Network (SWAN): passive seismic imaging and hazard analysis *compiled by* RE Murdie and MS Miller: Geological Survey of Western Australia, Report 255, p. 22–29.



Figure 13. Installation of a SmartSolo seismometer at Arthur River aftershock monitoring site SWNNB at Warup

A detailed earthquake catalogue for southwest Australia 2020–23 using data from the SWAN and WA Array networks

R Pickle¹, MS Miller¹, RE Murdie and TI Allen²

1. Research School of Earth Sciences, The Australian National University, Acton ACT 0200

2. Geoscience Australia, Symonston ACT 2609

Scientific abstract

The southwest (SW) region of Australia continues to experience persistent low-magnitude seismicity punctuated by ~ 27 M_w 5 or greater events over the last 100 years; including many of the largest earthquakes in recorded Australian history. The region also experiences regular large-volume, long-duration earthquake swarms. Investigations of prehistoric scarp offsets have also indicated that events may approach magnitudes of M_w 7.25 (Leonard and Clark, 2011). As the nearest plate boundary is over 2000 km away, the reason for these high levels of seismicity is poorly understood. To investigate this activity, two significant seismic networks have been deployed targeting this area: SWAN (2P, 27 stations, 2020–23) and WA Array (WG, 100+ stations, 2023–33). Prior to this, the region only had limited coverage provided by the Australian Seismometers in Schools (AuSiS, S1) and national networks (AU), as well as several small, temporary networks dating back to 2000. This study utilised data collected during the SWAN and WA Array deployments to derive a new earthquake catalogue using a modified version of EQTransformer (Mousavi et al., 2020), a machine learning phase picker. During the SWAN deployment, a significant earthquake swarm near Arthur River began in early 2022 and showed signs of continued activity through the end of 2023. In total over 12 400 events were discovered from September 1 2020 to December 20 2023, including many from known mining sites. The estimated magnitude of completeness for this catalogue is around M_{La} 2.0.

KEYWORDS: earthquakes, machine learning, swarms, seismic hazard

Lay abstract

The southwest region of Australia experiences regular imperceptible seismicity, as well as dozens of magnitude 3 or higher events per year and the occasional magnitude 5 or greater event. It has also seen many of Australia's most damaging earthquakes on record. Geological features, such as fault scarps, may also indicate that earthquakes capable of magnitude 7.25 are possible in this region. The exact cause of these earthquakes is still unknown. To investigate this seismicity, two distinct but collaborative seismic experiments were conducted between 2020 and 2023: the South West Australian Network and WA Array. The data collected from the seismometers deployed was analysed by a sophisticated 'deep-learning' algorithm to uncover over 12 400 earthquakes during the term of these projects. This work also observed a large earthquake 'swarm' which began in the Arthur River region on January 5 2022 and may still be ongoing.

Introduction

The southwest region of Australia is the country's most seismically active, and experiences persistent low-magnitude seismicity, punctuated by ~ 27 M_w 5 or greater events over the last 100 years, including the 1968 M_w 6.5 Meckering earthquake (Gordon and Lewis, 1980; Vogfjörð and Langston, 1987). The region also experiences regular long-duration earthquake swarms, including up to ~ 16 000 events in the Burakin region during 2001–02 (Leonard 2002), ~ 900 events following the Lake Muir sequence in 2018 (Clark et al., 2020; Standen et al., 2021), and nearly 3000 events in the Arthur River region beginning on January 5 2022 (Murdie et al., 2022). Investigations of prehistoric scarp offsets have also indicated that earthquakes may approach magnitudes of M_w 7.25 (Leonard and Clark, 2011). Given that southwest Australia is over 2000 km from the nearest plate boundary, there is no clear

explanation for these intracontinental earthquakes. To investigate this activity, two significant networks have been deployed here: SWAN (2P, 27 stations, 2020–23) and WA Array (WG, 100+ stations, 2023–33). The goal of these networks is to generate a detailed earthquake catalogue in addition to other seismic data products. Prior to this, the region only had limited coverage provided by the Australian Seismometers in Schools (AuSiS, S1) and national networks (AU), and several small temporary networks dating back to 2000.

Data

This catalogue used newly collected seismic data from the SWAN (South West Australia Network, 2P, Miller et al., 2023)

and WA Array (Western Australia Array, WG; Murdie et al., 2024) networks, as well as the AuSIS (Australian Seismometers in Schools, S1; Salmon et al., 2011), AU (Australian National Seismograph Network; Geoscience Australia, 2021), and IU (Global Seismograph Network, Albuquerque Seismological Laboratory; USGS, 2014) permanent networks. Some select stations from the AusArray Transportable Array (OA, Geoscience Australia; 2017) were also used in 2023 (Fig. 14).

The 27-station SWAN network was the first to attempt uniform spatial coverage of the area, and the 160+ station WA Array expanded on these sites with an attempted 40 km grid spacing. Both the SWAN, AusArray (2 degree spacing), and WA Array stations used broadband sensors exclusively and primarily those with corner frequencies of 120 s. After the Arthur River swarm began in early 2022, seven additional SmartSolo 5s BD3C-5 nodes were rotated across 11 different sites for ~10 months to further constrain these

earthquakes. In total, over 85 000 station-days of data were analysed from September 1 2020 to December 20 2023, with ~80% of this volume accounted for by the SWAN and WA Array networks.

Method

Machine learning phase picking

We employed a machine learning based seismic phase picker using an edited version of the EQTransformer (Mousavi et al., 2020) package. This code is trained on a catalogue of ~1.18M global earthquakes from the Stanford Earthquake Dataset (STEAD, Mousavi et al., 2019) and ~0.4M events from the Italian Seismic Dataset for Machine Learning (INSTANCE, Michelini et al., 2021), which has been

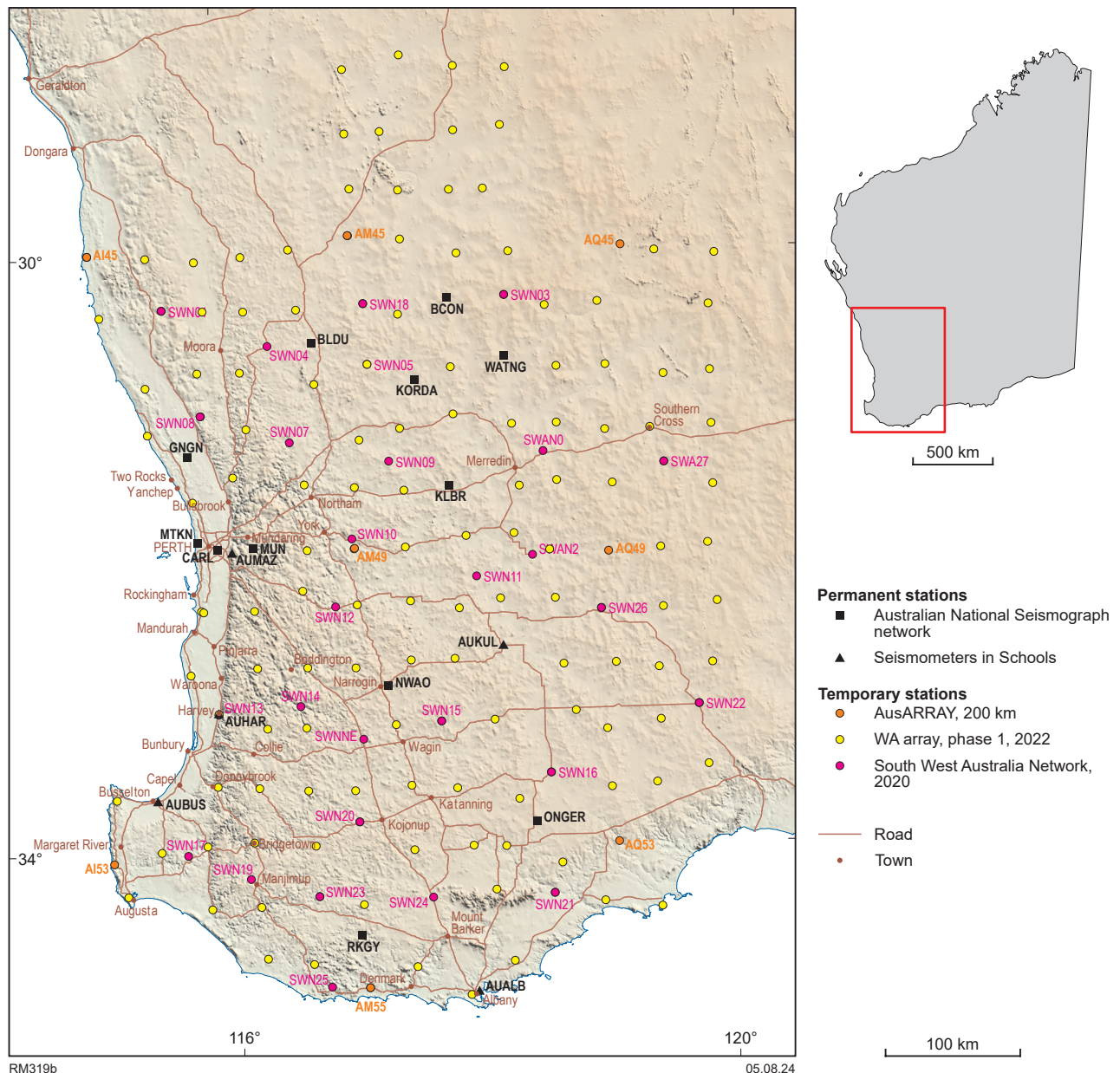


Figure 14. Location of the ANSN and AuSIS seismic stations active at the time of the SWAN project, SWAN array and WA Array

primarily filtered to exclude events with either a depth or epicentral distance >300 km. Machine learning phase pickers are able to identify P- and S-wave arrivals of earthquakes or other events by identifying similarities and assigning probabilities between waveforms against the vast quantities of 'known' P- and S-wave arrivals. In this way a trained model can detect low signal-to-noise (SNR) events using frequency analysis, correlation between P and S signatures, and other non-traditional ways that amplitude-based pickers cannot.

Association

Phase picks are initially associated with events using the REAL algorithm (Zhang et al., 2019). The code uses a 1D velocity model defined by averaging vertical velocity profiles from the 3D AuSREM crustal model (Salmon et al., 2012) beneath each local station. Events required at least seven total phase picks with the number of P >2 , S >2 , with at least two stations having both a P- and S-phase pick.

Location

The prototype earthquake catalogue from REAL was then relocated using the NonLinLoc algorithm (Lomax et al., 2009; Lomax et al., 2000) and a 3D velocity model (e.g. AuSREM; Salmon and Kennett, 2012). The starting AuSREM velocity model was refined to a resolution of 3 km^3 from its original 5 km depth and 0.5 degree horizontal resolution.

In addition to the minimum phase pick arrivals implemented during the association stage, arrivals at stations with a distance greater than 3.0 degrees from the epicentre were removed completely, and stations with a distance further than 2.0 degrees were not counted towards the minimum pick requirements but kept in the solution. At least four phase picks at stations nearer than 1.5 degrees must also be present for an event to not be rejected.

The NonLinLoc location algorithm was executed multiple times for each event. After the first iteration, arrivals with residuals >1.5 seconds or solver weights <0.05 were removed and the solver was run again. At this point, estimated arrivals at all unpicked stations within 1.8 degrees of the epicentre were calculated using a simple 1D velocity model, re-windowed into 60 second windows, and re-picked using the same trained ML picker. In practice, this recovers phase picks for events that may have been bisected or otherwise lost by the 60 second windowing done during the initial ML picking run. Any new picks within 2 seconds of their predicted arrivals were added to our preliminary event and NonLinLoc was run a second time.

After the second NonLinLoc run, picks with residuals >1.5 seconds or weights <0.05 were again removed. At this stage, we also cross-referenced these potential picks with a collection of predicted phase arrivals from global teleseismic events at <180 degrees and with magnitude $M_w >5.5$, and removed any picks within 10 seconds of these predicted teleseismic arrivals. If the number of dropped picks was greater than 5% of the total, NonLinLoc was run a third time with the same residual and weight filter. If the final number of contributing phase picks fell below 8, the event was rejected. Furthermore, if any of the north-east-vertical (N-E-Z) positional uncertainties were greater than 10 km, or the event RMS was greater than 1.5 seconds, or the event

had an azimuthal gap greater than 330 degrees, the event was rejected.

Catalogue review

Our last automatic QC step was to create a database of all stations with existing data for each day of our experiment and then calculate various metrics to reduce the prevalence of rogue phase arrivals, which may have low residuals but are not associated with any event.

First, we calculated the ratio of stations with associated phase arrivals relative to the number of stations with existing data within the same radius (here set to the minimum of the distance of the furthest arrival or two degrees). Any events with a ratio of existing to possible contributing stations below 0.333 were removed. Second, we also calculated an existing-to-possible comparison of azimuthal gaps. If the azimuthal gap calculated using existing arrivals was more than 90 degrees lower than the possible maximum azimuthal gap, the event was removed. These checks greatly reduced the volume of non-existent and severely mislocated events.

Our catalogue was then subjected to clustering analysis using the scikit-learn python package (v 1.5.1; <https://scikit-learn.org/stable/>) to identify and rank the 3D spatial correlation of events. Depending on the network geometry, station density and the volume of an earthquake catalogue, events occurring in locations removed from the proximity of others have a high probability of being non-existent, unresolvable or otherwise too poorly constrained to be viable. Events with a lower event density score were subjected to stricter quality control parameters and those in the bottom tenth percentile were reviewed manually.

Finally, we conducted systematic manual reviews by considering events with unlikely depths (e.g. deeper than 10 km) and events with a disparate number of phase arrivals given their magnitude. Events for larger or notable events were also reviewed to ensure picks were as accurate as possible. Manual reviewing was performed using SeisComp (www.seiscomp.de), with hypocentres then recalculated as needed using the NonLinLoc plugin and the same 3D velocity model. The final step was to apply the 'scrtdd' double differencing algorithm (e.g. Grigoli et al., 2022).

Overall, we deployed a conservative quality control scheme rather than create a catalogue with as many events as possible. There were two key reasons for this. First, southwest Australia is already a highly active zone, so areas of high seismicity will be clear regardless. Second, we expect that one of the primary use cases for this catalogue will be in hazard analysis as well as tomographic studies, so it is imperative that as few spurious events exist in the catalogue as possible.

Earthquake catalogue

Our final catalogue comprised 12 414 events from 1 September 2019 to 20 December 2023, with average latitude, longitude and depth uncertainties of 1.6, 1.8 and 3.2 km, respectively, an average RMS error of 0.446 seconds, and a mean of 30.4 P- and S-phase picks per event (Fig. 15).

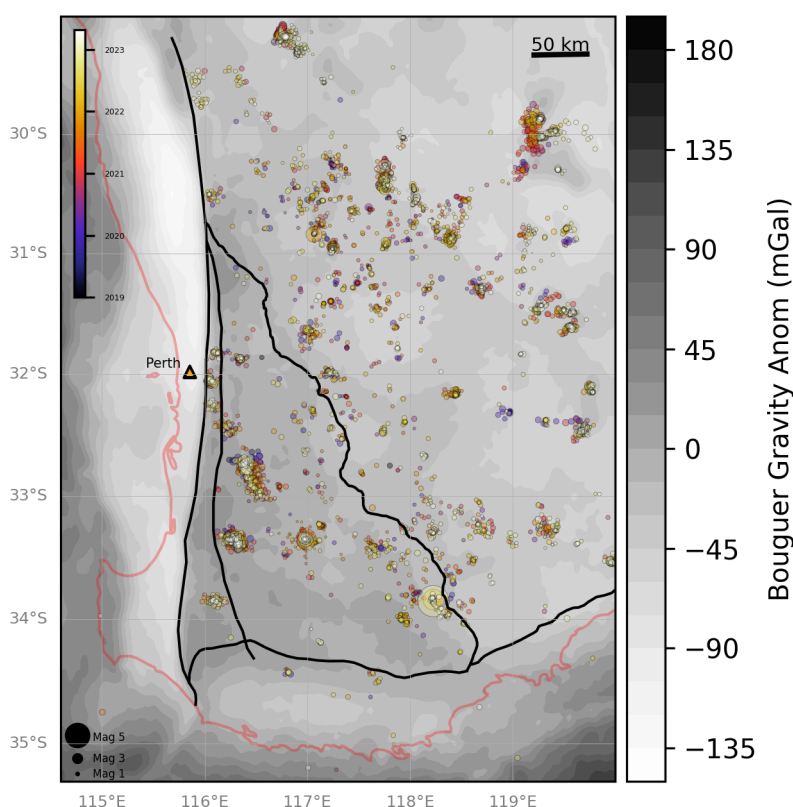


Figure 15. Map of located events. Colours indicate origin time from 2019 to late 2023. Events following WA Array deployment in late 2022 tend to have better constrained locations due to the high number of active stations

Many of these events, primarily at the western and eastern margins of the map, likely correspond to quarry blasts typically associated with precious metals mining. Most (63%) of these events were found to exist within clustered (radius <0.05 degrees) regions, and 17% of the total catalogue are likely associated with mining activity. We note that many events within the clusters around mines may be naturally occurring earthquakes, particularly those with origin times outside of regular working hours.

Magnitude calculation and completeness

M_{La} (Geoscience Australia) magnitudes were calculated for each event using the SeisComp 'scamp' and 'scmag' codes. These calculated regional event arrival amplitudes and magnitudes on the vertical data channel. This technique follows from the original Richter magnitude formula by removing the instrument response from the signal and replicating the behaviour of a Wood-Anderson seismometer. No filtering was done on the waveforms beforehand, and at least two valid station estimates were required to derive a magnitude. Magnitude estimates were computed by taking the mean of all station solutions with outliers beyond the 12.5 percentile removed; for example, the default configuration in SeisComp.

The magnitude completeness of the events in our catalogue are shown below in Figure 16. The catalogue is more-or-less complete (i.e. we have likely found all possible events) to $M_{La} \sim 2.0$, illustrated by the peak of events per magnitude data overlain in green. The linear distribution of the events—

phases data plotted in blue indicates a roughly logarithmic proportionality between the volume of detected events given a minimum number of associated phases, echoing the general expectation that smaller events will be detected by fewer stations.

Figure 17 shows a comparison between the national catalogue (which primarily uses the AU and S1 networks) and this catalogue. For events larger than $M_{La} 3$, both catalogues closely track each other but begin to diverge below $M_{La} 2.75$. This suggests a magnitude of completeness of around 2.75 or 3.0 M_{La} for the national catalogue for SW Australia. It is otherwise no surprise that our catalogue has found more events at lower magnitudes as the SWAN and WA Array networks incorporate nearly 170 additional stations. Furthermore, our catalogue and the data in Figures 16 and 17 include thousands of known quarry blast sites, whereas the national catalogue does not. Both the mean and median M_{La} magnitude of mining-related events was 2.04.

Event clustering and the 2022–23 Arthur River swarm

The events in Figure 15 mostly (63%) present as clusters of tens to thousands of events. We deployed the DBSCAN clustering algorithm in the scikit-learn python package (v 1.5.1; <https://scikit-learn.org/stable/>) to systematically locate 42 clusters (Fig. 18, blue circles) where 40 or more events exist within an epsilon radius of 0.05 degrees. Areas of known or inferred mining activity are shown by green circles. Many of these correlate with the clusters defined via DBSCAN; however, some fall below the threshold for detection.

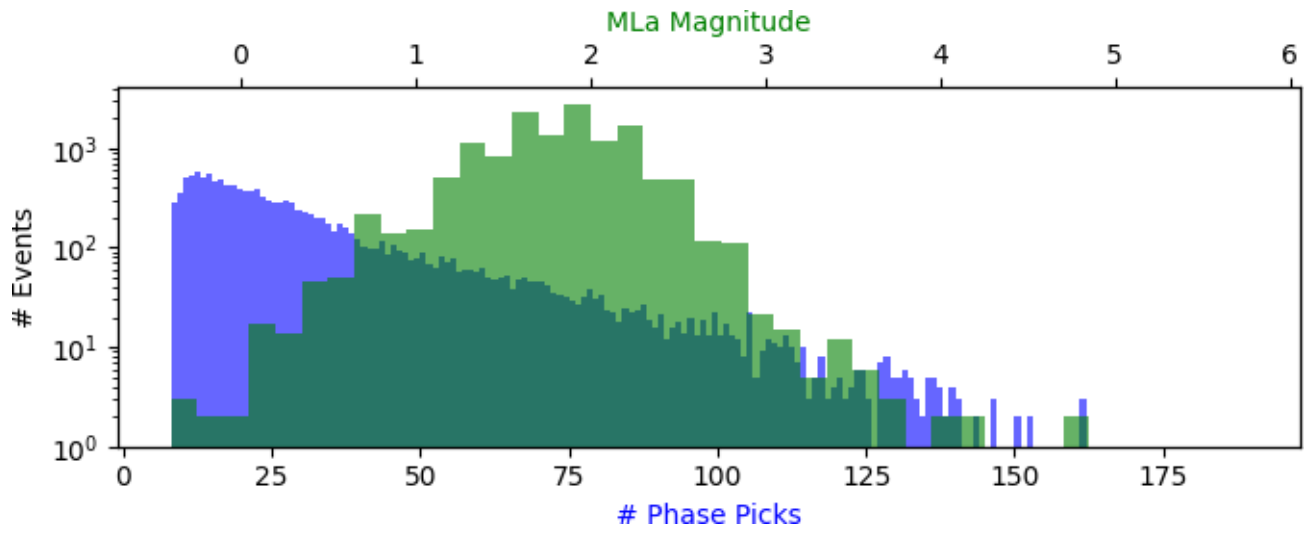


Figure 16. M_{La} magnitude vs number of events (green) and number of phase picks per event vs number of events (blue). The magnitude of completeness appears to be around M_{La} 2.0

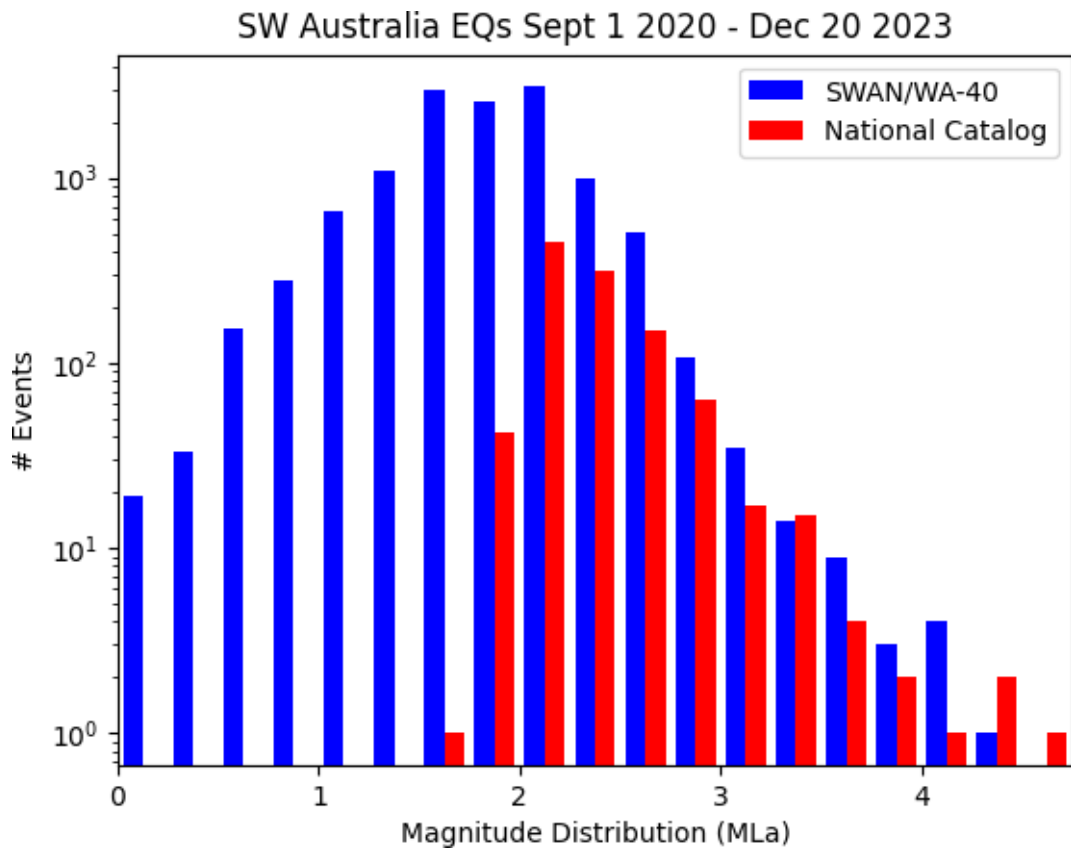


Figure 17. M_{La} magnitude distribution vs number of events for both this catalogue and the national catalogue

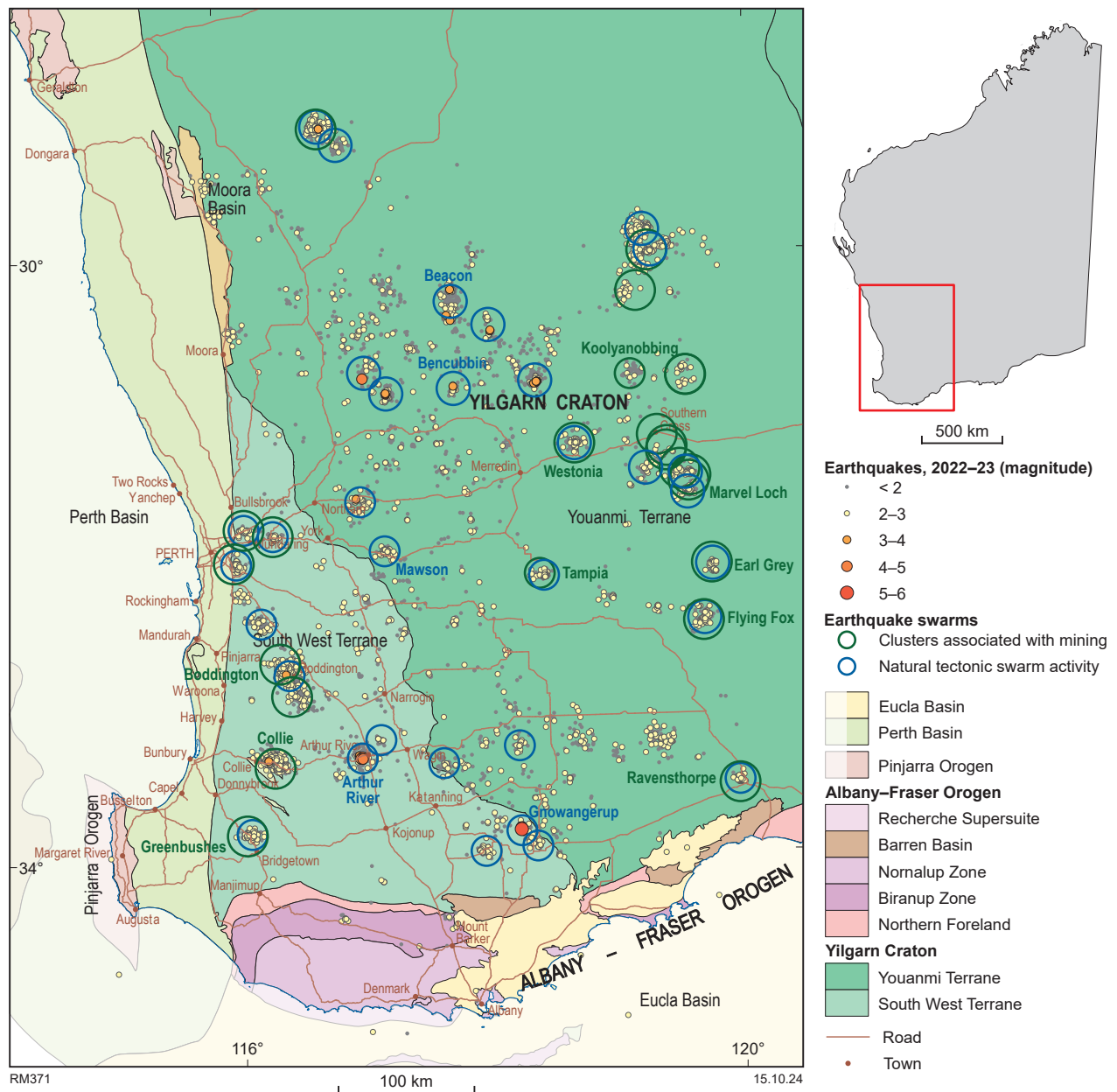


Figure 18. Map of located events overlain on tectonic units with algorithmically detected clusters circled blue. Green circles highlight areas of known or suspected mining activity. The Arthur River swarm is labelled and distinguished by its tight group of orange points indicating main shocks of magnitudes M_{La} 4–5

The Arthur River swarm (labelled in Fig. 18 and shown in detail in Fig. 19) began on 5 January 2022 with an M_{La} 4.0 earthquake and still showed significant activity through the end of our catalogue, with an M_{La} 3.5 event on 10 November 2023. Our catalogue observed 32 M_{La} 3+ events and 5 M_{La} 4+ events, of which the largest was an M_{La} 4.8 event on 24 January 2022. The focal mechanisms of the larger events have been associated with thrust faulting with an east–west direction of maximum shortening (Mousavi et al., 2024). In total, our catalogue holds 2901 associated events, nearly all of which are within a 4 km² area (Fig. 19). The events in Figure 19 also do not show any obvious spatial or temporal trends. The lack of any clear surface fault trace due to earthquake activity is consistent with other large-volume, spatially dense swarms in the region, such as the Burakin (Leonard, 2002) and Lake Muir sequences (Clark et al., 2020).

A depth vs time image of the Arthur River swarm is shown in Figure 20 and the frequency distribution showing the number of events per day is given in Figure 21. Earthquake hypocentres are almost exclusively shallower than 4 km, and larger events were deeper. The largest event (M_{La} 4.8) was at 21:24:47 UTC on 22 January 2022, about 19 days after the first two significant events (M_{La} 4.0 at 11:37 UTC on 5 January 2022 and M_{La} 3.78 at 22:50 UTC on 17 January 2022). In the following ~2 years, the swarm mostly continued at a steady number of events per day (i.e. 1 to 12; Fig. 21) with 12 days of high-volume activity (31 or more events per day), typically punctuated by larger M_{La} 3.0+ events. There is a clear drop in low-magnitude events in Figure 20 beginning around 1 November 2022 with the pullout of the ~7 nodes (sites SWNN*, Fig. 19) which may explain the ‘fat tail’ frequency distribution in Figure 21 rather than a logarithmic Omori-like decay.

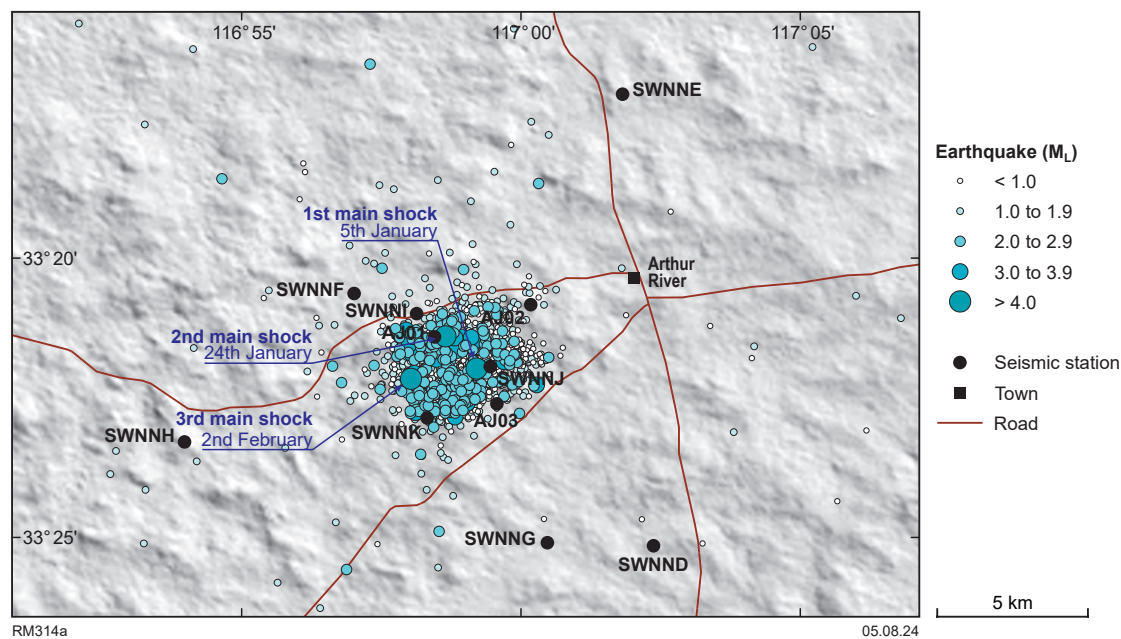


Figure 19. Precision map of Arthur River events

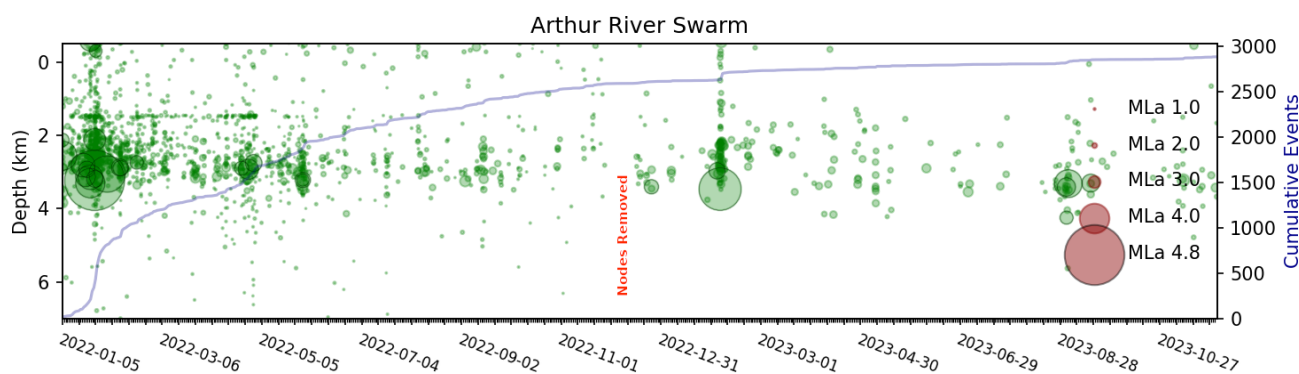


Figure 20. Depth vs time figure of Arthur River events. Scale events are plotted in pink and cumulative events in blue

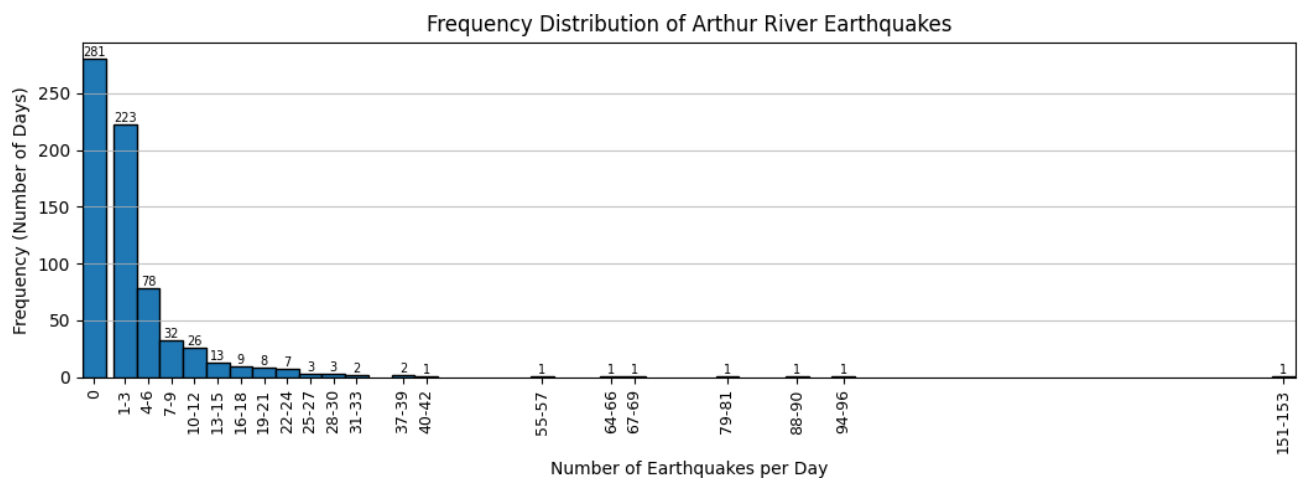


Figure 21. Frequency distribution of Arthur River events. Each bar represents the number of days in which N number of earthquakes were detected

Other notable events in the recording period included the M_{La} 4.8 event at Gnowangerup on 5 January 2023, which was followed by an M_{La} 5.8 event on 5 August 2023. There was also an accompanying swarm to this event; however, it was not as intense or persistent as the Arthur River swarm. This had also been the site of a previous swarm without mainshocks at the end of 2007 (Dent et al., 2010).

Smaller swarm events also are seen in areas such as Beacon, Bencubbin and Mawson. Beacon is an area which often experiences low-level activity as demonstrated by previously recorded swarms in 2009 (Dent, 2009), and 2012–13 (Dent, 2013).

Conclusions

We have applied a machine learning phase picker to new seismic data from 1 September 2020 to 20 December 2023 acquired from the South West Australia Network (2P) and WA Array (WG) experiments, in combination with the AusArray (OA) temporary experiment and pre-existing and permanent AuSIS (S1) and national networks (AU). This process was used to locate over 12 400 earthquakes and mining blasts (~17% of this catalogue) with average horizontal and vertical hypocentre uncertainties of 1.8 and 3.2 km, respectively. We observed that the distribution of these events varies from being spatially independent (37%) or occurring in any of 42 algorithmically defined clusters defined as having 40 or more events within a radius of 0.05 degrees. This work also located ~2900 earthquakes associated with the Arthur River swarm that began on 5 January 2022. Our catalogue's magnitude of completeness is estimated to be M_{La} 2.0 compared with the national catalogue's ~2.75 M_{La} for the same region and time. The dense station coverage provided by the SWAN and WA Array experiments has dramatically improved our understanding of the nature and activity of year-to-year seismicity in Australia's most seismically active region and may enhance our understanding of swarm earthquake behaviour and seismic hazard in the region.

References

- Clark, DJ, Brennand, S, Brenn, G, Garthwaite, MC, Dimech, J, Allen, TI and Standen, S 2020, Surface deformation relating to the 2018 Lake Muir earthquake sequence, southwest Western Australia: new insight into stable continental region earthquakes: *Solid Earth*, v. 11, no. 2, p. 691–717, doi:10.5194/se-11-691-2020.
- Dent, VF 2009, The Beacon, WA earthquake swarm commencing January 2009: Australian Earthquake Engineering Society Conference 2009, Newcastle, NSW, December, 2009, Australian Earthquake Engineering Society.
- Dent, VF 2013, Using the “PSN” seismograph network in southwest Australia to improve earthquake locations in the region: Australian Earthquake Engineering Society Conference, Hobart, Tasmania, 15–17 November, Australian Earthquake Engineering Society.
- Dent, VF, Harris, P and Hardy, D 2010, A new seismograph network in the southwest seismic zone of Western Australia: Australian Earthquake Engineering Society 2010 Conference, Australian Earthquake Engineering Society 2010 Conference, Perth, Australia.
- Gordon, FR and Lewis, JD 1980, The Meckering and Calingiri earthquakes October 1968 and March 1970: Geological Survey of Western Australia, Bulletin 126, 229p.
- Leonard, M 2002, The Burakin WA earthquake sequence Sept 2000 – June 2002: Australian Earthquake Engineering Society Conference 2002, Adelaide, South Australia.
- Leonard, M and Clark, D 2011, A record of stable continental region earthquakes from Western Australia spanning the late Pleistocene: Insights for contemporary seismicity: *Earth and Planetary Science Letters* v. 309, no. 3–4, p. 207–212.
- Lomax, A, Michelini, A, Curtis, A, Meyers, RA and Others 2009, Earthquake location, direct, global-search methods: *Encyclopedia of complexity and systems science*, p. 2449–2473.
- Lomax, A, Virieux, J, Volant, P and Berge-Thierry, C 2000, Probabilistic earthquake location in 3D and layered models, in *Advances in seismic event location*: Springer, pp. 101–134.
- Michelini, A, Cianetti, S, Gaviano, S, Giunchi, C, Jozinović, D and Lauciani, V 2021, INSTANCE – the Italian seismic dataset for machine learning: *Earth System Science Data*, v. 13, no. 12, p. 5509–5544.
- Mousavi, SM, Ellsworth, WL, Zhu, W, Chuang, LY and Beroza, GC 2020, Earthquake transformer—an attentive deep-learning model for simultaneous earthquake detection and phase picking: *Nature Communications*, v. 11, no. 1, p. 1–12.
- Mousavi, S, Pickle, R and Miller MS 2024, Centroid moment tensor (CMT) solutions for earthquakes in southwest Australia, enabled by the SWAN network, in *South West Australia Network (SWAN): passive seismic imaging and hazard analysis compiled by RE Murdie and MS Miller*: Geological Survey of Western Australia, Report 255, p. 30–35.
- Mousavi, SM, Sheng, Y, Zhu, W and Beroza, GC 2019, STanford Earthquake Dataset (STEAD): A global data set of seismic signals for AI: *IEEE Access*, v. 7, p. 179464–179476.
- Murdie, RE, Pickle, R, Yuan, H, Love, D, Dent, V, Miller, MS and Whitney, J 2022, Observations from the 2022 Arthur River, Western Australia, Earthquake Swarm, in *2022 National Conference proceedings*, Mount Macedon, Victoria, 24–25 November 2022, Australian Earthquake Engineering Society.
- Murdie, RE, Yuan, H, O'Donnell, JP, Johnson, SP, Ebrahimi, R and Rashidifard, M 2024, WA Array: A High-Resolution Passive-Source Seismic Survey to Image the West Australian Lithosphere: *Seismological Research Letters*, v. 95, no. 5, p. 3093–3108. doi:10.1785/0220230415.
- Salmon, M, Kennett, BLN and Saygin, E 2012, Australian Seismological Reference Model (AuSREM): Crustal component: *Geophysical Journal International*, v. 92, p. 190–206.
- Standen, S, Denthith, M and Clark, D 2021, A geophysical investigation of the 2018 Lake Muir earthquake sequence: reactivated Precambrian structures controlling modern seismicity: *Australian Journal of Earth Sciences*, v. 68, no. 5, p. 717–730, doi:10.1080/08120099.2021.1848924.
- Vogfjörð, KS and Langston, CA 1987, The Meckering earthquake of 14 October 1968: A possible downward propagating rupture: *Bulletin of the Seismological Society of America*, v. 77, no. 5, p. 1558–1578.

Centroid moment tensor (CMT) solutions for earthquakes in southwest Australia, enabled by the SWAN network

S Mousavi¹, R Pickle¹ and MS Miller¹

1. Research School of Earth Sciences, The Australian National University, Acton ACT 2601

Scientific abstract

Southwest Australia is the most seismically active area in the stable continental region of Australia. The SWAN array, a temporary broadband network consisting of 27 stations, operational from October 2020 to November 2023, detected a significant earthquake swarm, named the Arthur River swarm. This comprised more than 3000 located events as of December 2022. The swarm appears to be ongoing and is the largest example of several clusters of smaller earthquake swarms observed within the SWAN array.

Earthquake swarms are often presumed to originate within brittle fault damage zones, typically characterized by high permeability. Nonetheless, it is not definitively established that all swarm-related seismicity is linked to fluid movements within these zones. To probe the structure of the focal zone of the Arthur River swarm, we estimated the **centroid moment tensors** (CMT) for earthquakes recorded by SWAN with magnitudes in the range M_L 3.7 – 4.7. The CMTs were derived from comprehensive full-waveform modelling, employing a 4D spatiotemporal grid search that allowed for time shifts around the origin time. This inversion process yielded a suite of solutions that delineate the depth and location of the centroid, and the moment tensor of the earthquakes. We have tested a range of frequency bands and concluded that our local Earth model, developed using earthquakes recorded by SWAN, sufficiently simulates seismic waves up to 0.15 Hz. Our analysis reveals that the selected earthquakes exhibit a reverse faulting mechanism at exceptionally shallow depths within the top 5 km. With double-couple (DC) percentages exceeding 80%, these findings underscore that the seismic events are primarily driven by shear moments along planar fault zones.

KEYWORDS: Arthur River swarm, centroid moment tensor, southwest Australia, waveform modelling

Lay abstract

Southwest Australia is the most seismically active area in the stable continental region of Australia. Since October 2020, the ongoing Arthur River swarm has produced over 3000 earthquakes. By analysing the mechanism of these events, we found that most are driven by shear forces. These earthquakes, occurring at shallow depths within the top 5 km, exhibit a reverse faulting mechanism, indicating they are primarily caused by stress and movement along fault planes.

Introduction

Given Australia's intraplate setting, the occurrence of large-magnitude earthquakes is low relative to plate-boundary regions (e.g. Attanayake et al., 2019; Mousavi et al., 2023; Hejrani and Tkalčić, 2019). Nevertheless, these events can still cause significant damage.

Of Australia's nine documented surface rupturing earthquakes, five have occurred within the southwestern Western Australian region (Clark et al., 2020). Notable historical events to have occurred in the region include the 1968 Meckering earthquake (Gordon and Lewis, 1980; Vogfjörð and Langston, 1987; Clark and Edwards, 2018), the 1979 Cadoux earthquake (Lewis et al., 1981; Denham et al., 1987), the 2018 Lake Muir swarm (Clark et al., 2020) and the 2010 Kalgoorlie earthquake (Bathgate et al., 2010; Sippl et al., 2015). These events highlight the region's high levels of earthquake occurrence and the risks they pose to the built environment and vulnerable communities, even in a stable continental setting far from active plate boundaries.

In addition to these significant events, the southwest Australia region has experienced numerous small-magnitude earthquake swarms, such as the Burakin swarm from September 2000 to June 2002 (Leonard, 2002). These swarms, along with significant individual earthquakes, demonstrate the importance of accurate seismic monitoring and data collection. However, seismic hazard assessments in Australia are limited by the sparse coverage of permanent seismic stations (Allen, 2020), such as those in Geoscience Australia's Australian National Seismograph Network (ANSN) (Geoscience Australia, 2021) and the Australian Seismometers in Schools (AuSIS) network (Balfour et al., 2014).

Recent seismic activity, including the Arthur River swarm (Murdie et al., 2022), underscores the ongoing nature of seismicity in southwest Australia. The deployment of the SWAN array has enabled detailed analysis of these events, including the calculation of centroid moment tensor (CMT)

solutions. The increased number and quality of stations in the SWAN array significantly enhance the collection of seismic data (Pickle et al., 2024). These high-quality data facilitate the development of more accurate local velocity models, which are crucial for generating precise CMT solutions. Such detailed insights are essential for accurately understanding the mechanisms of earthquakes in southwest Australia.

Data and method

Figure 22 illustrates the distribution of earthquake epicentres recorded from 1960 to the end of 2022, prior to and during deployment of SWAN array (Miller et al., 2023), specifically highlighting events with M_{La} greater than 2.0. The locations of broadband stations in the SWAN network are marked by blue triangles, and stations from the Australian Seismometers in Schools (S1) and the National Seismograph Network (AU) are shown as yellow and magenta triangles, respectively. The arrow pointing to Events #1 to #4 identifies the 2022 Arthur River swarm zone.

The CMT was calculated for four significant events within the 2022 Arthur River swarm, with magnitudes above M_{La} 3.5 (Pickle et al., 2024):

Event #1: date 5 January 2022, M_{La} 4.0

Event #2: date 22 January 2022, M_{La} 3.7

Event #3: date 24 January 2022, M_{La} 4.7

Event #4: date 1 February 2022, M_{La} 4.3.

An additional event (#5) that occurred outside the Arthur River swarm cluster on 21 August 2022 in the Cadoux region, with a magnitude of M_{La} 4.3, was also analysed.

For the CMT inversion, we used full-waveform data from stations across the SWAN, AU and S1 networks that are located within an epicentral distance of 0.8 to 2.5 degrees from the earthquake epicentres. The raw data from these stations underwent corrections for instrument response and were low-pass filtered and resampled to 10 samples per second. To ensure accuracy, a two-way band pass Butterworth filter covering the frequency range from 0.04 to 0.15 Hz was applied to both the raw and synthetic data. The synthetic seismograms, based on our 1D velocity

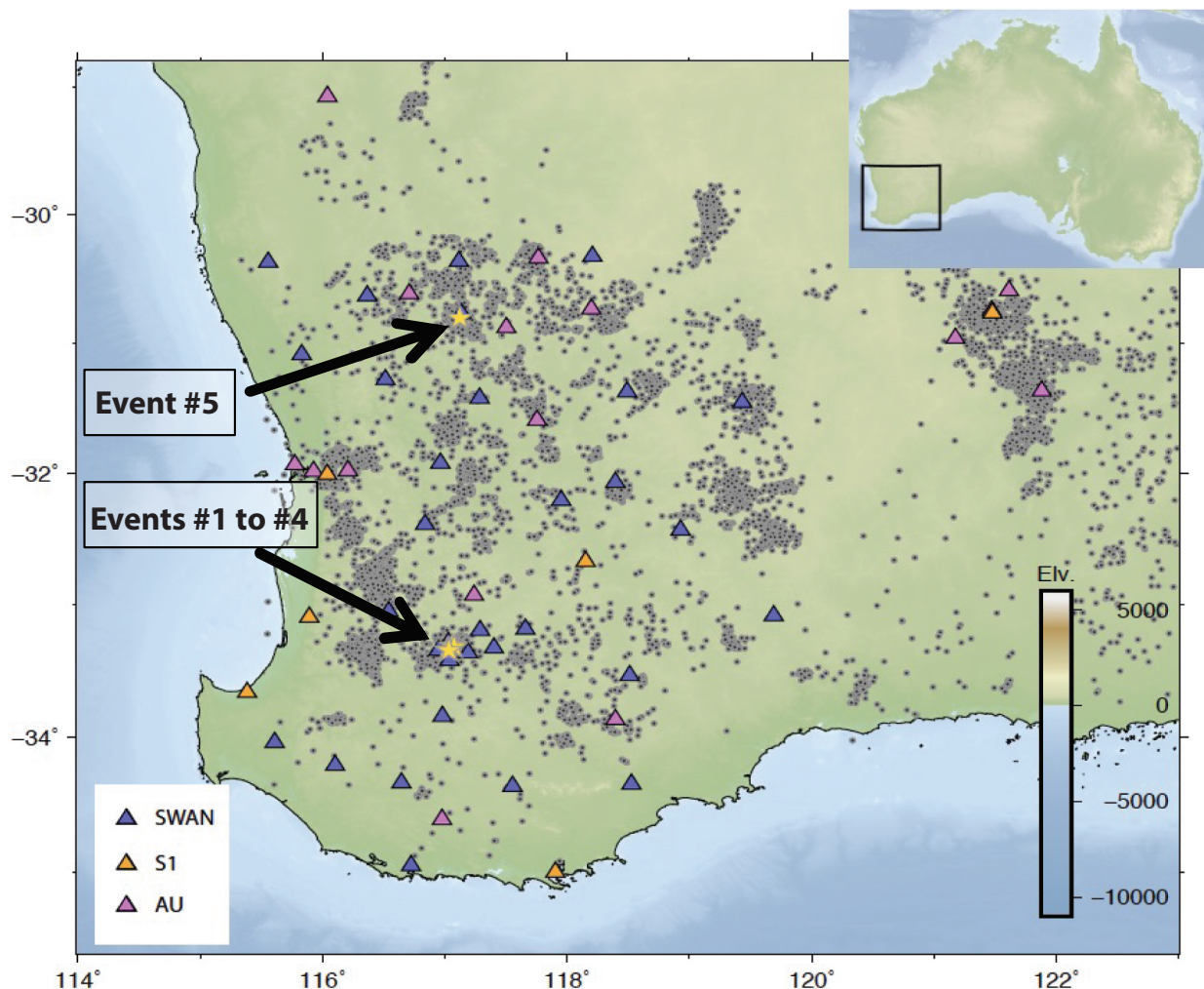


Figure 22. Earthquake epicentres in southwest Australia from 1960 to 2022 (see Pickle et al., 2024), with a focus on events with magnitudes greater than 2.0. Broadband stations are marked by blue triangles for SWAN, yellow for Australian Seismometers in Schools (S1), and magenta for the National Seismograph Network (AU). Events #1 to #4 occurred within the Arthur River swarm area. An additional Event #5 occurred outside this area

model, demonstrated acceptable accuracy within this frequency range, and a total waveform length of 160 s was incorporated into our inversions.

Full-waveform inversion is performed to estimate the CMT solution, which characterizes the earthquake source mechanism. The CMT solution follows the convention by Kikuchi and Kanamori (1991), representing the moment tensor as a linear combination of six independent basic mechanisms. By estimating the coefficients of these mechanisms through a least-squares method using observed and synthetic waveform data, the CMT solution is determined. The best model is selected by finding the optimal centroid location and time shift through a grid search based on the highest fit value.

Results

The inversion was conducted across a range of frequency bands and we concluded that our local Earth model, developed using earthquakes recorded by SWAN, adequately simulates seismic waves up to 0.15 Hz. Through initial assessments, the components of stations where their phase and amplitude could not be fitted with our model were excluded. The 4D grid search for the centroid time and location of Event #1 is visualized in two plots (Fig. 23a,b). The stations selected for waveform modelling are shown in Figure 23c. The fit between the real and synthetic data is colour-contoured in longitude-latitude and depth-time plots, which demonstrate the data's sensitivity to centroid location and timing.

The CMT results of Event #1 are presented along with the waveform fit between real and synthetic data at the optimal point at frequencies of 0.04 – 0.15 Hz (Fig. 24). Within this

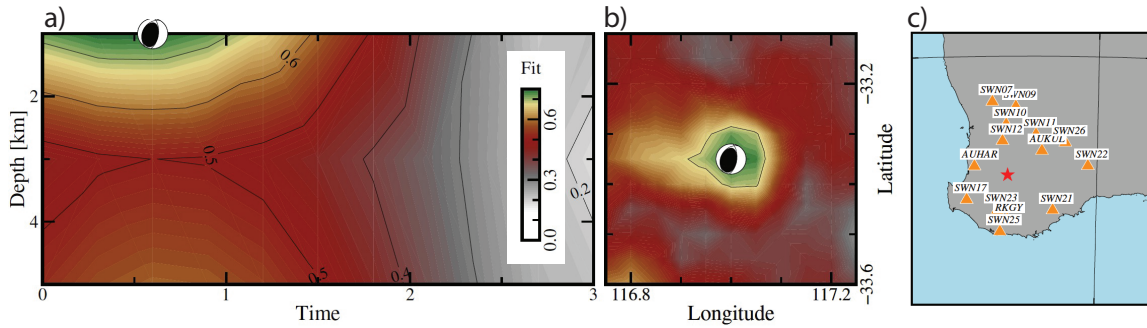


Figure 23. Results of the CMT inversion for Event #1: a) and b) depict two slices from the grid search for centroid time and depth, and for location in latitude and longitude, with the optimum CMT solution. The background colour in these panels represents the fit; c) illustrates the distribution of stations used for the CMT inversion, highlighting the comprehensive coverage that supports the inversion analysis

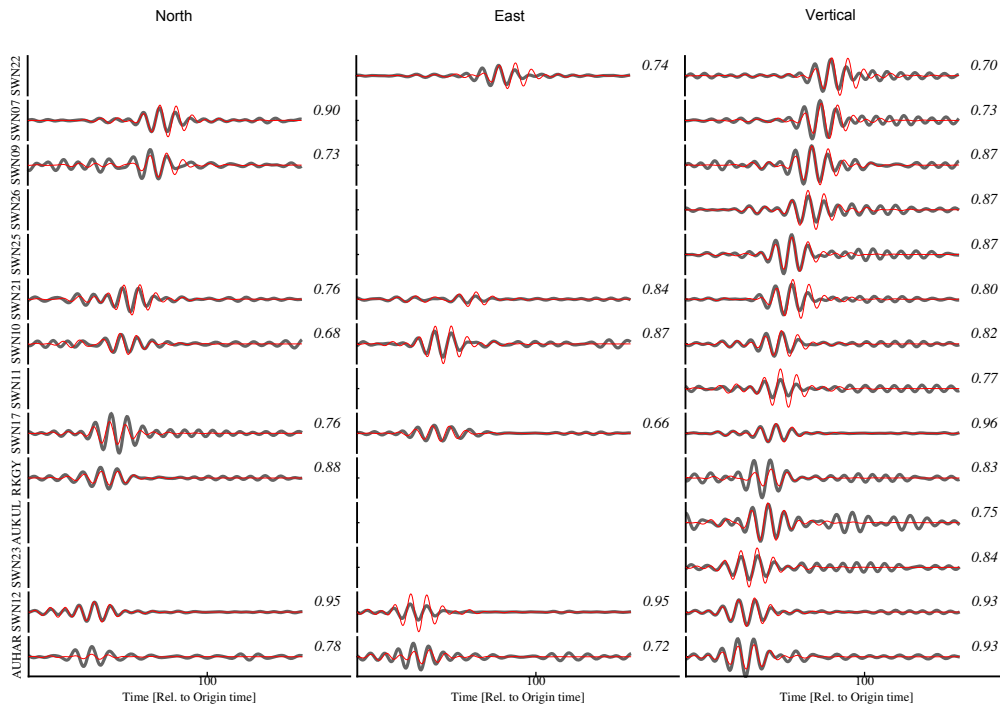


Figure 24. Waveform fits for the optimum CMT solution are presented across three panels: north component on the left, east component in the middle, and vertical component on the right. In each panel, synthetic data are plotted in red and real data in black, showcasing their alignment within the frequency band of 0.04 Hz to 0.15 Hz. Numbers on the right side of each panel indicate the correlation between the real and synthetic data for each component

frequency band, the accuracy of the constraints on the centroid's location, depth and time, provided by the CMT solutions, is notably enhanced (Hejrani and Tkalčić, 2020). The CMT solution indicates that the optimal depth range is around 1 km. The timing of the centroid is observed to be within 0-1 s after the origin time across all analysed events, which is considered a reasonable range given the size of the events and potential errors in determining the exact hypocentre time.

Furthermore, the overall fit between the synthetic and real data for all models is significantly high, with a minimum of 70% (Fig. 24). This high level of fit indicates robustness and precision of our CMT solutions.

The depth, double-couple (DC) percentages and mechanisms for the seismic events are summarized in Figure 25 and Table 3. All five events exhibit high DC percentages (>70%). The events located in the Arthur River swarm area have an optimal depth of 1 km, while Event #5 near Cadoux extends down to 5 km. Figure 26 illustrates the distribution and mechanisms of these events, highlighting their centroid locations and showing that all exhibit a reverse faulting mechanism.

Discussion and conclusion

The deployment of the SWAN network has significantly enhanced regional seismic coverage in southwest Australia, facilitating the study of a range of small-magnitude earthquakes. This research utilized high signal-to-noise waveforms from both permanent and SWAN stations to investigate the centroid moment tensor (CMT) solutions for the four earthquakes from the Arthur River swarm in 2022. These events occurred at very shallow depths; specifically, the analysed Arthur River swarm earthquakes were located at ~1 km depth, which is consistent with observed deformation (Shea et al., 2022). The single event in the north was located at ~5 km depth.

The CMT solutions exhibited mechanisms consistent with previous studies, such as those by Lin et al. (2021), validating the accuracy and reliability of our results. All five events demonstrated a predominant thrust faulting mechanism with strong double-couple components indicative of simple shear dislocation along the faults in the region. The effective application of waveform modelling, facilitated by the local velocity model and the dense seismic network, has not only confirmed these findings but also enabled the calculation

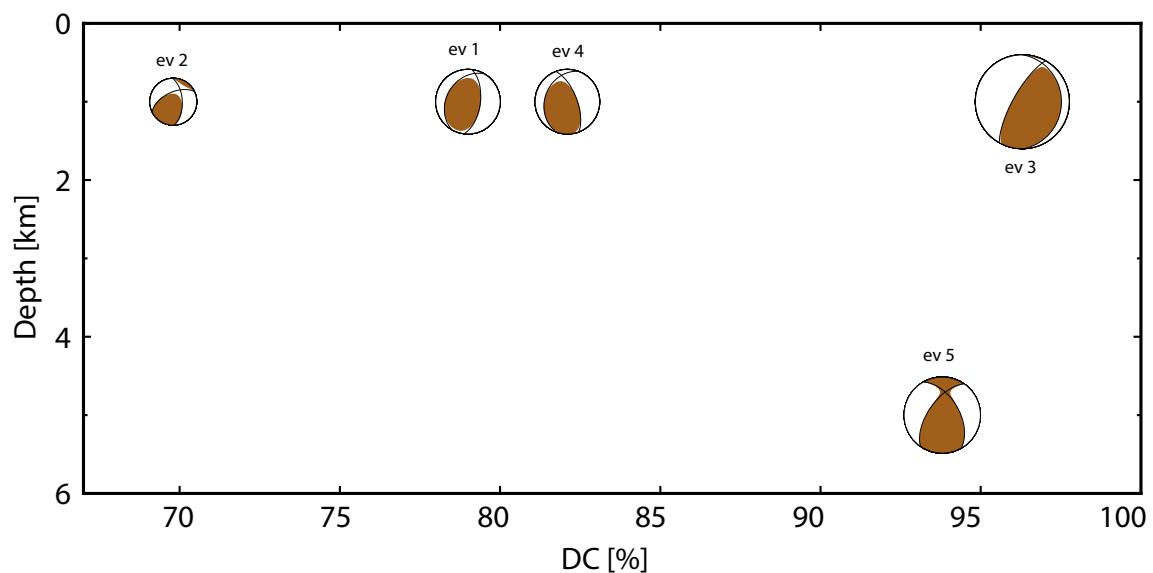


Figure 25. Depth and double-couple (DC) percentages are shown for five events, each depicted with its faulting mechanism

Table 3 Source parameters of the earthquakes in this study

Source	UTC time	M_{La}	Longitude (°)	Latitude (°)	Depth (km)	Strike (°)	Dip (°)	Rake (°)
Event #1	2022-01-05T11:37:02	4.0	117.00	-33.35	1	7.2 210.1	58.5 33.6	77.6 109.4
Event #2	2022-01-22T07:40:49	3.8	117.05	-33.30	1	348.3 240.9	31.8 79.5	-159.7 -59.8
Event #3	2022-01-24T21:24:47	4.8	117.00	-33.30	1	209.5 359.6	74.2 18.0	98.9 61.4
Event #4	2022-02-01T10:41:04	4.1	117.05	-33.30	1	191.8 10.9	66.6 23.4	90.4 89.1
Event #5	2022-08-21T04:37:01	4.3	117.15	-30.85	5	330.1 215.0	53.4 60.2	38.2 136.6

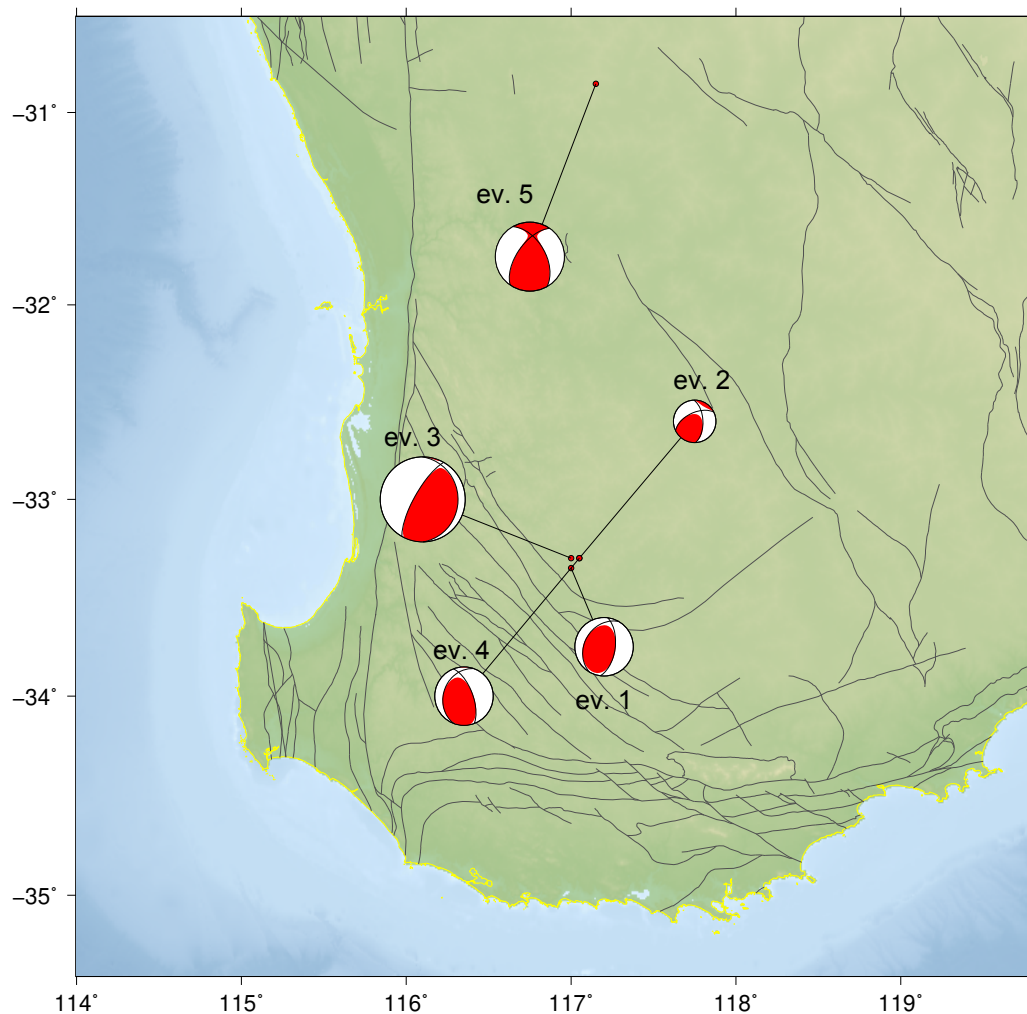


Figure 26. The estimated CMT solutions for earthquakes in southwest Australia overlain on the region's topography. Faults are delineated with thin black lines. All events predominantly display thrust faulting mechanisms with strong double-couple components, indicative of simple shear dislocations along these faults. Faults source: <https://catalogue.data.wa.gov.au/dataset>

of CMT solutions for earthquakes as small as M_l 3.8. This stresses the importance of the SWAN network in enhancing our understanding of seismic mechanisms in southwestern Australia.

References

- Allen, TI, Dhu, T, Cummins, PR and Schneider, JF 2006, Empirical attenuation of ground-motion spectral amplitudes in southwestern Western Australia: *Bulletin of the Seismological Society of America*, v. 96, p. 572–585, doi:10.1785/0120050036.
- Allen, TI 2020, Seismic hazard estimation in stable continental regions: does PSHA meet the needs for modern engineering design in Australia?: *Bulletin of the New Zealand Society for Earthquake Engineering*, v. 53, p. 22–36, doi:10.5459/bnzsee.53.1.22-36.
- Attanayake, J, Sandiford, D, Schleicher, LS, Jones, A, Gibson, G and Sandiford, M 2019, Interacting intraplate fault systems in Australia: The 2012 Thorpdale, Victoria, seismic sequences: *Journal of Geophysical Research*, v. 124, p. 4673–4693, doi:10.1029/2018JB016945.
- Bathgate, J, Glanville, H and Collins, C 2010, The Kalgoorlie earthquake of 20 April 2010 and its aftershock sequence: Australian Earthquake Engineering Society 2010 Conference, Perth, Western Australia, 26–28 November.
- Clark, D and Edwards, M 2018, 50th Anniversary of the 14th October 1968 M_w 6.5 (M_s 6.8) Meckering Earthquake: Australian Earthquake Engineering Society Pre-conference Field Trip, Meckering, 15 November 2018: Geoscience Australia, Record 2018/39, doi:10.11636/Record.2018.039.
- Clark, DJ, Brennand, S, Brenn, G, Garthwaite, MC, Dimech, J, Allen, TI and Standen S 2020, Surface deformation relating to the 2018 Lake Muir earthquake sequence, southwest Western Australia: new insight into stable continental region earthquakes: *Solid Earth*, v. 11, p. 691–717, doi:10.5194/se-11-691-2020.
- Denham, D, Alexander, LG, Everingham, IB, Gregson, PJ, McCaffrey, R and Enever, JR 1987, The 1979 Cadoux earthquake and intraplate stress in Western Australia: *Australian Journal of Earth Sciences*, v. 34, p. 507–521, doi:10.1080/08120098708729411.
- Geoscience Australia 2021, Australian National Seismograph Network Data Collection (Version 2.0), September 2018: Commonwealth of Australia (Geoscience Australia), doi:10.26186/144675.
- Gordon, FR and Lewis, JD 1980, The Meckering and Calingiri earthquakes October 1968 and March 1970: Geological Survey of Western Australia, Report 126, 229p.
- Hejrani, B, Tkalčić, H and Fichtner, A 2017, Centroid moment tensor catalogue using a 3-D continental-scale Earth model: Application to earthquakes in Papua New Guinea and the Solomon Islands: *Journal of Geophysical Research: Solid Earth*, v. 122, no. 10, p. 8570–8595, doi:10.1002/2017JB014230.

- Hejrani, B and Tkalčić, H 2019, The 20 May 2016 Petermann Ranges earthquake: centroid location, magnitude and focal mechanism from full waveform modelling: *Australian Journal of Earth Sciences*, v. 66, no. 1, p. 37–45, doi:10.1080/08120099.2018.1525783.
- Kikuchi, M and Kanamori, H 1991, The use of centroid moment tensor solutions to study earthquake mechanics: Department of Earth Sciences, University of Tokyo, Japan.
- Leonard, M 2002, The Burakin WA earthquake sequence Sept 2000–June 2002: Australian Earthquake Engineering Society 2002 Conference, Adelaide, South Australia, 17–18 October.
- Lewis, JD, Dactwyler, NA, Bunting, JA and Moncrieff, JS 1981, The Cadoux earthquake, 2 June 1979: Geological Survey of Western Australia, Report 11, 133p.
- Lin, X, Yuan, H, Dentith, MC, Murdie, R, Gessner, K and Nayak, A 2021, Improved full waveform moment tensor inversion of cratonic intraplate earthquakes in southwest Australia: *Geophysical Journal International*, v. 227, no. 1, p. 123–145, doi:10.1093/gji/ggab214.
- Miller, MS, Pickle, R, Murdie, R, Yuan, H, Allen, TI, Gessner, K, Kennett, BLN and Whitney, J 2023, Southwest Australia Seismic Network (SWAN): Recording earthquakes in Australia's most active seismic zone: *Seismological Research Letters*, v. 94, p. 999–1011, doi:10.1785/0220220323.
- Mousavi, S, Hejrani, B, Miller, MS and Salmon, M 2023, Hypocenter, fault plane, and rupture characterization of Australian earthquakes: Application to the September 2021 M_w 5.9 Woods Point Earthquake: *Seismological Research Letters*, v. 94, p. 1761–1774, doi:10.1785/0220220348.
- Murdie, R, Yuan, H, Miller, MS, Pickle, R, Salmon, M and Whitney, J 2022, Rapid deployment for earthquake aftershock monitoring in southwest Western Australia – the Arthur River swarm 2022: Preview, v. 217, p. 39–41, doi:10.1080/14432471.2022.2057678.
- Pickle, R, Miller, MS, Murdie, RE and Allen, TI 2024, A detailed earthquake catalogue for southwest Australia 2020–23 using data from the SWAN and WA Array networks, *in* South West Australia Network: passive seismic imaging and hazard analysis *compiled by* RE Murdie and MS Miller: Geological Survey of Western Australia, Report 255, p. 22–29.
- Sippl, C, Kennett, BLN, Tkalčić, H, Spaggiari, CV and Gessner, K 2015, New constraints on the current stress field and seismic velocity structure of the eastern Yilgarn Craton from mechanisms of local earthquakes: *Australian Journal of Earth Sciences*, v. 62, p. 921–931, doi:10.1080/08120099.2015.1114527.
- Shea, HN and Barnhart, WD 2022, The Geodetic Centroid (gCent) Catalog: global earthquake monitoring with satellite imaging geodesy: *Bulletin of the Seismological Society of America*, v. 112, p. 2946–2957, doi:10.1785/0120220072.
- Vogfjörð, KS and Langston, CA 1987, The Meckering earthquake of 14 October 1968: a possible downward propagating rupture: *Bulletin of the Seismological Society of America*, v. 77, p. 1558–1578, doi:10.1785/bssa0770051558, doi:10.1785/BSSA0770051558

3D V_s model of the Earth's crust in southwest Western Australia from ambient noise tomography

P Zhang¹, MS Miller¹, F Magrini¹, R Pickle¹ and H Yuan

1. Research School of Earth Sciences, The Australian National University, Acton ACT 0200

Scientific abstract

This study presents a high-resolution 3D V_s model of the crust and uppermost mantle in the southwest Australia, using ambient noise tomography with continuous data from SWAN (2020–23) and all available stations in the region. The results reveal significant lateral structural variations associated with regional tectonics. The thick Phanerozoic sediments of the Perth Basin characterized by slow materials and the old cratonic basement rocks of the Yilgarn Craton are characterized by fast velocities. Overall, these results are consistent with previous geological and geophysical knowledge but the model's resolution is significantly enhanced. We also identified a new high-velocity anomaly along the western edge of the Yilgarn Craton east of the Darling Fault, offering new insights into the tectonic relationships between the Yilgarn Craton and its surrounding structures.

KEYWORDS: ambient noise tomography, crust structure, Perth Basin, Yilgarn Craton

Lay abstract

This study explores the subsurface structure of the Earth's crust in southwest Australia, focusing on the Yilgarn Craton, one of the oldest parts of the Earth's crust, and its surrounding areas. Using a method called ambient noise tomography, which analyses vibrations recorded by seismic stations, we created a detailed 3D seismic velocity model of the region where new data collected from 2020–23 are included. Our findings show clear structural differences between the Yilgarn Craton and the neighbouring Perth Basin. We also discovered a new feature characterized by seismic high-velocity anomalies along the western edge of the Yilgarn Craton.

Data processing and inversion – ambient noise tomography

Ambient noise surface-wave tomography has become one of the most important tomography tools to image the Earth's crust and uppermost mantle structures since the pioneer work of Shapiro and Campillo (2004) and Shapiro et al. (2005). By cross-correlating continuous ambient noise records between each pair of stations, the surface wave Empirical Green's functions in short to intermedium period bands (<40 to 50 s) can be retrieved. It provides excellent constraints on crustal structures and has been widely applied to local or regional scales (e.g. Yao et al., 2006; Yuan and Bodin, 2018; Zhang and Miller, 2021) and continental-scale imaging studies (e.g. Yang et al., 2007; Lin et al., 2008; Saygin and Kennett, 2012). In this study, we focus on extracting fundamental-mode Rayleigh wave phase velocity dispersions and inverting for 3D isotropic V_s models in the crust and uppermost mantle in southwest Australia.

We used SeisLib, an open-source Python package developed by Magrini et al. (2022) to download and prepare continuous waveform data recorded by the SWAN (2P network, from August 2020 to March 2023), other temporary arrays (6C, 1K, 5C and LM networks), and permanent seismic stations (AU, IU, S1 networks) available in southwest Australia (Fig. 27).

Pre-processing included removing the instrument responses, the mean and linear trend. After this, raw waveforms from 238 stations, using only the vertical component, were down-sampled to 1 Hz and cut into 1-hour-long segments, with 50% overlap between each segment. Next, simultaneous recordings taken from a pair of stations were cross-correlated and stacked over their deployment period. This was done for all possible combination of station pairs, in total over 2000. Figure 28a presents the stacked symmetric cross-correlation functions (CCF) in time domain using all SWAN stations. The Rayleigh wave signals are clearly present within the 2 km/s to 5 km/s window. Each pair of these CCFs in Figure 28a was then measured for phase velocity dispersions up to 0.5 Hz by using the SeisLib package (Fig. 28b). The final dispersion phase velocity measurements were further checked to ensure a minimum interstation path length of 1.5 wavelength to satisfy the far-field assumption (e.g. Luo et al., 2015). A total of 4155 dispersions from 3 s to 39 s (Fig. 28b,c) were retrieved for surface-wave structure imaging.

Following the 'one-step' methodology of Fang et al. (2015), we applied a 3D surface-wave tomography package, DSurfTomo, which directly inverts the measured phase velocity dispersions (Fig. 28b) to produce a 3D V_s model of the regional crust and uppermost mantle. Details of this

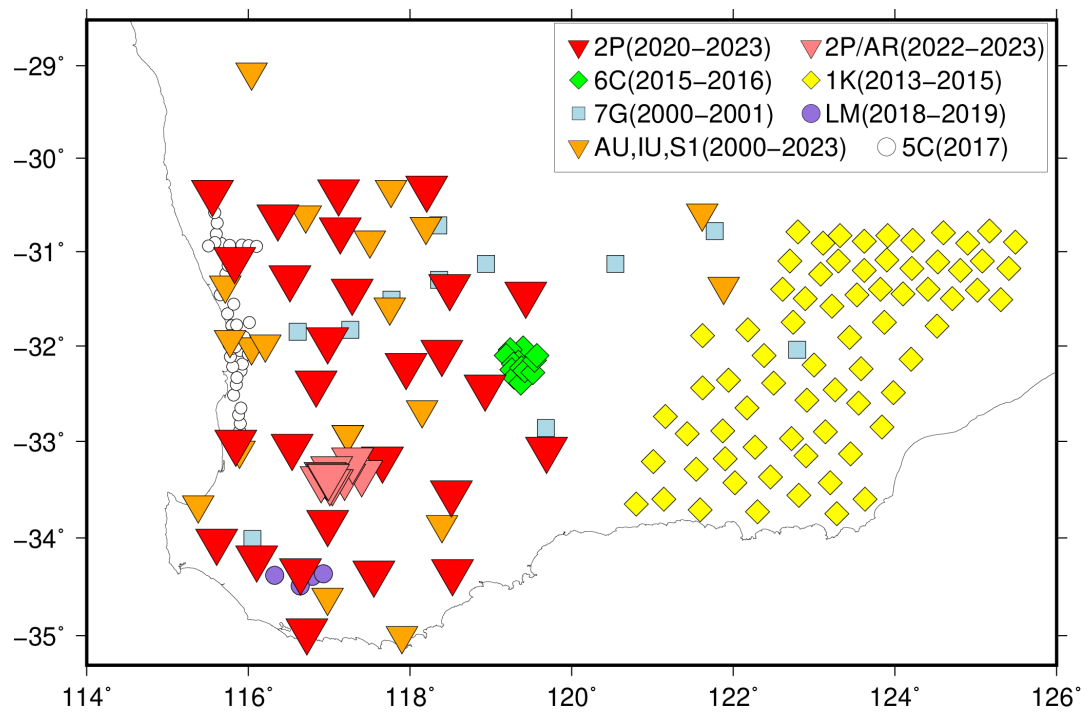


Figure 27. Seismic stations used for ambient noise tomography. Those from the SWAN array are coded as the 2P network (inverted red and pink triangles). Other temporary and permanent deployments available in southwest Australia as diamonds, squares, circles and orange triangles

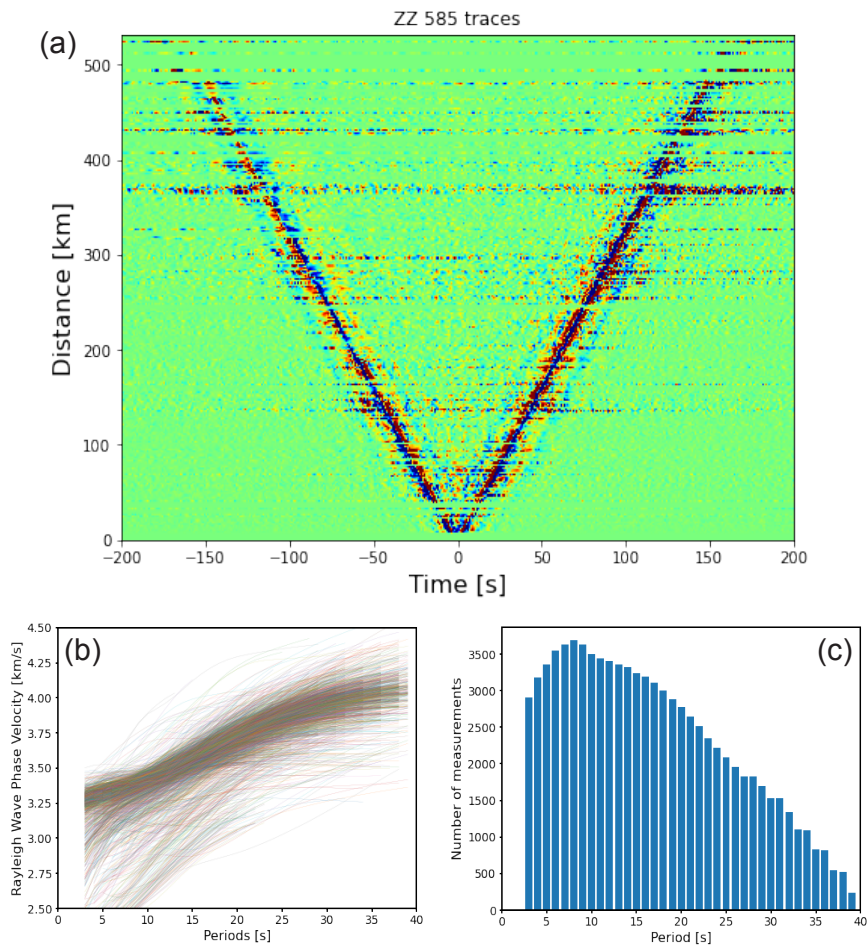


Figure 28. a) Cross-correlation functions in the time domain for the SWAN stations and b) measured fundamental-mode Rayleigh wave phase velocity dispersions c) number of dispersion measurements for each period

technique are described in Fang et al. (2015). Here, we provide specifics on the inversion parameters: starting model for the inversion was the regional average of the AuSREM crust and mantle models (Kennett et al., 2013; Salmon et al., 2013); vertical layer thickness was set to 2 km; lateral grid resolution was $0.25^\circ \times 0.25^\circ$. The final model (Figs. 28 and 29) was determined using an L-curve test and misfit analysis. The phase velocities at the 39 s maximum period provided good depth sensitivity up to 60 km.

Results and discussion – 3D V_s model and preliminary interpretations

The imaged 3D V_s model is presented as horizontal maps at depths of 4 km, 10 km, 16 km and 28 km in Figure 29, and as W–E and N–S trending vertical profiles up to 45 km depth in Figure 30. In comparison with existing continental-scale tomographic models of Australia, which utilized previously

available seismic stations in southwest Australia (e.g. AuSREM crust; Salmon et al., 2013; Saygin and Kennett, 2012; Chen et al., 2023; Magrini et al., 2023), the new ambient noise tomographic model with the additional SWAN array data provides unprecedented resolution in crustal structural images. It shows pronounced lateral structural variations between the Archean Yilgarn Craton and its marginal orogens and basins, and a correlation with terrane structures in the craton interior.

We carried out a checkerboard test to estimate the lateral resolution, using similar parameter settings as used in real-data inversion and checker size of 0.25×0.25 . The test shows that the V_s model in upper 40 km depth can be robustly resolved in regions where data coverage is dense, with a lateral resolution of ~ 60 – 80 km, although varying degrees of smearing are observed (Fig. 31). It is worth pointing out that the topography is not considered in the current inversion; instead, we only interpret the structural pattern at scales that are resolved reasonably well and are not significantly affected by the topographic variations in southwest Australia.

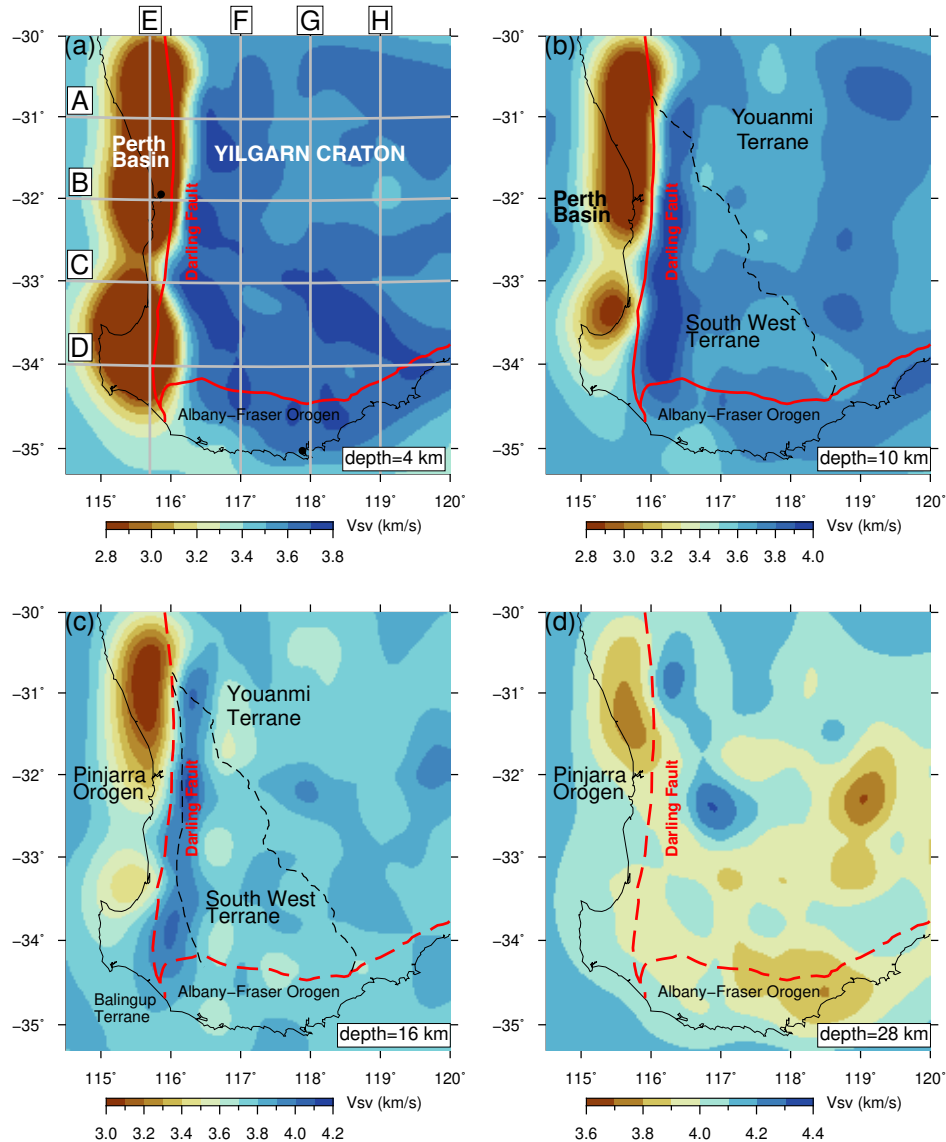


Figure 29. Horizontal slices at depths of 4 km, 10 km, 16 km and 28 km through the 3D V_s model from ambient noise tomography

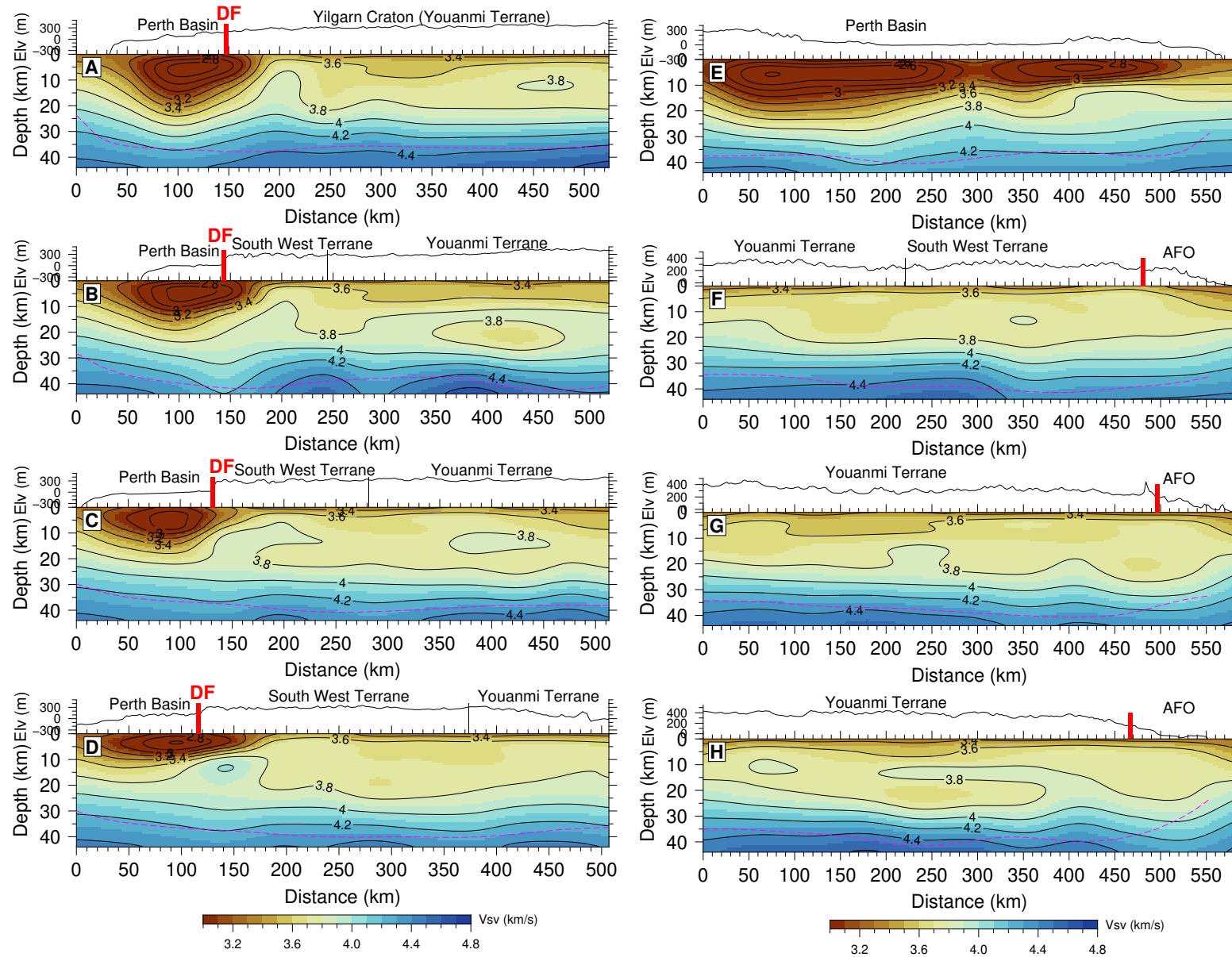


Figure 30. Vertical profiles trending from west to east (profiles A–D, left panel) and from north to south (profiles E–H, right panel) through the 3D V_s model up to 45 km depth from ambient noise tomography. Profile locations are marked in Figure 29. Magenta dashed lines are the Moho depths from the AusMoho model by Kennett et al. (2023)

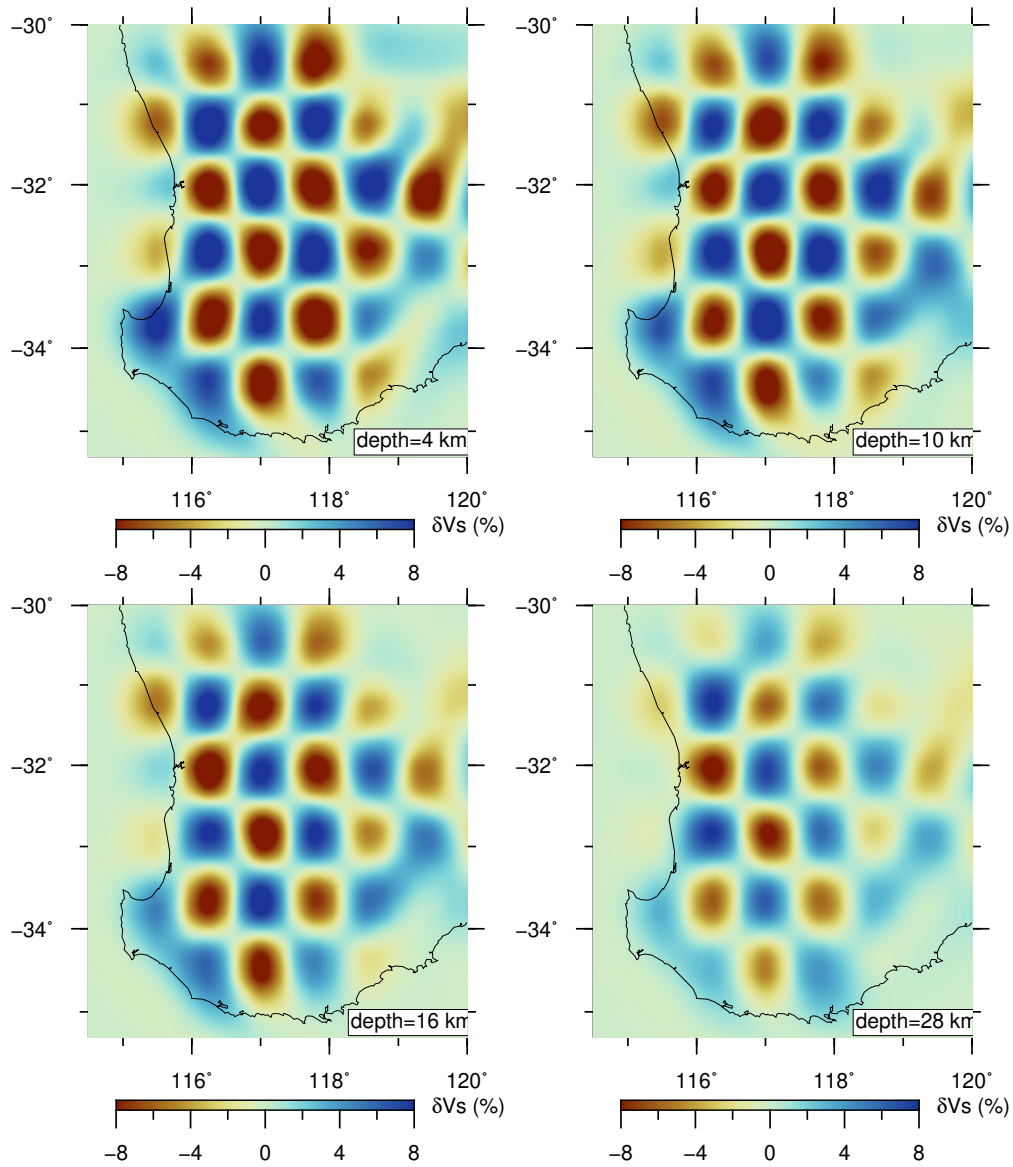


Figure 31. Horizontal slices of the checkerboard resolution test, with a checker size of 0.75 degree by 0.75 degree

At depths of 4 km and 10 km in Figure 29a,b, the Yilgarn Craton in southwest Australia is largely characterized by relatively high-velocity anomalies ($V_s > 3.4$ km/s), which reflects the Archean basement rocks. In contrast, the Perth Basin is dominated by distinct northerly trending low-velocity anomalies ($V_s < 3.0$ km/s) in the shallow to middle crust (<10 to 15 km depth) (Fig. 29a,b). These are interpreted as the thick sedimentary sequences deposited during the Phanerozoic. Our model also shows the basement rocks of the Perth Basin (V_s between 3.2 km/s and 4.0 km/s), which lie to the west of Darling Fault Zone buried beneath the thick sediments (Fig. 29c,d). These basement rocks of the Perth Basin are assumed to be part of the northerly oriented Proterozoic Pinjarra Orogen. In the shallow to middle crust, we also observe a strong velocity contrast that correlates well with the north-trending Darling Fault Zone, which separates the low-velocity ($V_s > 3.0$ km/s) Phanerozoic sediments of Perth Basin in the west from the cratonic crustal ($V_s > 3.0$ km/s) of the Archean Yilgarn Craton to the east (Fig. 29a,b).

At depths of 10 km and 16 km in Fig. 29b,c, we imaged a pronounced northerly oriented high-velocity anomaly ($V_s > 4.0$ km/s) along the western edge of Yilgarn, bounded to the west by the surface extent of Darling Fault and to the south by the Albany–Fraser Orogen. This feature is clearly observed on the maps in Figures 29b and 29c, and at distances between 100–150 km and 200 km along the W–E profiles (profiles A–D) in Figure 30.

The high-velocity anomaly geographically correlates with a narrow north-trending metamorphic belt along the western margin of Yilgarn, bounded to its west by the Darling Fault and to its east by a poorly defined geological boundary (black dashed line in Figure 29c). This belt is termed the Balingup Terrane by Wilde et al. (1996). However, recent geophysical and geological investigations in the southwest corner of the Yilgarn did not find convincing evidence to support the presence of a distinctive terrane in this area (e.g. Quentin de Gromard et al., 2021). The new model in this study has imaged this distinct feature in the middle-to-lower crust at a local scale for the first time.

In comparison to the strong W–E lateral structural variations across the western margin of the Yilgarn, N–S structural variations resolved in our model are less pronounced (e.g. compare the W–E profiles A–D with the N–S profiles F–H in Figure 30). The crustal velocities of the Yilgarn Craton are similar to those of the Albany–Fraser Orogen. This might have been anticipated because the Albany–Fraser Orogen is interpreted as the reworked southeast margin of the Yilgarn Craton (e.g. Spaggiari et al., 2015).

In the craton interior, we observe an overall two-layer crustal structure where the upper-to-middle crustal V_s is about 3.4 – 3.8 km/s and the lower-crustal V_s is in the range 3.8 – 4.2 km/s (Fig. 30). Lateral structural variations within the craton interior in the upper crust are small but there is pronounced middle-to-lower crust structural heterogeneities. The 4.2 km/s velocity contour on the vertical profiles of our tomographic model (Fig. 30) agree well with Moho depths from the Australian Reference Moho model (AusMoho) by Kennett et al. (2023). We, therefore, attribute the structural variations imaged in the lower crust to uppermost mantle (>25 km depth) shown in Figure 30d and profiles F–G in Figure 30 the Moho differences.

Conclusions

We present a new high-resolution 3D V_s model for the crust and uppermost mantle of the southwest Yilgarn Craton and its margins based on ambient noise tomography using data recorded by the SWAN (2020–23) array and other available stations in SW Australia. The model reveals pronounced lateral structural variations across the region, from the Perth Basin in west to the southwest Yilgarn in east. It highlights the thick Phanerozoic sediments of the Perth Basin and its basement rocks, which are part of the Proterozoic Pinjarra Orogen, along the western margin of the Yilgarn Craton. The model also reveals a newly imaged northerly oriented high-velocity anomaly along the western edge of the Yilgarn Craton, bounded by the Darling Fault. The north-trending velocity contrast between Perth Basin and Yilgarn Craton is strong and correlates well with Darling Fault. These structures are overall consistent with previous knowledge from geology and geophysics but never imaged in such high resolution before. The north-oriented high-velocity anomaly imaged in the middle-to-lower crust along the western edge of Yilgarn also calls for a new understanding of the western margin of the Yilgarn Craton and its geometric and tectonic relationships with its bounding orogen and basins, and the terranes of its interior.

References

- Chen, Y, Saygin, E, Kennett, B, Qashqai, MT, Hauser, J, Lumley, D and Sandiford, M 2023, Next-generation seismic model of the Australian crust from synchronous and asynchronous ambient noise imaging: *Nature Communications*, v. 14, no. 1, p. 1192.
- Fang, H, Yao, H, Zhang, H, Huang, YC and van der Hilst, RD 2015, Direct inversion of surface wave dispersion for three-dimensional shallow crustal structure based on ray tracing: methodology and application: *Geophysical Journal International*, v. 201, no. 3, p. 1251–1263.
- Kennett, BL, Gorbato, A, Yuan, H, Agrawal, S, Murdie, R, Doublier, MP, Eakin, CM, Miller, MS, Zhao, L, Czarnota, K, O'Donnell, JP, Dentith, M, and Gessner, K 2023, Refining the Moho across the Australian continent: *Geophysical Journal International*, v. 233, no. 3, p. 1863–1877.
- Kennett, BL, Fichtner, A, Fishwick, S and Yoshizawa, K 2013, Australian seismological reference model (AuSREM): mantle component: *Geophysical Journal International*, v. 192, no. 2, p. 871–887.
- Lin, FC, Moschetti, MP and Ritzwoller, MH 2008, Surface wave tomography of the western United States from ambient seismic noise: Rayleigh and Love wave phase velocity maps: *Geophysical Journal International*, v. 173, no. 1, p. 281–298.
- Luo, Y, Yang, Y, Xu, Y, Xu, H, Zhao, K and Wang, K 2015, On the limitations of inter-station distances in ambient noise tomography: *Geophysical Journal International*, v. 201, no. 2, p. 652–661.
- Magrini, F, Lauro, S, Kästle, E, Boschi, L 2022, Surface-wave tomography using SeisLib: a Python package for multiscale seismic imaging: *Geophysical Journal International*, v. 231, no. 2, p. 1011–1030.
- Quentin de Gromard, R, Ivanic, TJ and Zibra, I 2021, Pre-Mesozoic interpreted bedrock geology of the southwest Yilgarn, 2021: Accelerated Geoscience Program extended abstracts: Geological Survey of Western Australia, Record 2021/4, p. 122–144.
- Salmon, M, Kennett, BLN and Saygin, E 2013, Australian seismological reference model (AuSREM): crustal component: *Geophysical Journal International*, v. 192, no. 1, p. 190–206.
- Saygin, E and Kennett, BLN 2012, Crustal structure of Australia from ambient seismic noise tomography: *Journal of Geophysical Research: Solid Earth*, v. 117(B1).
- Spaggiari, CV, Kirkland CL, Smithies RH, Wingate MTD, and Belousova, EA 2015, Transformation of an Archean craton margin during Proterozoic basin formation and magmatism: The Albany–Fraser Orogen, Western Australia: *Precambrian Research*, v. 266, p. 440–466.
- Shapiro, NM and Campillo, M 2004, Emergence of broadband Rayleigh waves from correlations of the ambient seismic noise: *Geophysical Research Letters*, v. 31, no. 7.
- Shapiro, NM, Campillo, M, Stehly, L and Ritzwoller, MH 2005, High-resolution surface-wave tomography from ambient seismic noise: *Science*, v. 307, no. 5715, p. 1615–1618.
- Wilde, SA, Middleton, MF and Evans, BJ 1996, Terrane accretion in the southwestern Yilgarn Craton: evidence from a deep seismic crustal profile: *Precambrian Research*, v. 78, no. 1–3, p. 179–196.
- Yao, H, van der Hilst, RD and De Hoop, MV 2006, Surface-wave array tomography in SE Tibet from ambient seismic noise and two-station analysis – I. Phase velocity maps: *Geophysical Journal International*, v. 166, no. 2, p. 732–744.
- Yang, Y, Ritzwoller, MH, Levshin, AL and Shapiro, NM 2007, Ambient noise Rayleigh wave tomography across Europe: *Geophysical Journal International*, v. 168, no. 1, p. 259–274.
- Yuan, H and Bodin, T 2018, A probabilistic shear wave velocity model of the crust in the central West Australian craton constrained by transdimensional inversion of ambient noise dispersion: *Tectonics*, v. 37, no. 7, p. 1994–2012.
- Zhang, P and Miller, MS 2021, Seismic imaging of the subducted Australian continental margin beneath Timor and the Banda Arc collision zone: *Geophysical Research Letters*, v. 48, no. 4, e2020GL089632.

Imaging the lithospheric mantle of southwest Western Australia using finite-frequency P-wave tomographic inversion of the SWAN dataset

R Zhao^{1,2}, X Xu³, L Zhao¹, P Zhang⁴, R Pickle⁴ and H Yuan

1. State Key Laboratory of Lithospheric and Environmental Coevolution, Institute of Geology and Geophysics, Chinese Academy of Sciences, Beijing 100029, China
2. College of Earth and Planetary Sciences, University of Chinese Academy of Sciences, Beijing 100049, China
3. Tsinghua University, Department of Mathematical Sciences, Beijing 100084, China
4. Research School of Earth Sciences, The Australian National University, Acton ACT 0200

Scientific abstract

The Yilgarn Craton was formed by the Neoproterozoic amalgamation of the Youanmi, Narryer and South West Terranes, and the Eastern Goldfields Superterrane. There is not yet a consensus about the geodynamic setting in which this cratonization occurred. One theory suggests this amalgamation process mirrored modern subduction and accretion, resulting in numerous north-northwesterly trending sutures. Another theory posits that the Eastern Goldfields Superterrane developed as a rift within the Youanmi Terrane basement. This study, part of the South West Seismic Network (SWAN) project, focuses on the lithospheric structure of the southwest Yilgarn Craton. Recognizing that shallow geological structures are influenced by deeper processes, we utilize teleseismic body-wave tomography to investigate the craton's deep structures. By developing a P-wave velocity model of the upper mantle, we establish connections between deep structures and shallow tectonics to elucidate the craton's evolutionary mechanisms. Our findings aim to provide robust constraints on the craton's evolution and offer significant insights into the region's mineralization processes.

KEYWORDS: cratonic lithosphere, finite-frequency tomography, P-wave velocity structure, Yilgarn Craton

Lay abstract

The Yilgarn Craton is not only one of the largest existing Archean crustal blocks, it is also one of the most mineral-rich regions in the world. Research in this area helps us understand the origin of continents and provides valuable guidance for future mineral exploration. Our study, using seismic methods, has obtained the deep velocity structure of southwestern Australia, revealing the complex internal structure of the Yilgarn Craton, which is significant for understanding the region's evolution over geological time scales. These data allow us to better explain the relationship between deep structures and shallow tectonics, thus guiding future exploration and development. Overall, studying the Yilgarn Craton not only enriches our geological knowledge but also offers significant economic potential, providing important reference value for global mineral resource management and development.

Introduction

The Yilgarn Craton, the largest tectonic unit in Western Australia and one of the oldest cratons globally, covers about one-third of the state's area. It is also among the most mineral resource-rich regions worldwide, offering significant potential for scientific research and economic development. Studying the lithospheric evolution of the Yilgarn Craton provides essential insights into new mineral deposits and opens new avenues for future exploration (Griffin et al., 2004; Betts et al., 2002).

Previous research indicates that the Yilgarn Craton contains abundant high-Ca granites, characteristic of high-pressure melt sources, possibly within thickened mafic crust or from melting subducted oceanic crust. This corresponds

to two main hypotheses regarding the craton's origin: 1) the subduction hypothesis, which suggests early plate amalgamation driven by subduction and accretion, resulting in a series of north-northwesterly trending sutures in the eastern craton (Wilde et al., 1996; Czarnota et al., 2010); 2) the mantle plume hypothesis, which posits that the craton was formed by lateral spreading of melts generated by mantle plume upwelling (Smithies et al., 2005; Van Kranendonk et al., 2007; Mole et al., 2014).

To help differentiate between these mechanisms, a comprehensive understanding of the region's geological structure, particularly its deep structure, is essential. However, the lithospheric structure has remained largely

unconstrained due to limited data coverage. The recent recognition of the region's development prospects has led to an increased deployment of seismic stations. The successful execution of the South West Australia Network (SWAN) passive seismic project has now made it possible to develop the region's first upper-mantle body-wave tomographic model.

Our study leverages data from the SWAN and permanent stations in this region. Using the finite-frequency body-wave tomographic method, we have imaged deep velocity structures in southwestern Australia, providing direct observations of the regional lithosphere which may have archived the craton's deep evolution and shallow geological activities. Our findings provide new insights into the lithospheric architecture and have the potential to enhance understanding of the tectonic processes shaping the Yilgarn Craton and its mineral deposits (Sheppard et al., 2012; Kennett et al., 2013).

Data and method

Finite-frequency body-wave tomography is a powerful tool in seismological research for mapping the Earth's internal structure with high resolution. By analysing the travel times and amplitudes of body waves (P-waves and S-waves)

as they pass through the Earth's interior, this technique accounts for finite-frequency effects; for example, wavefront healing and scattering effects (Dahlen et al., 2000; Montelli et al., 2004), and provides accurate images of subsurface features (Dahlen et al., 2000). This method enhances our understanding of the composition, temperature and dynamics of the mantle and core, significantly contributing to our knowledge of tectonic processes, mantle convection and the overall evolution of the Earth's interior (Trampert and van der Hilst, 2005; Boschi et al., 2006). The method has been widely used to achieve high-resolution images of the Earth's interior.

In this study, we applied a package of finite-frequency body-wave tomography inversion code, which has been employed in several regional and local scale tomographic studies (e.g. Zhao et al., 2016; Xu et al., 2018). The distribution of stations used in the study is shown in Figure 32; it comprises 64 stations – 38 temporary and 26 permanent. The distribution of teleseismic events recorded by these stations covers a wide range of back-azimuths, though fewer events occurred southwest of the array (Fig. 33).

In the finite-frequency approach, we selected three frequency bands for picking travel times. Table 4 details the number of events and raypaths used. Considering that the picked seismic events show uneven distribution characteristics, we need to do some processing to reduce

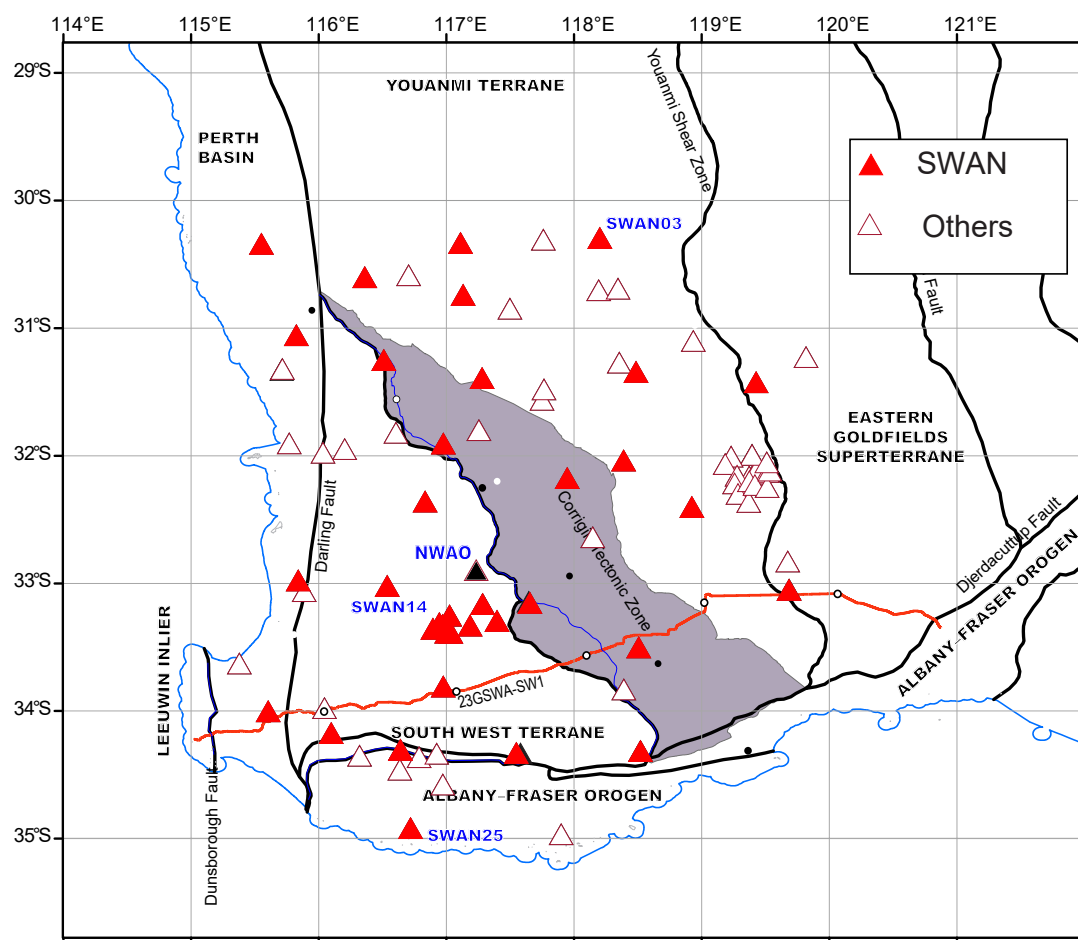


Figure 32. Region of southwest Western Australia covered by this project and distribution of seismic stations. Solid red triangles represent the temporary stations of SWAN, and hollow red triangles represent permanent and other stations

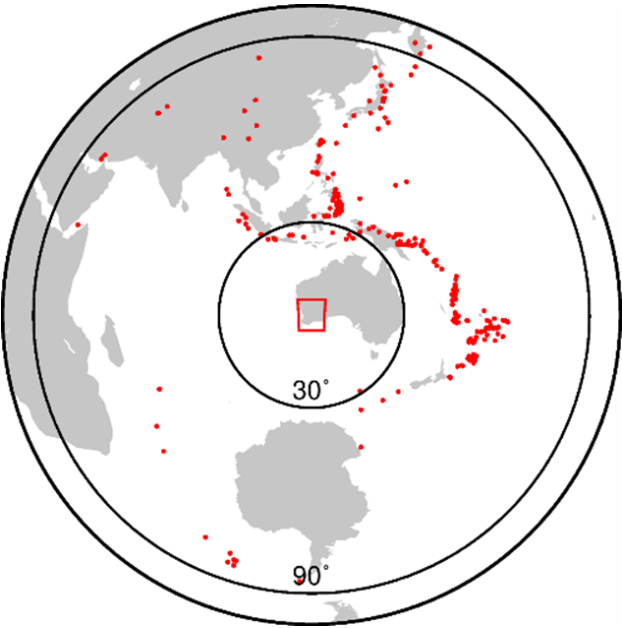


Figure 33. Distribution of teleseismic events. The epicentre distance of most events is between 30° and 90°, while the events with high signal-to-noise epicentre distance <30° are picked up to make the data as much as possible.

Table 4 Frequency bands used for picking seismic-wave travel times, and the number of events and rays picked up in those different frequency bands

Frequency bands	0.02 – 0.3 Hz	0.1 – 0.8 Hz	0.8 – 2.0 Hz
Number of events	147	267	295
Number of rays	4254	7369	6889

the influence of the uneven distribution. With the study area as the centre, the seismic events in the first quadrant are densely distributed and large in number, while the other quadrants are relatively sparse and small in number. This uneven distribution can cause a ‘smearing effect’. A summary ray method can improve this situation to some extent (Robertson and Woodhouse, 1995; Yuan and Dueker, 2005). The basic principle of this method is to merge rays with similar paths. We took each station as a separate dataset, divided all events received by the station into grids according to the back azimuth and ray parameters, combined the rays in each grid, and the combined residual was the average of all events in the grid. After processing all station sets, new travel-time residual data was formed for inversion. This approach can mitigate the effects of dense event distribution areas, resulting in a better model.

After picking the travel-time residuals, crustal corrections were applied to account for the large variation in crustal structure across the region (Fig. 34; Yuan et al., 2024; Zhang et al., 2024). Since teleseismic rays enter the crust at nearly vertical incidence angles, they provide limited resolution of crustal structure due to the reduction in the number of crossing paths that are crucial for tomographic resolution. This lack of constraint on the crustal velocity structure has the potential to introduce artifacts into the tomographic model. Therefore, we corrected the travel-time residuals by calculating the travel-time residuals in crust through the

crustal V_p model, which is upscaled from the SWAN crustal V_s and the V_p/V_s ratio models (Fig. 35; Yuan et al., 2024; Zhang et al., 2024). The calculated travel-time residuals in crust were then subtracted from the total travel-time residuals, thus isolating the travel times due to subcrustal velocity anomalies. It is these travel-time residuals that we tomographically invert for upper-mantle 3D P-wave velocity structure.

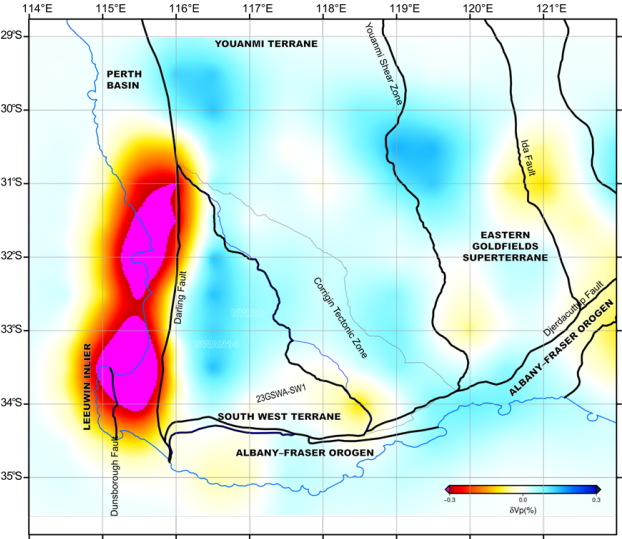


Figure 34. Average crustal P-wave velocity model. Contrasts in crustal velocity across southwest Western Australia. Red represents relative low speed, blue represents relative high speed

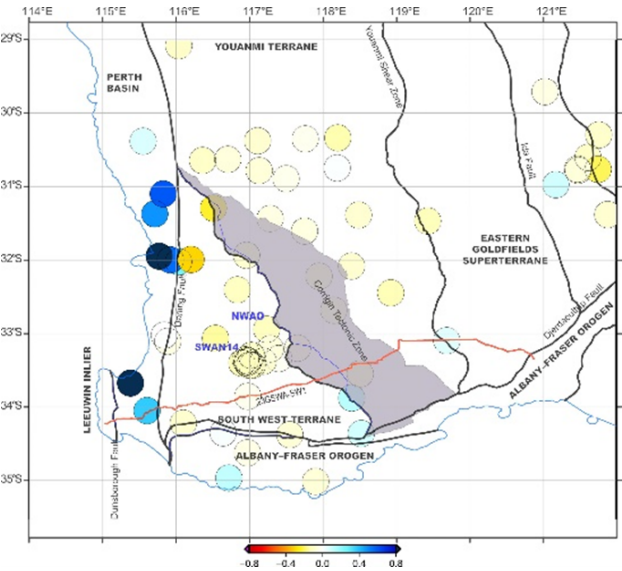


Figure 35. Average crustal correction for stations. It is also the average relative crustal travel-time residual for stations. Yellow and red represent early arrivals, light and dark blue represent delayed arrivals

We parameterized the model space into a grid of $32 \times 32 \times 32$ cells, with each cell measuring approximately $0.25 \times 0.25 \times 25$ km, and selected and applied regularization on the basis of a trade-off between data fitting and model geological plausibility (Fig. 36). The residual distribution in difference between observed and computed travel times has significantly improved after inversion compared to before inversion (Fig. 37).

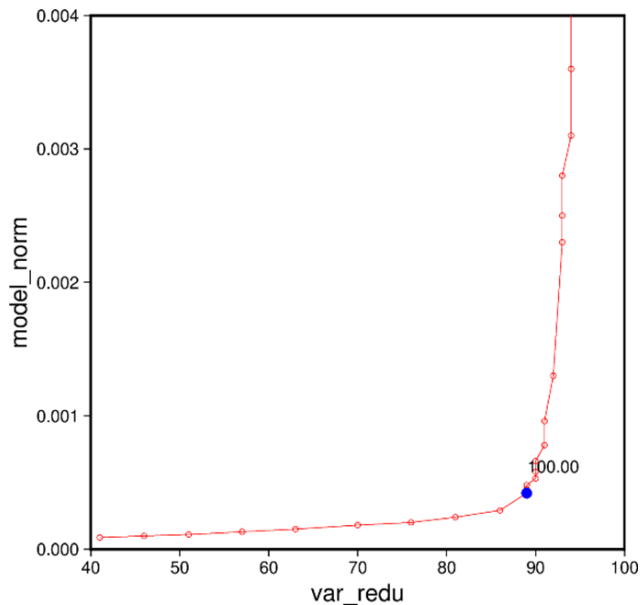


Figure 36. L-curve for selected regularization factors. The L-curve between model norm and variance reduction demonstrates the trade-off between model complexity (model norm) and data fit (var_redu), where more complex (rough) models can fit the data better but may overfit, while simpler (smoother) models offer less precise fits but are more robust against overfitting. An optimal model is usually picked at the 'elbow' of the L-curve

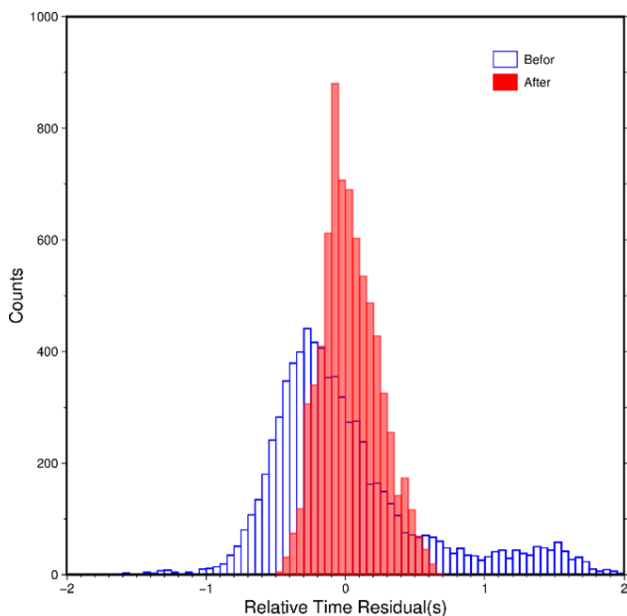


Figure 37. Histograms of relative travel-time residuals. Blue shows the original data and red indicates synthetic relative travel-time residuals from the final tomographic model

P-wave model

Several selected depth slices are shown in Figure 38. Three depth cross-sections AA', BB' and CC' are presented in Figure 39.

Discussion and conclusions

The proposed model for Archean terrane accretion in the southwest Yilgarn Craton (Wilde et al., 1996; Czarnota et al., 2010) suggests a north-northwesterly striking structural fabric in this region. However, Smithies et al. (2023), using dense geochemical datasets, revealed a primary northeast to east-northeasterly trending lithospheric architecture, which challenges the terrane accretion model. This structural inconsistency is compatible with the idea that the craton basement may be segmented into compositionally discrete blocks, possibly due to plume-related accretion (e.g. Mole et al., 2019). Seismic velocity variations can be used as a proxy to evaluate the regional lithospheric architecture and provide constraints on these models (Figs 40, 41).

Several key features can be inferred.

1. Positive velocity variations are observed in the cratonic areas bounded by the Darling Fault to the west and the Albany–Fraser Orogen to the south. This is consistent with the expected fast velocities of cratonic lithospheric roots, indicating the presence of pristine lithosphere.
2. Most of the South West Terrane exhibits negative velocity variations that are significantly slower than those of the craton interior, suggesting the presence of a distinct lithospheric block.
3. However, the pattern of positive velocity variations within the cratonic lithosphere is non-uniform, with small-scale negative velocity variations interspersed throughout.
4. No systematic northwest-trending structure can be inferred in the Corrigin Tectonic Zone and the Youanmi Terrane farther east; nor is any significant northeast-trending pattern recognized.

Combining depth slices, several additional features can be inferred.

5. The lithospheric root within the craton may extend to a depth of 200 km (Fig. 38).
6. Beneath the lithosphere, both negative and positive velocity variations are present, showing no obvious correlation with surface geology.

Overall, the SWAN dataset offers valuable travel-time residual data for understanding the lithospheric structure in southwestern Yilgarn. However, due to the large station spacing (>100 km) and limited spatial coverage, the current dataset lacks the spatial resolution needed to fully address the debate between terrane accretion and vertical plume accretion tectonics, although it does suggest a generally non-uniform craton interior. Higher-resolution data, expected from the ongoing 10-year WA Array seismic campaign (Murdie et al., 2024), should provide more detailed structural insights.

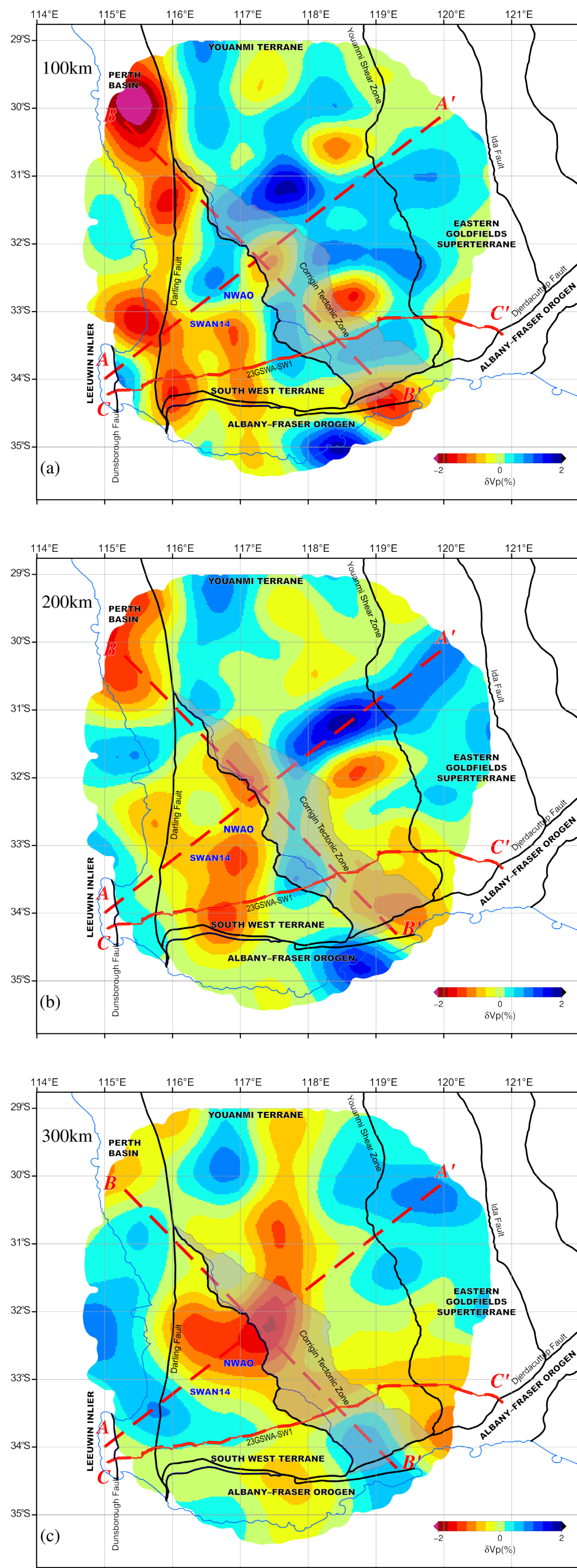


Figure 38. P-wave tomographic model slices at different depths. a) P-wave tomographic models at 100 km in the lithosphere; b) P-wave velocity variations at 200 km near the bottom of the lithosphere; c) P-wave velocity variations at 300 km in the asthenosphere. Colours show velocity variations. Lines AA', BB' and CC' are the locations of depth cross-sections presented in Figure 39

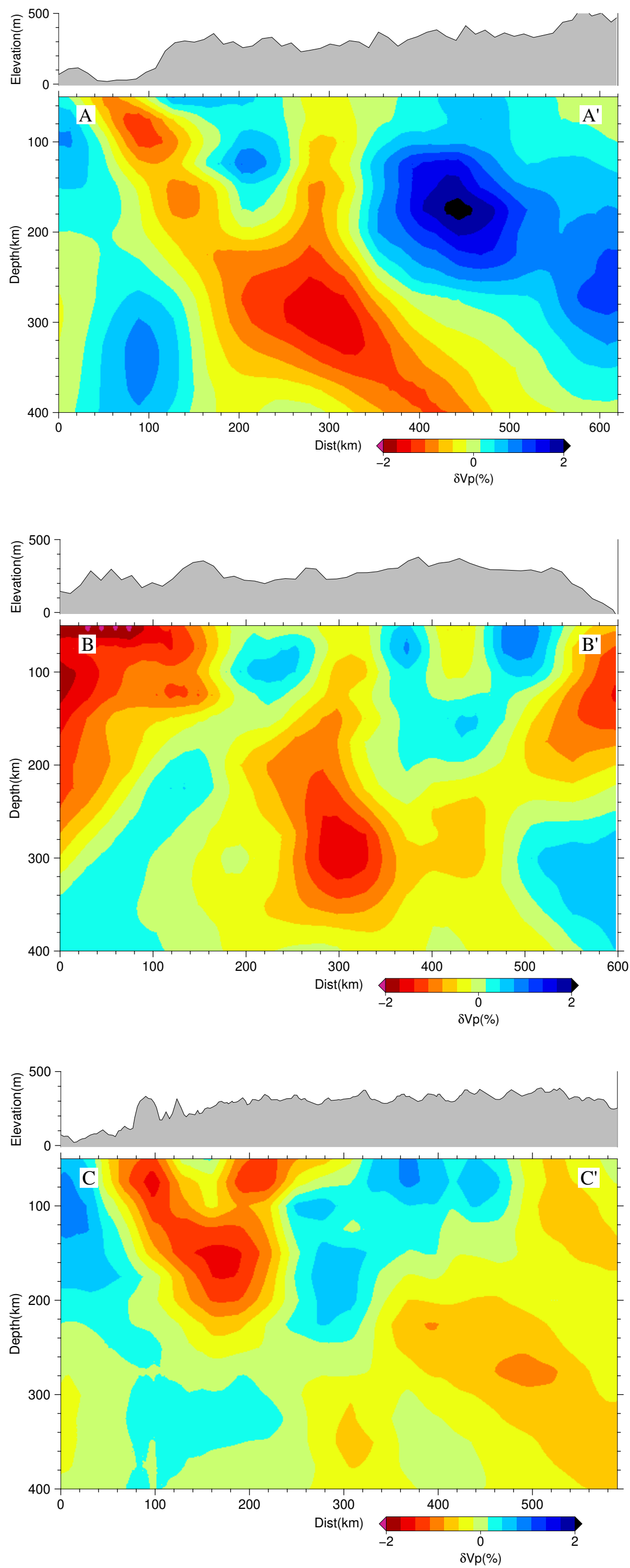


Figure 39. P-wave velocity variation cross-sections along profiles A-A', B-B' and C-C'. Locations of the profiles are shown in Figure 38

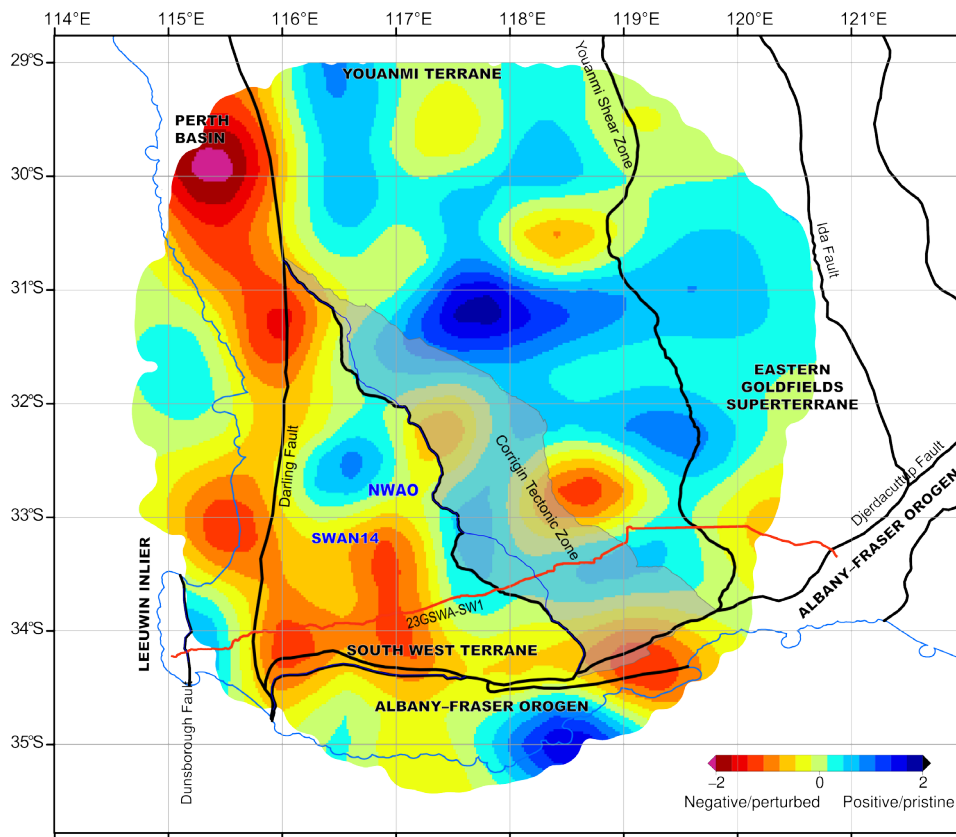


Figure 40. P-wave velocity variations averaged from 70 to 150 km depths. This gives an indication of lithospheric architecture of the southwest Yilgarn Craton

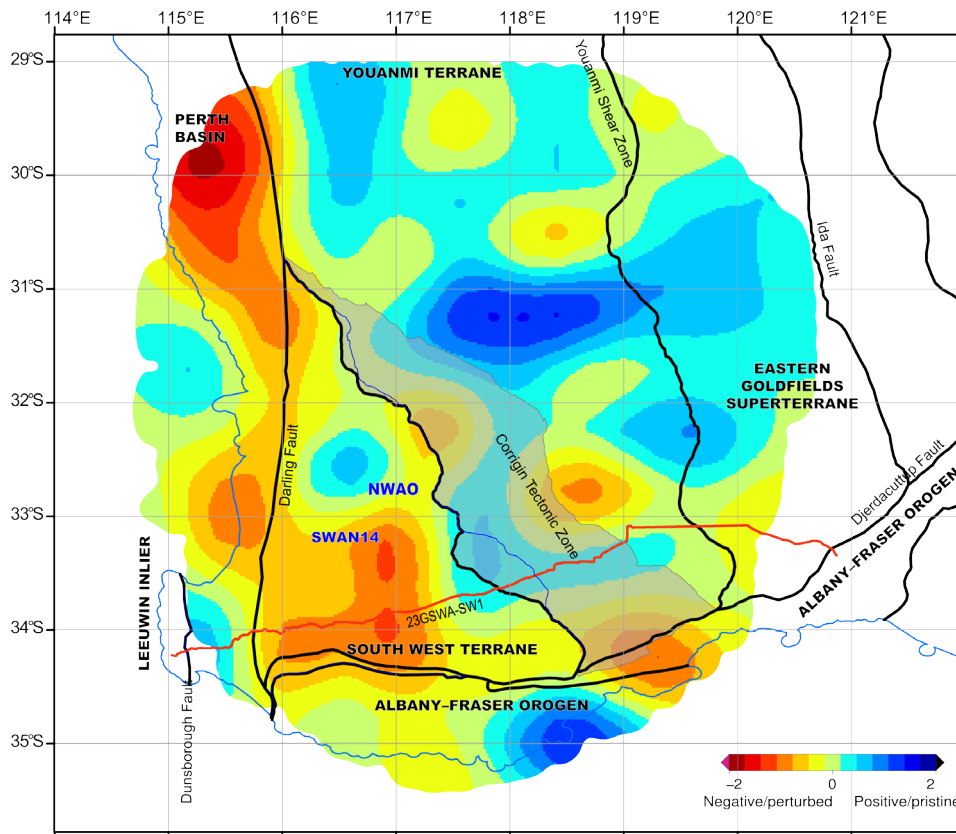


Figure 41. P-wave velocity variations averaged from 50 to 200 km depths. This gives an indication of lithospheric architecture of the southwest Yilgarn Craton

References

- Betts, PG, Giles, D and Lister, GS 2003, Tectonic environment of shale-hosted massive sulfide Pb-Zn-Ag deposits of Proterozoic northeastern Australia: *Economic Geology*, v. 98, no. 3, p. 557–576.
- Boschi, L, Piersanti, A and Spada, G 2006, Global sea-level rise, Antarctic ice mass loss and glacial isostatic adjustment: *Physics of the Earth and Planetary Interiors*, v. 154, no. 1, p. 232–246.
- Czarnota, K, Champion, DC, Goscombe, B, Blewett, RS, Cassidy, KF, Henson, PA and Groenewald, PB 2010, Geodynamics of the eastern Yilgarn Craton: *Precambrian Research*, v. 183, no. 2, p. 175–202, doi:10.1016/j.precamres.2010.08.004.
- Dahlen, FA, Hung, S-H and Nolet, G 2000, Fréchet kernels for finite-frequency traveltimes—I. Theory: *Geophysical Journal International*, v. 141, no. 1, p. 157–174.
- Griffin, WL, O'Reilly, SY and Ryan, CG 2004, The composition and origin of subcontinental lithospheric mantle: *American Geophysical Union, Geophysical Monograph Series* v. 150, p. 13–45.
- Kennett, BLN, Sambridge, MS and Fishwick, S 2013, *Lithospheric structure in Australia from seismic tomography*: Geological Society, London, Special Publications, v. 380, p. 5–30.
- Mole, DR, Fiorentini, ML, Thébaud, N, Cassidy, KF, McCuaig, TC, Kirkland, CL, Romano, SS, Doublier, MP, Belousova, EA and Barnes, SJ 2014, Archean komatiite volcanism controlled by the evolution of early continents: *Proceedings of the National Academy of Sciences*, v. 111, no. 28, p. 10083–10088.
- Montelli, R, Nolet, G, Dahlen, FA, Masters, G, Engdahl, ER and Hung, S-H 2004, Finite-frequency tomography reveals a variety of plumes in the mantle: *Science*, v. 303, no. 5656, p. 338–343.
- Murdie, RE, Yuan, H, O'Donnell, JP, Johnson, SP, Ebrahimi, R and Rashidifard, M 2024, WA Array: A high-resolution passive-source seismic survey to image the West Australian lithosphere: *Seismological Research Letters*, v. 95, no. 5, p. 3093–3108, doi: 10.1785/0220230415.
- Robertson, GS and Woodhouse, JH 1995, Evidence for proportionality of P and S heterogeneity in the lower mantle: *Geophysical Journal International*, v. 123, no. 1, p. 85–116.
- Sheppard, S and Cassidy, KF 2012, Crustal evolution and metallogeny of the Yilgarn Craton; Preface: *Mineralium Deposita*, v. 47, no. 7, p. 715–719.
- Smithies, RH, Champion, DC and Cassidy, KF 2003, Formation of Earth's early Archaean continental crust: *Precambrian Research*, v. 127, 1–3, p. 89–101.
- Smithies, RH, Gessner, K, Lu, Y, Kirkland, CL, Ivanic, T, Lowrey, JR, Champion, DC, Sapkota, J, Masurel, Q and Thébaud, N 2024, Geochemical mapping of lithospheric architecture disproves Archean terrane accretion in the Yilgarn Craton: *Geology*, v. 52, no. 2, p. 141–146.
- Trampert, J and van der Hilst, RD 2005, Towards a quantitative interpretation of global seismic tomography: *Geophysical Monograph Series*, v. 160, p. 47–62.
- van Kranendonk, MJ, Hugh Smithies, R, Hickman, AH and Champion, DC 2007, Secular tectonic evolution of Archean continental crust: interplay between horizontal and vertical processes in the formation of the Pilbara Craton, Australia: *Terra Nova*, v. 19, no. 1, p. 1–38.
- Wilde, SA, Middleton, MF and Evans, BJ 1996, Terrane accretion in the southwestern Yilgarn Craton: evidence from a deep seismic crustal profile: *Precambrian Research*, v. 78, 1–3, p. 179–196.
- Xu, X, Zhao, L, Wang, K and Yang, J 2018, Indication from finite-frequency tomography beneath the North China Craton: The heterogeneity of craton destruction: *Science China Earth Sciences*, v. 61, no. 9, p. 1238–1260, doi:10.1007/s11430-017-9201-y.
- Yuan, H and Dueker, K 2005, Upper mantle tomographic V_p and V_s images of the Rocky Mountains in Wyoming, Colorado and New Mexico: Evidence for a thick heterogeneous chemical lithosphere: *Geophysical Monograph Series*, v. 154, p. 329–345.
- Yuan, H, Zhang, P, Pickle, R, Miller, MA, Murdie, RE, Li, T and Gessner, K 2024, P-wave receiver function models from SWAN data, in *South West Australia Network (SWAN): passive seismic imaging and hazard analysis compiled by RE Murdie and MS Miller*: Geological Survey of Western Australia, Report 255, p. 50–57.
- Zhang, P, Miller, MS, Magrini, F, Pickle, R and Yuan, H 2024, 3D V_s model of the Earth's crust in southwest Western Australia from ambient noise tomography, in *South West Australia Network (SWAN): passive seismic imaging and hazard analysis compiled by RE Murdie and MS Miller*: Geological Survey of Western Australia, Report 255, p. 36–41.
- Zhao, L, Paul, A, Malusà, MG, Xu, X, Zheng, T, Solarino, S, Guillot, S, Schwartz, S, Dumont, T and Salimbeni, S 2016, Continuity of the Alpine slab unraveled by high-resolution P wave tomography: *Journal of Geophysical Research: Solid Earth*, v. 121, no. 12, p. 8720–8737.

P-wave receiver function models from SWAN data

H Yuan, P Zhang¹, R Pickle¹, MS Miller¹, RE Murdie, T Li² and K Gessner

1. Research School of Earth Sciences, The Australian National University, Acton ACT 0200
2. State Key Laboratory of Lithospheric and Environmental Coevolution, Institute of Geology and Geophysics, Chinese Academy of Sciences, Beijing 100029, China

Scientific abstract

P-wave receiver functions are conventional in seismological research for delineating the Earth's internal structure. By examining the P-wave conversions to S-waves at subsurface interfaces (e.g. the Moho), these functions provide insights into the composition and thickness of the crust and upper mantle. In general, receiver function technique enhances our understanding of geological processes and the dynamic behaviour of tectonic plates, contributing to broader knowledge of seismic activity and Earth's evolution. Here, we apply a series of P-wave receiver function stacking techniques to obtain the average crustal thickness, the V_p/V_s ratio (which is used to infer average crustal composition), and a 3D volume of receiver function images that highlight the nature of the regional Moho in a continuous way. Our new models, for the first time, reveal a general north–south whole-crustal structural difference in this region of the Yilgarn Craton. When combined with recent geophysical datasets, these results will provide deeper insights into the regional tectonic history and contribute to a more comprehensive understanding of crustal evolution in this area.

KEYWORDS: crustal structure, P-wave receiver functions, Yilgarn Craton

Lay abstract

P-wave receiver functions are a key tool in seismology for understanding the structure of the Earth's continental crust. In this study, we used both single- and multiple-station stacking techniques to analyse data from the SWAN dataset, covering the southwest region of the Yilgarn Craton. Our analysis reveals the average crustal thickness, crustal composition (inferred from P- and S-wave velocities), and the continuous topography of the Moho—the boundary between the crust and the mantle. For the first time, these results highlight spatial variations in crustal properties, which can be directly linked to surface geological features such as faults, lithological boundaries, and regions of tectonic activity, providing new insights into the area's tectonic history.

Introduction

In this section, we aim to provide two P-wave receiver function (RF) models for the SWAN dataset. The two techniques applied are single-station thickness (H) versus V_p/V_s ratio (κ) – this is referred to as H- κ analysis (Zhu and Kanamori, 2000) – and multiple-station common-conversion-point (CCP) stacking technique (Dueker and Sheehan, 1997). RF methods (Langston, 1977) are generally sensitive to velocity boundaries such as the Moho and intracrustal faults. The techniques applied in this study complement each other in resolving crustal architecture. The H- κ technique provides 'bulk' crustal thickness and V_p/V_s ratio estimates beneath individual seismic stations. These are often used to infer average crustal composition (Christensen, 1996) and understand the origin and evolution of early crust (Zandt and Ammon, 1995; Chevrot and Girardin, 2000; Reading, et al., 2007; Yuan, 2015). On the other hand, CCP stacking provides a spatially continuous interface map of lithospheric discontinuities, such as the Moho (Schulte-Pelkum et al., 2005; Kind and Yuan, 2010). Identifying the topographic changes in these velocity

discontinuities has significant implications for understanding mineral deposit systems and regional tectonic evolution (e.g. Dentith et al., 2018; Hoggard et al., 2020).

Data and method

The design and deployment of the SWAN array is described by Miller et al. (2024) and Murdie et al. (2024). We collected event waveforms from 27 SWAN stations, along with nearly one year of data from several SmartSolo 5s-IGU-BD3c-s sensors which were deployed to monitor the regional swarm events near the Arthur River area (Fig. 42).

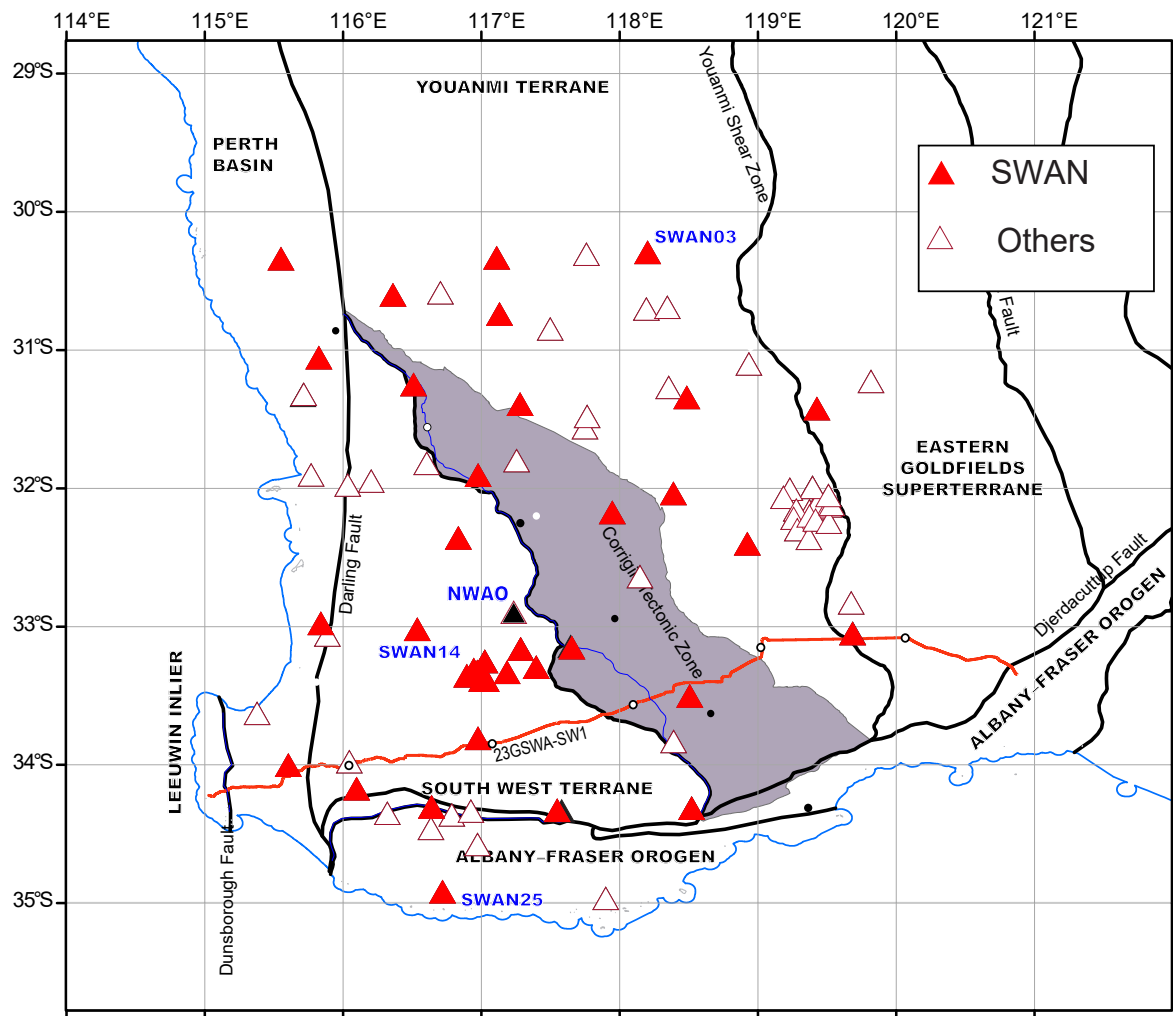


Figure 42. SWAN area map and stations used in the receiver function analysis

P-wave receiver function (RF) computation

This study applied the method developed by Yuan et al. (2010) and Yuan (2015). The method has been used in several studies in cratonic areas (Dentith et al., 2018; Li et al., 2022; Zhao et al., 2022; Yuan et al., in press) to calculate P-wave receiver functions, analysing and processing major teleseismic events ($M_s > 5.8$ and epicentral distance greater than 40° but less than 90°) and regional seismic events ($M_b > 5.2$ and great circle distance $20-40^\circ$). Before calculating the P-wave receiver functions, the event waveforms were first down-sampled to 50 Hz, then de-meaned, detrended and windowed from 50 s before to 100 s after the theoretical P-wave arrival time. The N-S and E-W components were then rotated to radial and tangential components using the SAC (Seismic Analysis Code) software and band-pass filtered with a filter of 20 s to 5 Hz.

Using the extended multi-taper spectral correlation method (Park and Levin, 2000; Helffrich, 2006), background noise was employed as a dynamic damping parameter to stabilize frequency deconvolution. Anomalous amplitudes (greater than 0.8 times the direct P-wave) and radial receiver functions that were twice the full-waveform root mean square (or standard deviation of the mean) were then removed.

Single-station H- κ stacking

For the H- κ approach, we adopted the methodology outlined in Yuan (2015) to determine the bulk crustal thickness and V_p/V_s ratio. For each pair of given crustal thickness (H) and V_p/V_s ratio, we computed the theoretical arrival times and stacked the amplitudes of the direct P-phases along with the P2p1s and P2s1p surface reverberations (Gurrola et al., 1994) using weights of 0.5, 0.3 and -0.2, respectively. The negative weight accounted for the negative polarity of the P2s1p phase. The V_p and V_s velocity models were both required to compute the phase arrivals (Gurrola et al., 1994).

We applied the regional shallow V_s model developed in the SWAN project (Zhang et al., 2024) and explored a range of V_p/V_s ratios (from 1.6 to 2.0) to derive the V_s model for arrival time calculations. The crustal thickness H was searched between 20 and 60 km, based on the regional Moho topography from the AuSREM Model (Kennett et al., 2023).

For each station, due to the long operating time, an average of over 200 events was selected (Table 5). This allowed us to apply a bootstrap resampling procedure (Efron and Tibshirani, 1986) to generate 100 datasets, each containing the same number of events. Optimal H and κ values were determined for each dataset, and the averages of these 100 optimal values were used to construct the final model.

Table 5 Average crustal thickness (H) and V_p/V_s ratio (κ) constrained by the SWAN data. Columns dH and $d(V_p/V_s)$ (i.e. $d\kappa$) show the error associated with the H and V_p/V_s ($d\kappa$) estimates. V_s and V_p are average crustal shear- and compressional-wave velocities estimated using the background V_s model and the V_p/V_s ratio. #RF stands for number of receiver functions used for the station

Station	H (km)	dH	V_p/V_s	$d(V_p/V_s)$	V_s	V_p	#RF	Quality
SWAN00	37	36.8 – 37.2	1.75	1.74 – 1.75	3.83	6.68	188	good
SWAN02	39.2	38.2 – 39.4	1.75	1.72 – 1.77	3.86	6.75	226	good
SWAN03	34.2	34.0 – 34.3	1.71	1.71 – 1.72	3.8	6.51	302	good
SWAN04	41.1	40.9 – 41.3	1.77	1.76 – 1.78	3.9	6.9	205	okay
SWAN05	33.1	33.0 – 33.3	1.71	1.70 – 1.72	3.79	6.5	233	good
SWAN07	39.1	38.5 – 39.4	1.81	1.79 – 1.82	3.84	6.94	266	okay
SWAN09	35.2	35.0 – 35.4	1.74	1.73 – 1.75	3.81	6.63	208	good
SWAN10	35.9	35.8 – 36.1	1.78	1.77 – 1.79	3.8	6.78	178	good
SWAN11	35.6	35.3 – 36.0	1.75	1.73 – 1.76	3.82	6.67	166	good
SWAN12	35.3	35.4 – 35.5	1.82	1.81 – 1.84	3.79	6.91	255	okay
SWAN14	39.7	38.4 – 39.9	1.76	1.75 – 1.78	3.83	6.74	166	good
SWAN15	45.2	44.7 – 45.8	1.88	1.87 – 1.89	3.94	7.44	255	okay
SWAN16	43.1	42.5 – 43.8	1.74	1.73 – 1.75	3.91	6.81	285	good
SWAN18	33.3	31.3 – 33.0	1.71	1.69 – 1.73	3.81	6.49	311	good
SWAN20	38.2	38.0 – 38.3	1.86	1.85 – 1.88	3.81	7.1	176	okay
SWAN21	42.4	42.0 – 42.8	1.83	1.82 – 1.85	3.86	7.07	267	okay
SWAN22	42.7	42.4 – 42.9	1.73	1.72 – 1.74	3.9	6.75	197	good
SWAN23	41.6	41.4 – 41.8	1.94	1.92 – 1.96	3.84	7.43	300	okay
SWAN25	33	32.8 – 33.6	1.69	1.68 – 1.71	3.74	6.34	228	good
SWAN26	42.2	42.0 – 42.4	1.76	1.76 – 1.77	3.9	6.89	286	okay
SWAN27	35.4	35.0 – 35.7	1.69	1.68 – 1.71	3.81	6.45	102	good
SWNND	44	43.7 – 44.1	1.75	1.73 – 1.77	3.9	6.84	139	good
SWNNE	43.8	43.5 – 44.2	1.74	1.73 – 1.75	3.9	6.79	82	good
SWNNF	40.7	39.9 – 40.2	1.77	1.76 – 1.79	3.85	6.83	84	good
SWNNG	39.6	39.3 – 39.9	1.87	1.84 – 1.89	3.84	7.16	119	okay
SWNNH	41.5	40.9 – 41.7	1.78	1.76 – 1.79	3.86	6.86	95	okay
SWNNI	40	39.7 – 40.3	1.81	1.79 – 1.82	3.84	6.93	81	okay
SWNNJ	45.3	44.7 – 45.6	1.73	1.72 – 1.74	3.93	6.79	30	okay
SWNNK	40.8	40.6 – 41.0	1.81	1.80 – 1.82	3.85	6.95	64	good

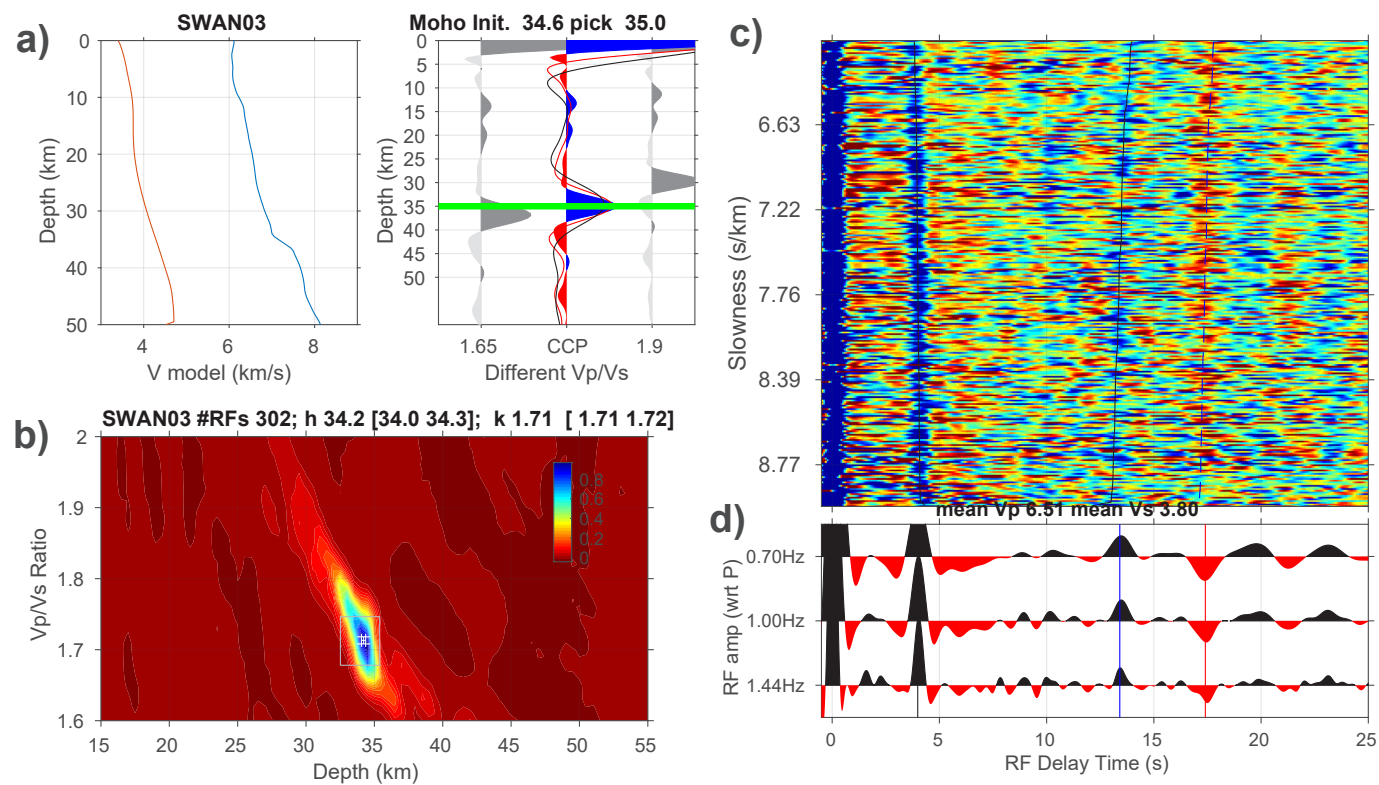


Figure 43. H- κ stacking for SWAN station SWAN03: a) reference crustal V_s (red) and V_p (blue) models and moveout-corrected receiver functions with respect to depth. By using the crustal V_s and a range of V_p models (based on 1.65 and 1.9 V_p/V_s ratio and the V_p model in a)), this procedure helps to determine the area in the depth (H) and V_p/V_s ratio (κ) space in (b) for the optimal H and κ values; b) H- κ stacking showing the maximum receiver function amplitude, where the optimal H and κ values are picked. Note this is the average of 100 bootstrapped H- κ stacks; c) slowness-sorted receiver functions and the theoretical predictions of the Moho arrival (around 4 s) and surface multiples (~ 14 s and 17 s); d) linear stacks of all receiver functions for three frequency bands (high-pass filter at 0.7, 1.0 and 1.44 Hz) to show consistency of the receiver function signals

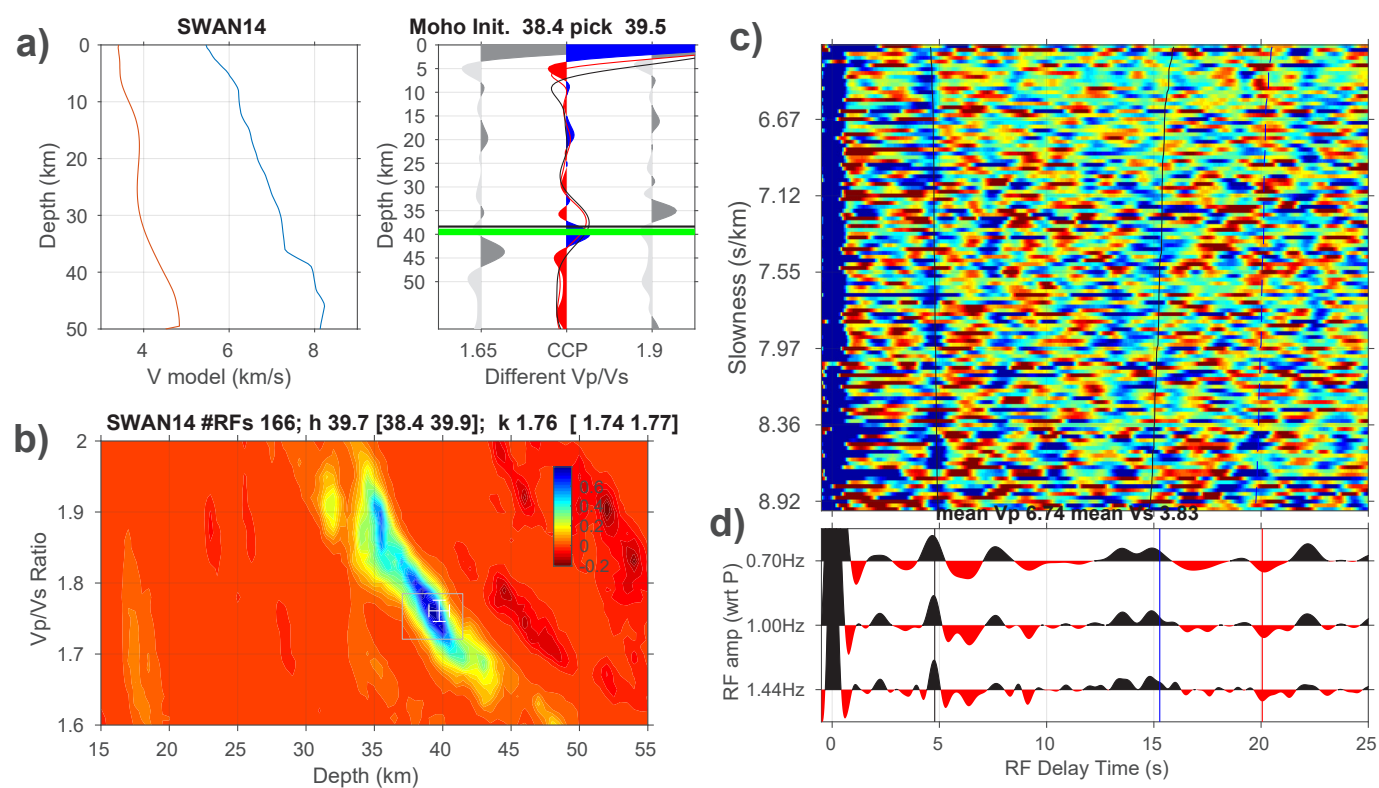


Figure 44. Same as Figure 43 but for station SWAN14 near Quindanning in the South West Terrane

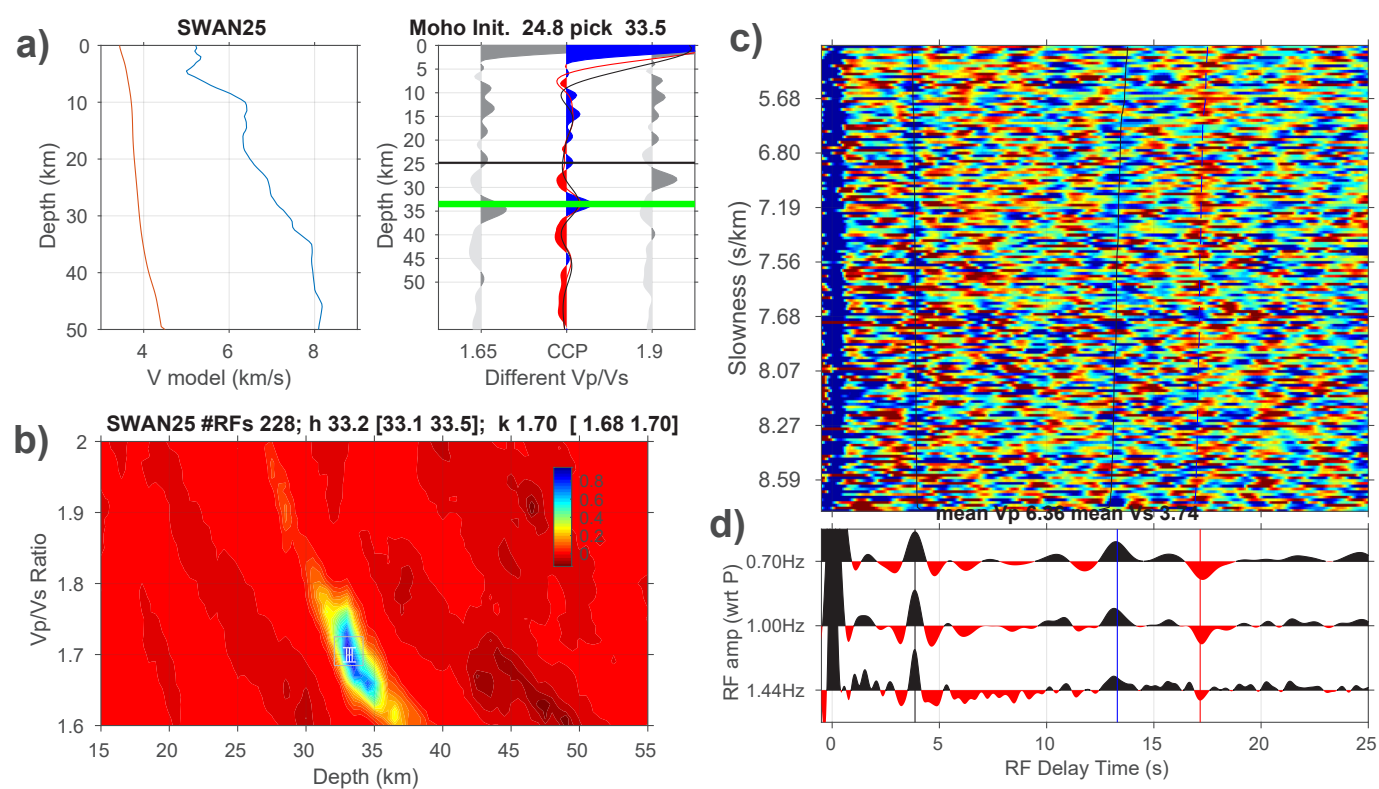


Figure 45. Same as Figure 43 but for station SWAN25 near Walpole in the Albany–Fraser Orogen

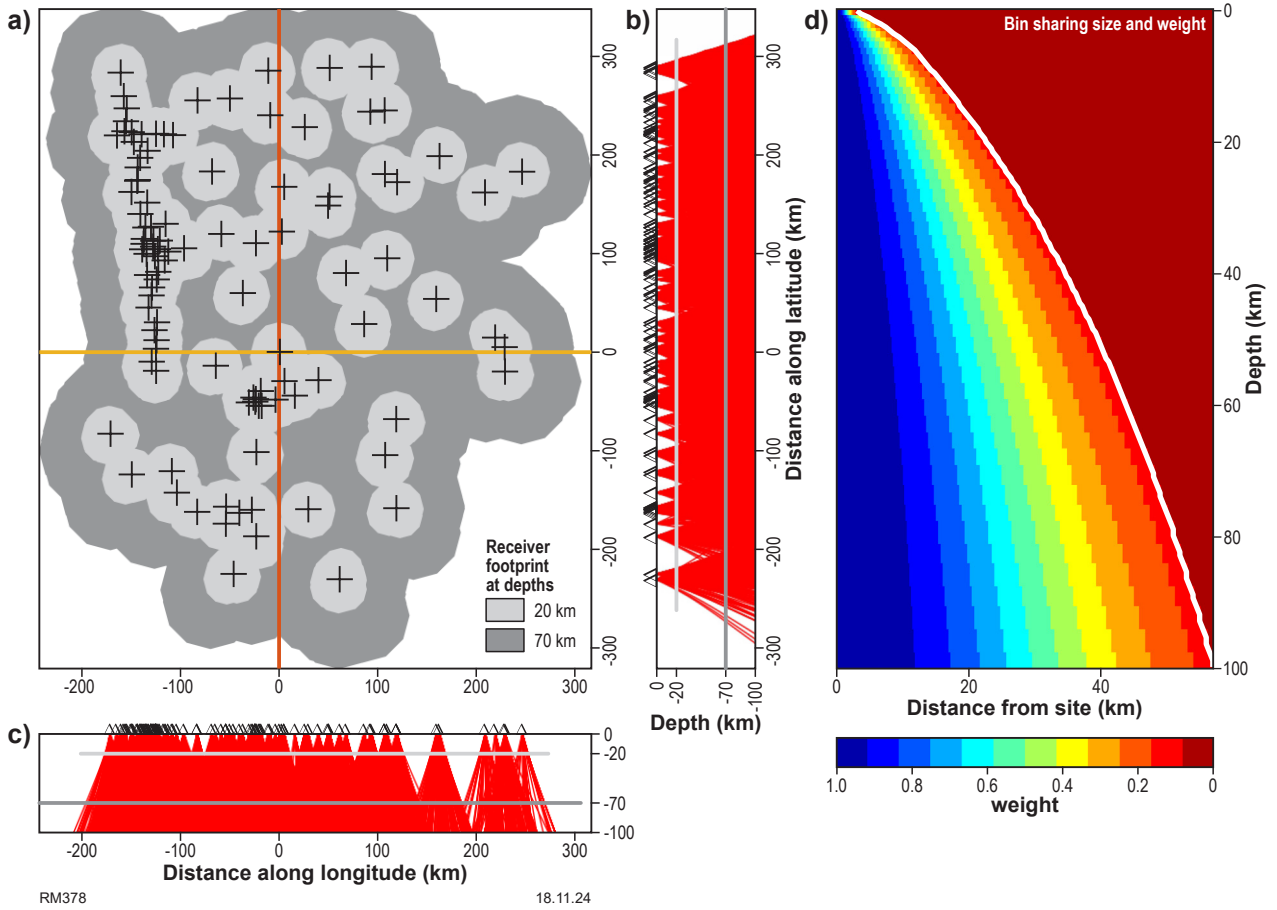


Figure 46. Common-conversion-point (CCP) stacking: a) the effective footprint of incoming ray paths at depths of 20 km (pale grey) and 70 km (dark grey); b) ray paths along the latitudinal section [red line in part (a)]; c) ray paths along the longitudinal section [yellow line in part (a)]; d) the ray at the centre has the maximum contribution (or weight). Such weights decrease when moving away from the ray and effectively reaches zero at the wide curve, which is approximated by the first Fresnel zone

Figures 43, 44 and 45 illustrate examples of H- κ analysis for selected stations in the Youanmi Terrane, the South West Terrane and the Albany–Fraser Orogen, respectively (see Fig. 42 for station location).

Optimal H- κ estimates yield the most coherent arrival times for the P-to-s converted phase from the Moho interface (referred to as Pms) and its surface multiples (or reverberations). In cases of a simple, flat Moho, this typically results in a unimodal distribution of maximum stacked receiver function amplitude, as observed at stations in both the Pilbara and Kimberley Cratons (e.g. Yuan 2015), and in the southwest Yilgarn Craton. The predicted arrival times based on the optimal model align well with the actual data (e.g. part (c) in each of Figures 43–45). However, in the Perth Basin, many stations exhibit multiple peaks in the amplitude stack due to strong basin-induced noise that contaminates the receiver function signal. Therefore, the H and κ values for these stations are usually not available.

Multiple common-conversion-point (CCP) stacking

For this approach, we applied the workflow described by Dueker and Sheehan (1997) and followed the procedures outlined in Yuan et al., (2010). The CCP model is centred at station NWA0 (Fig. 42) at the surface, extending ± 300 km in

both the longitudinal and latitudinal directions and down to a depth of 100 km. The 3D volume is divided into small blocks, each with uniform dimensions of 20 km \times 20 km \times 0.5 km. We used the receiver functions from the previous H- κ stacking and incorporated available regional data from both the permanent network (IRIS network code AU/IU) and earlier temporary deployments (Reading et al., 2007, 2012; Murdie et al., 2020). In total, over 19 000 radial RFs were used in the CCP stacking.

V_p and V_s models are both required for the CCP ray tracing to migrate the time-domain RFs to depth (Fig. 46a–c). For each station, we extracted the V_p model from the reference AuSREM models and the V_s model from the SWAN network (Zhang et al., 2024) to trace the rays and form the final stacking. In migrating the time-domain RFs to depth, for each block, the horizontal regions affected by each converted S-wave ray path were approximated by the first Fresnel zone width $\sqrt{0.5\lambda z_i}$ (Fig. 46d), where λ is the wavelength of the converted shear wave and z_i is the depth. We used a period of 2 s, which is typical for crustal P-wave RFs; these RF amplitudes projected into each block were weighted by their distance to the centre of the block (Fig. 46d).

All stations together contributed approximately 10 000 RF traces after data culling, enabling us to perform bootstrap resampling to generate 100 datasets. The CCP stacking was then performed with each of these datasets, and the resultant 100 CCP models were averaged to form the final CCP model (see section below).

Receiver function models

Bulk crustal thickness and V_p/V_s ratio models

The average crustal thickness (H) and V_p/V_s ratio values in Table 5 are plotted onto the regional geology map (Fig. 47). For each station, a radius of 25 km was used to approximate

the effective sampling region around the Moho depth.

Common-conversion-point (CCP) model

Three cross-sections (Figs. 48–50) of the CCP model that cut across the South West Terrane were created to sample the crust and shallow lithospheric upper mantle. The SWAN crustal V_s model (Zhang et al., 2024) is also presented for comparison. The velocity model is plotted in terms of velocity perturbations with respect to the station average (Fig. 48c) of all SWAN stations within the Yilgarn Craton.

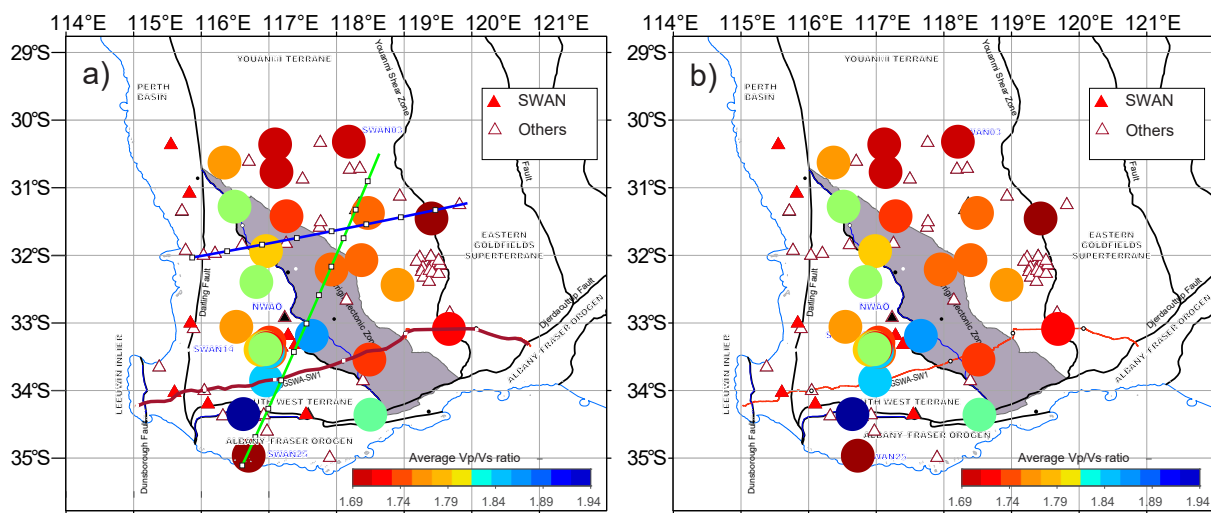


Figure 47. Map views of the average crustal thickness (H, left) and V_p/V_s ratio (κ , right) values for SWAN stations

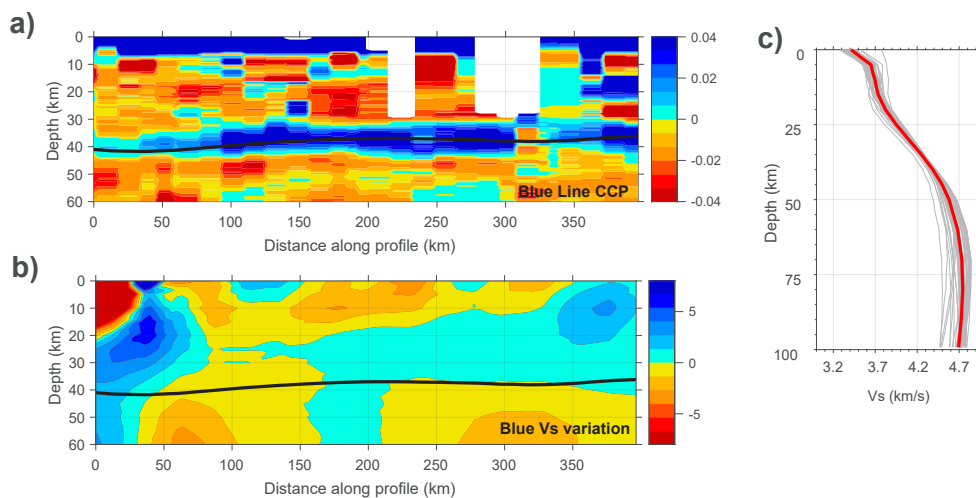


Figure 48. a) CCP and b) V_s variation models along the blue profile (see Figure 47a) in the northern study area. The V_s variations are relative to the average of the craton station velocity profiles [red line in (c)]; c) grey lines show the craton station velocity profiles. Black line in (a) and (b) is the Moho from AusMoho 2023 (Kennett et al., 2023)

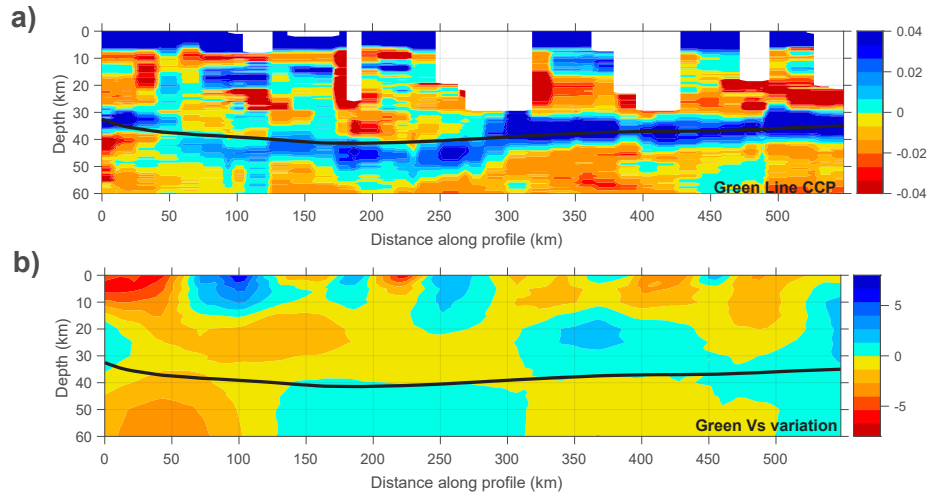


Figure 49. Same as Figure 48 but for the green profile (see Figure 47a for location)

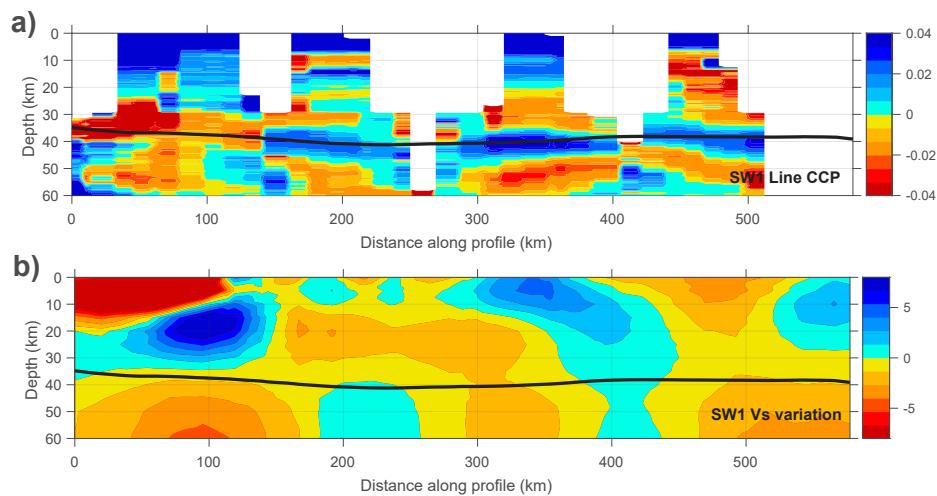


Figure 50. Same as Figure 48 but for the active-source SW1 line (see Figure 47a for location)

Discussion and conclusions

Single-station receiver function analysis (Fig. 47) reveals the following features.

1. The northern SWAN region (the Youanmi Terrane) has a generally thin (35–38 km) crust with small (felsic) V_p/V_s ratios, except along the western edge in the northern Corrigin Tectonic Zone, where the crust is thicker (~40 km) and compositionally more intermediate ($V_p/V_s \sim 1.76$).
2. The South West Terrane in general has thick crust (>40 km) and $V_p/V_s > 1.76$, possibly indicating a more mafic bulk composition.
3. Large H and κ values tend to occur near terrane boundaries, e.g. SWAN23 between the Albany–Fraser Orogen and the South West Terrane.
4. Relatively young basin areas generally do not yield robust H - κ estimates. In this case CCP stacking with RFs in various frequency bands may help find the Moho using the AuSREM V_p and SWAN V_s models.
5. In general, the SWAN study region can be divided into structurally different north and south halves.

6. The CCP model reveals more Moho topography in the region compared with the AusMoho 23 model, although significant lateral smearing is needed due to large SWAN station spacing.

The P-wave RF models from the SWAN data provide new constraints on the regional shallow lithospheric architecture. Our analysis reveals detailed insights into the crustal and upper-mantle structures, including variations in crustal thickness and V_p/V_s across the South West Terrane and the Yilgarn Craton. The application of H - κ and CCP stacking techniques has enabled a comprehensive understanding of the Moho depth and its spatial continuity across subdomains. These findings may enhance our knowledge of regional tectonic processes and provide valuable information for understanding the evolution of the Earth's crust in this area. The integration of these new models with existing geophysical datasets will contribute to more accurate interpretations of mineral deposit systems and regional tectonic history.

References

- Chevrot S and Girardin, N 2000, On the detection and identification of converted and reflected phases from receiver functions: *Geophysical Journal International*, v. 141, no. 3, p. 801–808.
- Christensen NI 1996, Poisson's ratio and crustal seismology: *Journal of Geophysical Research: Solid Earth*, v. 101 B2, p. 3139–3156, doi:10.1029/95JB03446.
- Dentith, MC, Yuan, H, Johnson, S, Murdie, R and Piña-Varas P 2018, Application of deep-penetrating geophysical methods to mineral exploration: Examples from Western Australia: *Geophysics*, v. 83, no. 3, p. WC29–WC41, doi:10.1190/geo2017-0482.1.
- Dueker, KG, and Sheehan, AF 1997, Mantle discontinuity structure from midpoint stacks of converted P and S waves across the Yellowstone hotspot track: *Journal of Geophysical Research*, v. 102 B4, p. 8313–8327.
- Efron, B and Tibshirani, R 1986, Bootstrap methods for standard errors, confidence intervals, and other measures of statistical accuracy: *Statistical Science*, v. 1, p. 54–77.
- Gurrola, H, Minster, JB and Owens, T 1994, The use of velocity spectrum for stacking receiver functions and imaging upper mantle discontinuities: *Geophysical Journal International*, v. 117, no. 2, p. 427–440, doi:10.1111/j.1365-246X.1994.tb03942.x.
- Helffrich, G 2006, Extended-time multitaper frequency domain cross-correlation receiver-function estimation: *Bulletin of the Seismological Society of America*, v. 96, p. 344–347, doi:10.1768/020050098.
- Hoggard, MJ, Czarnota, K, Richards, FD, Huston, DL, Jaques, AL and Ghelichkhan, S 2020, Global distribution of sediment-hosted metals controlled by craton edge stability: *Nature Geoscience*, v. 13, no. 7, p. 504–510, doi:10.1038/s41561-020-0593-2.
- Kennett, BLN, Gorbato, A, Yuan, H, Agrawal, S, Murdie, R, Doublier, MP, Eakin, CM, Miller, MS, Zhao, L, Czarnota, K, O'Donnell, JP, Dentith, M and Gessner, K 2023, Refining the Moho across the Australian continent: *Geophysical Journal International*, v. 233, no. 3, p. 1863–1877, doi:10.1093/gji/ggad035.
- Kind, R and Yuan, X 2010, Seismic images of the biggest crash on Earth: *Science*, v. 329, no. 5998, p. 1479–1480, doi:10.1126/science.1191620.
- Langston, CA 1977, Corvallis, Oregon, crustal and upper mantle receiver structure from teleseismic P and S waves: *Bulletin of the Seismological Society of America*, v. 67, p. 713–724.
- Li, T, Jiang, M, Zhao, L, Yao, W, Chen, L, Chu, Y, Sun, B, Ai, Y, Wan, B, Gessner, K and Yuan, H 2022, Wedge tectonics in South China: constraints from new seismic data: *Science Bulletin*, v. 67, no. 14, p. 1496–1507, doi:10.1016/j.scib.2022.05.007.
- Miller, MS, Pickle, R, Murdie, RE, Yuan, H, Allen, TI, Gessner, K, Zhang, P, Mousavi, S, Kennett, BLN and Whitney, J 2024, Southwest Australia Seismic Network (SWAN), in *South West Australia Network (SWAN): passive seismic imaging and hazard analysis compiled by RE Murdie and MS Miller*: Geological Survey of Western Australia, Report 255, p. 1–13.
- Murdie, RE, Yuan, H and Pickle, R 2024, SWAN deployment, in *South West Australia Network (SWAN): passive seismic imaging and hazard analysis compiled by RE Murdie and MS Miller*: Geological Survey of Western Australia, Report 255, p. 19–21.
- Park, J, and Levin, V 2000, Receiver functions from multiple-taper spectral correlation estimates: *Bulletin of the Seismological Society of America*, v. 90, no. 6, p. 1507–1520.
- Reading, AM, Kennett BLN and Goleby, B 2007, New constraints on the seismic structure of West Australia: Evidence for terrane stabilization prior to the assembly of an ancient continent?: *Geology*, v. 035, no. 4, p. 379–382, doi:10.1130/g23341a.1.
- Reading, AM, Tkalčić, H, Kennett, BLN, Johnson, SP and Sheppard, S 2012, Seismic structure of the crust and uppermost mantle of the Capricorn and Paterson Orogens and adjacent cratons, Western Australia, from passive seismic transects: *Precambrian Research*, v. 196–197, p. 295–308, doi:10.1016/j.precamres.2011.07.001.
- Schulte-Pelkum, V, Monsalve, G, Sheehan, A, Pandey, MR, Sapkota, S, Bilham, R and Wu, F 2005, Imaging the Indian subcontinent beneath the Himalaya: *Nature*, v. 435, no. 7046, p. 1222–1225.
- Yuan, H 2015, Secular change in Archaean crust formation recorded in Western Australia: *Nature Geoscience*, v. 8, no. 10, p. 808–813, doi:10.1038/ngeo2521.
- Yuan, H, Dueker, K and Stachnik, J 2010, Crustal structure and thickness along the Yellowstone hot spot track: Evidence for lower crustal outflow from beneath the eastern Snake River Plain: *Geochemistry, Geophysics, Geosystems*, v. 11, no. 3, p. Q03009, doi:10.1029/2009gc002787.
- Yuan, H, Levin, V, Darbyshire, F and Manke, W (in press), Crust of eastern North America 1 preserves a record of the supercontinent cycle, in *Structure and evolution of Laurussian orogens in Europe and North America from geophysical investigations edited by W Ben-Mansour*: Geological Society London, Special Publication.
- Zandt, G and Ammon, CJ 1995, Continental crust composition constrained by measurements of crustal Poisson's ratio: *Nature*, v. 374, no. 6518, p. 152–154.
- Zhang, P, Miller, MS, Magrini, F, Pickle, R and Yuan, H 2024, 3D V_s model of the Earth's crust in southwest Western Australia from ambient noise tomography, in *South West Australia Network (SWAN): passive seismic imaging and hazard analysis compiled by RE Murdie and MS Miller*: Geological Survey of Western Australia, Report 255, p. 36–41.
- Zhao, L, Tyler, IM, Gorczyk, W, Murdie, RE, Gessner, K, Lu, Y, Smithies, RH, Li, T, Yang, J, Zhan, A, Wan, B, Sun, B and Yuan, H 2022, Seismic evidence of two cryptic sutures in Northwestern Australia: Implications for the style of subduction during the Paleoproterozoic assembly of Columbia: *Earth and Planetary Science Letters*, v. 579, article no. 117342, doi:10.1016/j.epsl.2021.117342.
- Zhu, L and Kanamori, H 2000, Moho depth variation in southern California from teleseismic receiver functions: *Journal of Geophysical Research*, v. 105, p. 2969–2980.

Site classification and V_{s30} determination for seismic hazard evaluation in the SWAN seismic network, Western Australia

R Ebrahimi and TI Allen¹

1. Geoscience Australia, Symonston ACT 2609

Scientific abstract

Seismic site classification is essential for seismic hazard analysis as it helps constrain the impact of local geological conditions on the near-surface seismic-wave propagation and observed ground motion. The Southwest Australia Seismic Network (SWAN) temporary array was established to record local earthquakes for seismic hazard applications and to improve rendering of the 3D seismic structure of the crust and mantle lithosphere in southwestern Australia. Notably, the SWAN project has recorded significant seismic events, including the 2022 Arthur River earthquake sequence and the 2023 M_w 5.0 Gnowangerup earthquake. These earthquakes, together with other well-recorded events across the SWAN network, offer a rare opportunity to assess the utility of published ground-motion models (GMMs) for large-magnitude earthquakes, thereby significantly improving seismic hazard assessment in the region. Moreover, the importance of site classification is underscored as it is a critical component of GMMs, and can substantially enhance the accuracy and reliability of these models. This study uses microtremor survey methods to estimate the shallow shear-wave velocity profiles and V_{s30} values, which are the primary factors for site classification at seismic stations. Microtremor array measurements, such as high-resolution frequency-wavenumber and modified spatial autocorrelation methods, were utilized to analyse ambient vibrations, producing detailed dispersion curves for each station. To enhance the depth accuracy of velocity profiles, ellipticity curves were extracted using the RayDec method and jointly inverted with the dispersion curves. Additionally, OpenHVSr software was employed for the inversion of single-station ellipticity curves.

KEYWORDS: HVSr, seismic hazard assessment, shear-wave velocity, site classification

Lay abstract

Understanding how local geology affects seismic waves is key to characterizing the intensity of earthquake ground shaking that could affect the built environment and cause societal harm. The SWAN network in southwestern Australia recorded thousands of earthquakes, including major events such as the 5 August 2023 M_w 5.0 Gnowangerup earthquake. Site classification assesses how local ground conditions influence seismic waves, which is crucial for improving ground motion models (GMMs). These models are of primary importance to seismic hazard studies which are used across a broad range of policy and regulatory settings, and contribute to engineering design practice, risk modelling, insurance underwriting, community safety and resilience planning. However, in Australia, GMMs have been limited by a lack of local site data so that they can be referenced to a given site condition. This study uses advanced techniques to measure shallow shear-wave velocities at SWAN stations, providing essential data to enhance the development of improved GMMs and improve local site-response predictions for future large earthquakes.

Introduction

Seismic site classification (SSC) is crucial in seismic hazard analysis, helping us understand how local geological conditions affect seismic-wave propagation and ground motion. It involves categorizing sites based on their seismic response characteristics, which is essential for earthquake risk assessment, urban planning and infrastructure design. This process is important for improving ground motion models (GMMs), which estimate the shaking intensity for a given earthquake magnitude, source-to-site distance and site condition. Many older GMMs were created with limited data and did not account for local site effects. By improving SSC, we can fill this gap and enhance the reliability of GMMs used in seismic hazard assessments.

Historically, it has been recognized that softer soils amplify seismic waves (e.g. Borchardt, 1970), depending on the period of shaking causing damage during earthquakes. This led to the development of various classification schemes to categorize sites based on their expected seismic response. The National Earthquake Hazards Reduction Program (NEHRP; Building Seismic Safety Council [BSSC], 2001) in the United States, among other global initiatives, formalized these classification schemes, using V_{s30} (time-average shear-wave velocity in the upper 30 m of soil) as a standard parameter. NEHRP categorizes subsoil into five classes, from hard rock (subsoil class A) to thick medium-soft soils (subsoil class E). The Australian earthquake loading

standard (AS 1170.4–2007 [R2018]; Standards Australia, 2018) employs a similar system to the NEHRP system but with several key differences (Table 6), aligning with New Zealand’s standards to create a unified earthquake code.

In southwestern Australia, particularly in regions covered by the SWAN project, there is limited understanding of the relationship between geological materials and their response to earthquake ground shaking. This gap arises from limited ground motion and geotechnical and geophysical data, especially shear-wave velocity data, necessary to define typical V_{S30} ranges for different near-surface materials. The shallow V_S information available for all the SWAN stations are the slope-based V_{S30} estimates (Wald and Allen, 2007) and geological-proxy-based V_{S30} (McPherson, 2017; Table 7). Slope-based V_{S30} , as proposed by Wald and Allen (2007), is measured by using topographic slope as a reliable proxy for the time-averaged shear-wave velocity to 30 m depth, derived from correlations between V_{S30} measurements and topographic gradients calculated from digital elevation models (DEMs). By contrast, the Australian Seismic Site Conditions Map (ASSCM) uses surficial geology as a proxy for potential seismic behaviour. More precise SSCs using array measurements and other single-station methods can provide more accurate V_{S30} values to improve the calibration of GMMs to varying seismic site conditions.

The SWAN array (Fig. 51) was established as a temporary broadband network consisting of 27 stations to address these challenges (Murdie et al., 2020; Miller et al., 2023). The network’s objectives include recording local earthquakes for seismic hazard

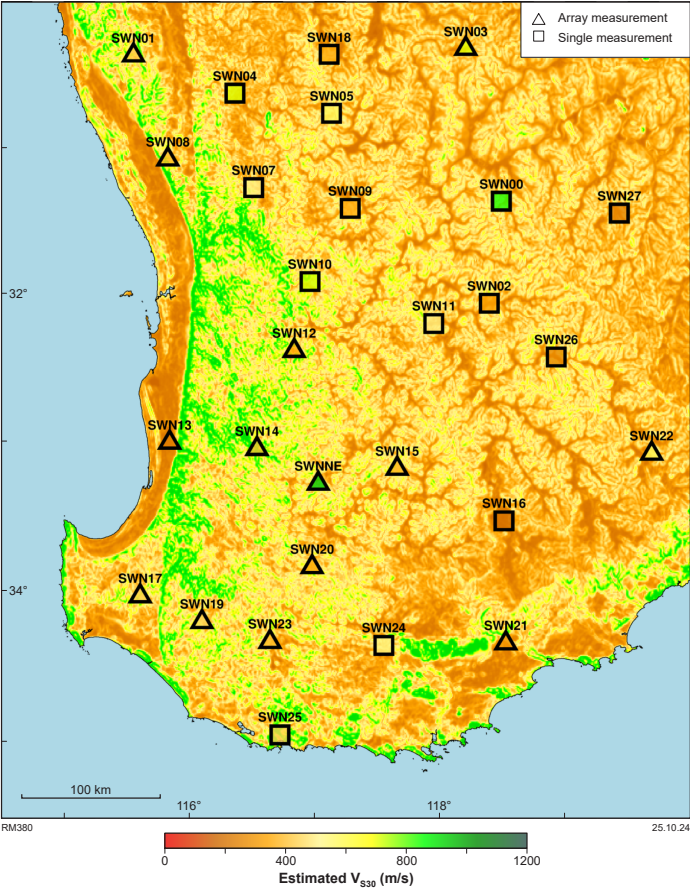


Figure 51. Map showing the spatial distribution of estimated V_{S30} values for SWAN seismic stations. Triangles represent stations estimated using the array measurement approach; squares indicate stations measured by the single-station method. The symbols are colour-coded based on the estimated V_{S30} values. The basemap displays the slope-based V_{S30} values across the region

Table 6 Seismic site classification in Australia

Site class	Generalized soil description	NEHRP (BSSC, 2001)	AS 1170.4 (Standards Australia, 2007 [R2018])	Australian Seismic Site Conditions Map (McPherson, 2017)	
			V_{S30} (m/s)		Description
A	Hard rock	> 1500	> 1500	–	–
B	Rock	760–1500	> 360	> 760	Fresh to moderately weathered hard rock units (plutonic and metamorphic rocks; most volcanic rocks; coarse-grained sedimentary rocks, Cretaceous and older)
BC	–	–	–	555–1000	Highly weathered hard rock; some Tertiary volcanic rocks
C	Very dense soil & soft rock	360–760	≤ 0.6 s (surface to rock)	360–760	Sedimentary rocks of Oligocene age; coarse-grained sedimentary rocks of younger age; extremely weathered hard rock units
CD	–	–	–	270–555	Sedimentary rocks of Miocene and younger age, unless formation is notably coarse-grained; Plio-Pleistocene alluvial units; older (Pleistocene) alluvium; some areas of coarse younger alluvium
D	Dense to medium soils	180–360	> 0.6 s (surface to rock)	180–360	Young (Holocene to Late Pleistocene) alluvium
DE	–	–	–	90–270	Fine-grained alluvial, deltaic, lacustrine and estuarine deposits
E	Medium to soft soils	< 180	Greater than 10 m soil depth with $V_S \leq 150$	< 180	Intertidal and back-barrier swamp deposits

applications and enhancing the rendering of the 3D seismic structure of the crust and mantle lithosphere. The data gathered are essential for better characterizing the location, depth and attenuation of regional earthquakes, thereby improving the understanding of seismic hazards in the region. Since its initiation in late 2020, SWAN has recorded a significant earthquake swarm near the community of Arthur River, including three events in 2022 and another in 2023 with local magnitudes of 4.0 and larger (Murdie et al., 2022). This region has historically recorded some of the highest seismic activity levels in Australia, including notable events such as the 2023 Gnowangerup earthquake (Murdie et al., 2022), the 2018 Lake Muir earthquakes (Clark et al., 2020; Standen et al., 2021), and the 1968 Meckering earthquake (Gordon and Lewis 1980; Vogfjörð and Langston 1987). These events highlight the local seismic hazard and the risk posed to Western Australian communities.

The objective of this study is to estimate the shallow shear-wave velocity profile of SWAN sites using microtremor survey methods and to estimate the V_{s30} values specific to the SWAN seismic recording stations. This understanding will serve as a foundation for the evaluation and choice of GMMs for application in both deterministic (scenario-based) and probabilistic seismic hazard assessments (e.g. Ghasemi and Allen, 2022). These assessments will enable earthquake risks to be evaluated for vulnerable communities in Western Australia.

Microtremor survey methods

Observation of microtremors can give useful information on both static and dynamic properties of a site, such as its natural frequency, f_0 , and shear-wave velocity, V_s . From the definition, a microtremor is a low-amplitude (in the order of micrometres) ambient vibration of the ground caused by man-made or atmospheric disturbances (Nakamura, 1989).

Seismic ambient noise analysis has become a prominent technique for modelling subsurface shear-wave velocity structures and evaluating site effects (Bonnefoy-Claudet et al., 2006; Foti et al., 2011). Beyond seismic hazard assessments, microtremor methods have broader applications, such as determining the depth of bedrock or estimating the cover thickness of sedimentary layers. These applications are particularly valuable in engineering and resource exploration, where understanding subsurface conditions is critical.

Microtremor measurements are used to extract dispersion curves, which describe the dispersive characteristics of surface waves. These curves show how different frequencies penetrate to different depths, revealing detailed information about the subsurface structure. To enhance the accuracy of shear-wave velocity profiles, we also analyse ellipticity curves of Rayleigh waves, which are sensitive to the vertical shear-wave velocity. Ellipticity is preferred over the standard horizontal-to-vertical spectral ratio (HVSr), which is used for single-station measurements, because HVSr results are influenced by body waves (P-waves and S-waves, as well as horizontal shear (S_H) waves). By focusing on ellipticity, we eliminate these influences, allowing for more accurate joint inversion with dispersion curves. In this study, we used several well-established array and single-station methods, as follows.

Vertical high-resolution frequency-wavenumber (HRFK) method (Fäh et al., 2008; Poggi and Fäh, 2010). This operates with sliding time windows and narrow frequency bands to measure wave propagation parameters such as azimuth and slowness for the most coherent plane wave arrivals. This technique enables the extraction of phase velocity dispersion curves for Rayleigh and Love waves by analysing vertical and transverse components, respectively.

Modified Spatial Autocorrelation (MSPAC) method (Bettig et al., 2001) which accommodates arbitrary array layouts. This method is especially useful in urban settings where regular circular arrays are impractical.

Rayleigh three-component beamforming (RTBF) method (Wathelet et al., 2018).

RayDec method to extract the Rayleigh wave ellipticity curve (Hobiger et al., 2009).

Due to access challenges and the permitting requirements for some SWAN sites, microtremor array measurements were performed at 14 of the 27 stations (Fig. 51). For the remaining stations, we measured the V_s profiles by the single-station method, using the inversion of the ellipticity curves.

Microtremor array measurements

The choice of array geometry often involves a trade-off between theoretical principles and practical constraints. While various ideal configurations are possible, geometries with uniform directional response, such as circular or triangle arrays, are preferred. However, limitations imposed by available space and site access can lead to irregular and suboptimal array configurations, such as L-shaped layouts. Examples of the array geometries employed at SWAN stations are shown in Figure 52.

At each location, we used three-component geophones to measure and characterize near-surface V_s profiles. By analysing surface waves from ambient vibrations (i.e. background noise), we obtained well-constrained information on shear-wave velocity to a few hundred metres depth. The results of these analyses converged to define a set of representative 1D shear-wave velocity profiles for each site.

In our study, the extraction of Rayleigh wave ellipticity is a crucial step for performing a joint inversion with the dispersion curves. Ellipticity is generated by the elliptical motion of Rayleigh waves. Specifically, it reflects the vertical shear (S_v) motion within the wave. By focusing on ellipticity, we can minimise the influence of body waves and other surface waves.

The objective of SSC is to develop a velocity profile at each site. To do this we employed an inversion process which used two methods for defining layered Earth models: Layering by Number (LN) and Layering Ratio (LR) (Vantassel and Cox, 2020). LN involves selecting models with different numbers of layers (3, 4, 5 and 7), while LR uses ratios (1.2, 1.5, 2.0 and 3.0) to determine layer depth ranges. By applying these methods across various parameters, including V_s , primary-wave velocity (V_p), and density, we generated over a million models to fit both dispersion and ellipticity curves.

Figure 53a displays the inversion results for station SWN15,

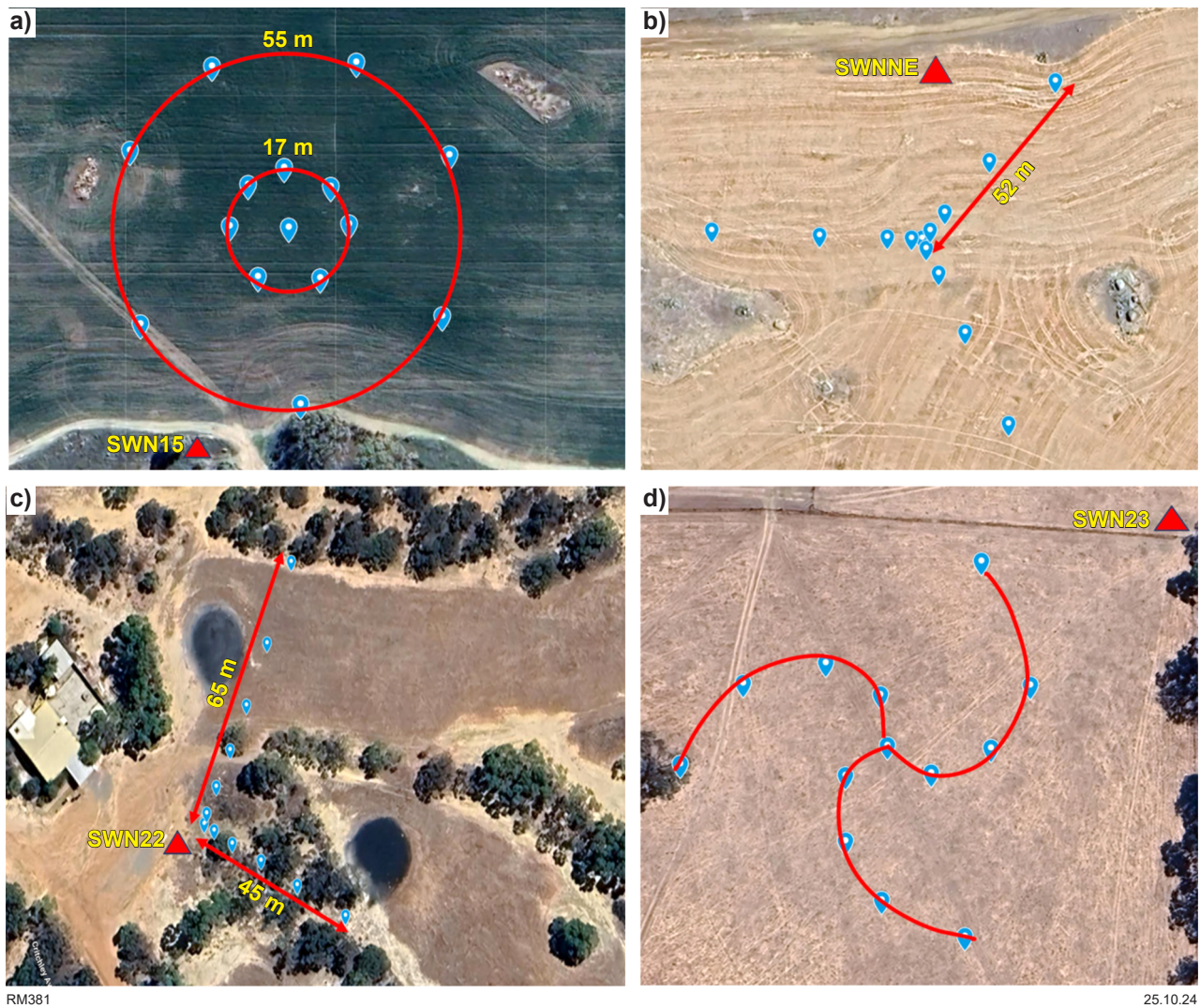


Figure 52. Examples of array geometries used to acquire ambient vibrations at the SWAN sites: a) layout of nested circular arrays at radii of 17 and 55 m; b) a triangular array, with each leg measuring 52 m; c) an L-shaped layout, with legs measuring 65 and 45 m; d) a spiral array layout, with each arm measuring 55 m. Red triangles in each image are the station locations

showing the best profiles with lowest misfit obtained from each parametrization. Further exploration involves showcasing the 10 lowest misfit profiles (Fig. 53b) and 100 lowest misfit profiles (Fig. 53c). These observations align quantitatively in Figure 53d, where uncertainty ($\sigma_{\ln V_s}$) is smallest near the surface and gradually increases with depth. The evident bulges in $\sigma_{\ln V_s}$ correspond to the layer boundary locations, which combines layer boundary uncertainty with the uncertainty of V_s , thereby exaggerating the uncertainty of these model regions.

Single-station measurements

The single-station method calculates the horizontal-to-vertical spectral ratio (HVSr) from simultaneous measurements using a tri-axial seismometer. To get a reliable HVSr peak and curve, we followed the available guidelines, such as sufficient recording duration, consistency across time segments, and low noise levels (SESAME Deliverable D08.02, 2003). For a significant HVSr peak, the requirements are a clear peak amplitude, consistency over time, a reasonable peak plus or minus standard deviation of frequency less than 5%, and comparison with array data

if available. If the HVSr curve shows a significant peak that meets these criteria, it suggests a site effect with potential amplification of seismic motion at a specific frequency, likely indicating a sharp velocity contrast in the local geological structure. For single-station measurement at SWAN sites, ambient noise recordings ranging from 3 to 24 hours were processed following SESAME (SESAME Deliverable D08.02, 2003) procedures. Each component of the raw data was divided into 100-second windows to avoid transient contamination (i.e. earthquakes or anthropogenic noise), and the amplitude spectra of the two horizontal components were averaged and divided by the vertical component's spectrum to obtain HVSr estimates. Figure 54 illustrates an example of HVSr measurement for station SWN24.

For the single-station inversion process, in addition to the standard HVSr, the Rayleigh wave ellipticity, which is specifically sensitive to vertical V_s , was obtained using the RayDec method and inverted with 'OpenHVSr' software (Bignardi et al., 2016). The difference between the standard HVSr (yellow) and the observed ellipticity (black) obtained using the RayDec method (Hobiger et al., 2009) is shown in Figure 55. The inversion process to find the velocity profile is highly non-unique, but the use of shallow 1D velocity

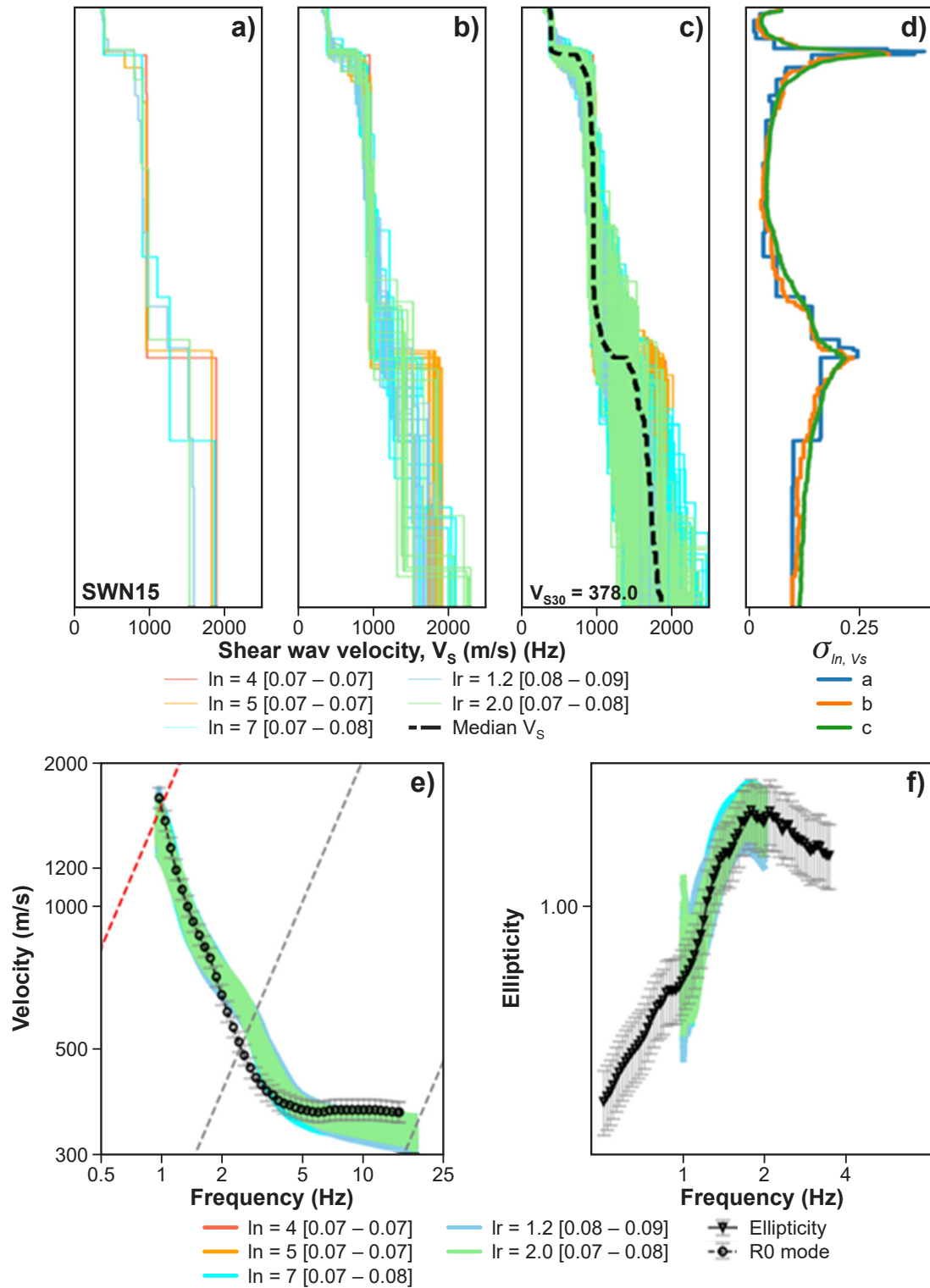


Figure 53. Inversion results for station SWN15 are presented to address V_s uncertainty using approximate methods through three approaches: a) considering the best model from each accepted inversion parametrization; b) considering the 10 lowest misfit models from each accepted inversion parametrization; c) considering the 100 lowest misfit models from each accepted inversion parametrization. The black dashed line shows the median of the accepted 100 lowest misfit models; d) corresponding σ_{ln, V_s} for each previously mentioned panel with the range of the misfit values mentioned in the square brackets; e) example of fitting the best inversion solutions on the observed Rayleigh dispersion curve; dashed black lines are array limits using FK method; red dashed line is the MSPAC method resolution limit; f) example of fitting observed ellipticity curve with the best inversion solutions

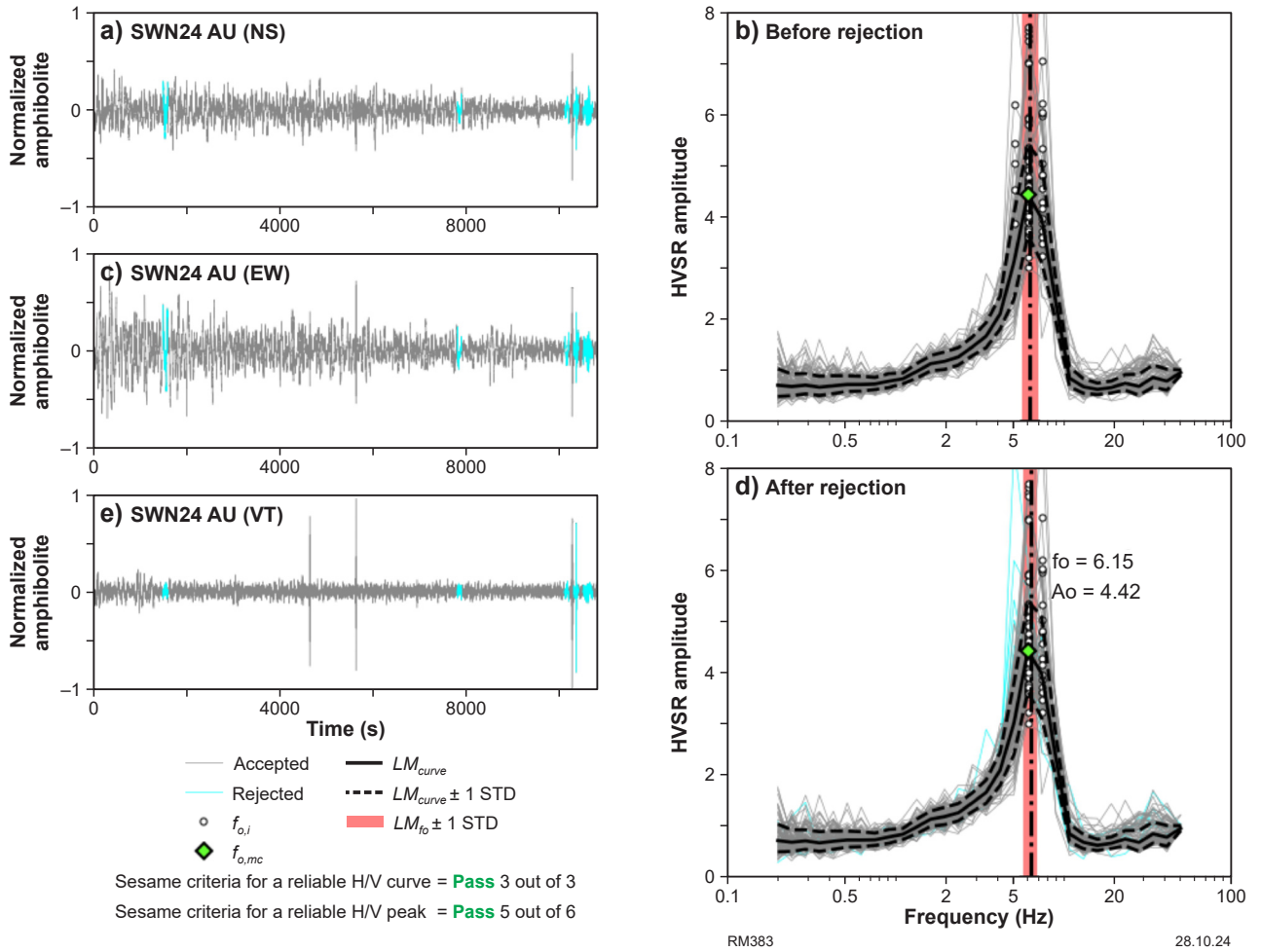


Figure 54. Example of HVSr measurement for station SWN24: a), c), e) three-component time records with blue windows indicating those rejected because of contamination by transient noise; b) HVSr curves obtained before applying any rejection algorithm; black circles identify all natural frequency ($f_{0,i}$) values; d) HVSr curves obtained after applying the frequency-domain window-rejection algorithm; blue lines identify all rejected $f_{0,i}$ values. The red error bar shows the standard deviation of the log-normal median of the f_0 (LM_{f_0}). Number of passed SESAME criteria (SESAME Project, 2004) for a reliable curve and clear peak during the process is also shown at the bottom of the figure

profiles can significantly improve the uniqueness (Hobiger et al., 2013). Our method starts with an initial model based on the natural frequency (f_0) and amplification factor (A_0) from HVSr data, using a low-speed layer over a semi-infinite space (Fig. 55b).

Thickness of the initial model (h) can be estimated from $h = V_s/(4f_0)$ (Nakamura, 1989), V_s being the shear-wave velocity of the top layer. Using the amplification factor $A_0 = V_{SB}/V_s$, assuming a shear-wave velocity for bedrock $V_{SB} = 1500 \text{ m/s}$ (Nakamura, 2000), we calculated layer thickness $h = V_{SB}/(4A_0 f_0)$. The shallow V_s information used in this inversion was the slope-based V_{s30} (Wald and Allen, 2007).

The inversion of ellipticity curves (Bignardi et al., 2016) was performed to find the best 1D profile of V_s to depth through iterative perturbations. Comparing modelled results with the observed HVSr fundamental frequency (Fig. 55a), we find that the modelled theoretical peak frequency (6.95 Hz) closely matches the observed peak (6.15 Hz) at station SWN24, confirming that the estimated V_s profile accurately reflects subsurface impedance boundaries (Wathelet et al., 2008; Wathelet, 2005; SESAME Project, 2004).

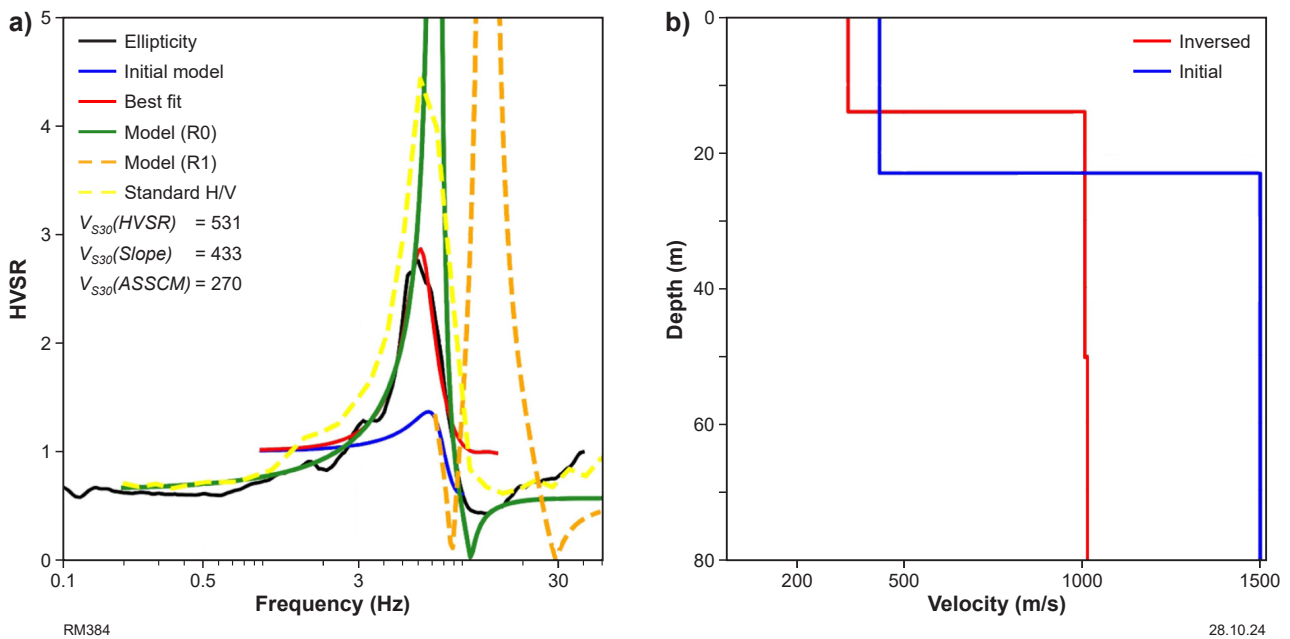


Figure 55. Result of the shear-wave velocity profile inversion process for station SWN24: a) observed HVSr ellipticity curve (black line), standard H/V (yellow), initial curve model (blue line), final best-fitted model from the inversion (red line), forward-modelled fundamental mode of Rayleigh wave ellipticity (green line), and modelled first higher mode of Rayleigh wave ellipticity (dashed orange line). The V_{S30} values from geological proxy-based (McPherson, 2017) method, slope-based (Wald and Allen, 2007) method and inversion of HVSr curves are also shown; b) shear-wave velocity structure obtained from inversion of HVSr curve (red line) compared with initial model (blue line)

Discussion and conclusions

The HVSr method is a cost-effective way of assessing site effects, especially in areas without prior geophysical data (Nakamura, 1989). The method works well with strong impedance contrasts but often shows minimal amplification in hard rock or thick sediment sites, as seen in stations SWN12 and SWN14 (Fig. 56a,b). At these stations, HVSr curves failed due to the presence of stiff top layers, and showed flat responses due to minimal velocity contrasts in the top 80 m. Array measurements for these stations (Fig. 56c,d) suggest a V_{S30} of 350–400 m/s in the presence of deep sediment without significant velocity contrast, highlighting the HVSr method's limitations. This discrepancy emphasizes the need for caution when using HVSr curves and natural frequency alone for site classification. In such cases, complementary methods such as array measurements provide a more accurate assessment of subsurface conditions.

For the sites where the array and HVSr measurements were not possible (SWN04, SWN09 and SWN10), we used average V_{S30} values from geological proxy-based (McPherson, 2017) and slope-based (Wald and Allen, 2007) methods (Fig. 51; Table 7).

The results from our study demonstrate the strengths and limitations of both the HVSr and array methods in site classification. The HVSr method, while cost-effective and useful in areas lacking detailed subsurface information, can sometimes provide misleading results in sites with stiff top layers as shown by stations SWN12 and SWN14; in this case, array measurements provided a more reliable V_{S30} value, highlighting the importance of using multiple methods for accurate site characterization.

The findings from this study provide important station metadata that can augment ground motion datasets (e.g. Ghasemi and Allen, 2021; Allen et al., 2024). These datasets support the development and refinement of GMMs that are appropriate for Australian continental crust, which are crucial for future updates of the National Seismic Hazard Assessment (e.g. Allen et al., 2023).

Table 7 Results showing natural frequency and V_{s30} values from geological proxy-based method (McPherson, 2017), slope-based method (Wald and Allen, 2007) and inversion of single-station HVSR curves, and array measurements for SWAN seismic stations

<i>Station</i>	<i>ASSCM site classification</i>	<i>ASSCM V_s</i>	<i>USGS V_s</i>	<i>Array V_s</i>	<i>HVSR V_s</i>	<i>Natural frequency (Hz)</i>
SWN00	B	1100	670.2	nan	838	9
SWN01	CD	360	719.2	423.2	nan	0.29
SWN02	D	270	240.8	nan	332.4	3.82
SWN03	CD	360	231.4	707.2	nan	4.73
SWN04	B	1100	318.3	nan	nan	nan
SWN05	C	560	340.5	nan	573.2	3.82
SWN07	B	1100	464.6	nan	497.2	3.82
SWN08	CD	360	574.1	390	nan	0.23
SWN09	D	270	451.0	nan	nan	nan
SWN10	B	1100	333.2	nan	nan	nan
SWN11	D	270	285.7	nan	499	2.48
SWN12	B	1100	349.8	354.7	nan	nan
SWN13	CD	360	233.8	235	nan	1.75
SWN14	B	1100	898.92	401	nan	nan
SWN15	C	560	457.0	378	nan	5.86
SWN16	D	270	241.5	nan	197	1.62
SWN17	C	560	756.4	433.9	nan	4.2
SWN18	CD	360	473.1	nan	355	3.47
SWN19	C	560	443.9	456.9	nan	3.47
SWN20	B	1100	401.3	346.6	nan	2.87
SWN21	CD	360	307.5	295.7	nan	1.1
SWN22	C	560	483.5	580.4	nan	5.09
SWN23	C	560	617.4	389.1	nan	3.47
SWN24	D	270	432.7	nan	531.4	6.15
SWN25	D	270	899.2	nan	442.18	3.47
SWN26	D	270	238.9	nan	260.6	1.96
SWN27	D	270	272.7	nan	248	1.97
SWNNE	B	1100	435.9	936.9	nan	nan
SWN00	B	1100	670.2	nan	838	9

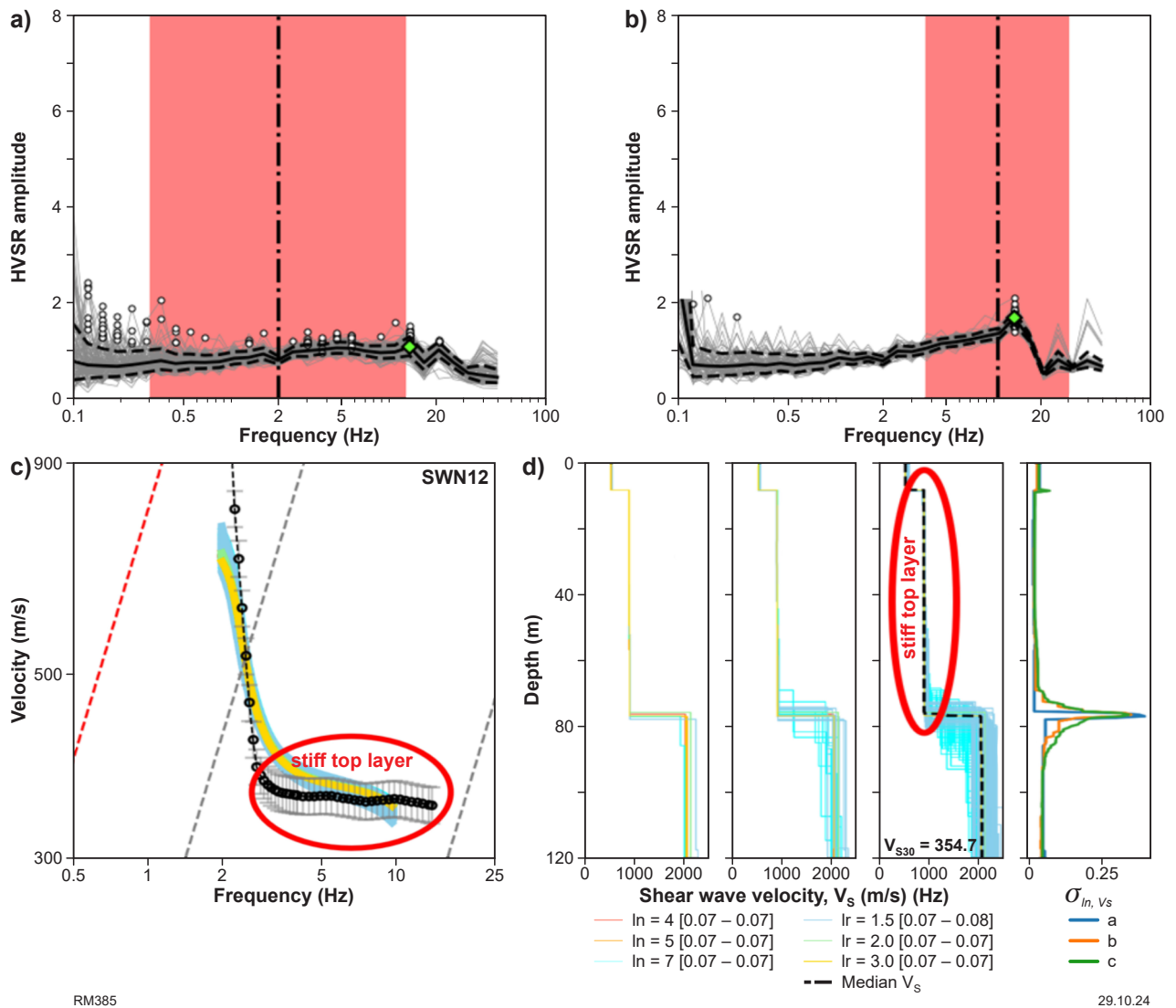


Figure 56. HVSR curves for stations that failed to exhibit a clear peak in the fundamental frequency attributed to the presence of stiff top layers: a) SWN12; b) SWN14; c) dispersion curve of the fundamental Rayleigh wave phase velocity at station SWN12, highlighting the influence of stiff top layers between 3 Hz and 15 Hz; d) inverted velocity profile at station SWN12, indicating deep sediment extending to 78 m without significant velocity contrast (details of each panel as for Figure 53a–d)

References

- Allen, TI, Ghasemi, H and Ebrahimi, R 2024, Seismology down under: developing engineering ground-motion databases in regions of low seismicity and sparse monitoring networks: 18th World Conference on Earthquake Engineering, Milan, Italy, June 30 – July 5, 2024.
- Allen, TI, Griffin, JD, Clark, DJ, Cummins, PR, Ghasemi, H and Ebrahimi, R 2023, The 2023 National Seismic Hazard Assessment for Australia: model overview: Geoscience Australia Record 2023/53, 152p, doi:10.26186/148969.
- Bard, PY, Bonnefoy-Claudet, S and Cotton, F 2004, SESAME: site effects assessment using ambient excitations. Optimum deployment strategy for array measurements. European Commission-Research General Directorate Project No. EVG1 CT 26.
- Bettig, B, Bard, PY, Scherbaum, F, Riepl, J, Cotton, F, Cornou, C and Hatzfeld, D 2001, Analysis of dense array noise measurements using the modified spatial auto-correlation method (SPAC): application to the Grenoble area: Bollettino di Geofisica Teorica ed Applicata, v. 42, no. 3–4, p. 281–304.
- Bignardi, S, Mantovani, A and Zeid, NA 2016, OpenHVSR: imaging the subsurface 2D/3D elastic properties through multiple HVSR modelling and inversion: Computers and Geosciences, v. 93, p. 103–113.
- Bignardi, S, 2017, The uncertainty of estimating the thickness of soft sediments with the HVSR method: A computational point of view on weak lateral variations: Journal of Applied Geophysics, v. 145, p. 28–38.
- Bonnefoy-Claudet, S, Cotton, F and Bard, PY 2006, The nature of noise wavefield and its applications for site effects studies: A literature review: Earth-Science Reviews, v. 79, no. 3–4, p. 205–227.
- Bonnefoy-Claudet, S, Köhler, A, Cornou, C, Wathelet, M, Bard, P-Y 2008, Effects of love waves on microtremor H/V ratio. Bulletin of the Seismological Society of America, v. 98, p. 288–300.
- Borcherdt, RD 1970, Effects of local geology on ground motion near San Francisco Bay: Bulletin of the Seismological Society of America, v. 60, p. 29–61, doi:10.1785/BSSA0600010029.
- Clark, DJ, Brennand, S, Brenn, G, Garthwaite, MC, Dimech, J, Allen, TI and Standen, S 2020, Surface deformation relating to the 2018 Lake Muir earthquake sequence, southwest Western Australia: new insight into stable continental region earthquakes: Solid Earth, v. 11, no. 2, p. 691–717, doi:10.5194/se-11-691-2020.
- Cox, BR, Cheng, T, Vantassel, JP and Manuel, L 2020, A statistical representation and frequency-domain window-rejection algorithm for single-station HVSR measurements: Geophysical Journal International, v. 221, no. 3, p. 2170–2183.

- Fäh, D, Kind, F and Giardini, D 2001, A theoretical investigation of average H/V ratios: *Geophysical Journal International*, v. 145, no. 2, p. 535–549.
- Fäh, D, Wathelet, M, Kristekova, M, Havenith, H, Endrun, B, Stamm, G, Poggi, V, Burjáněk, J and Cornou, C 2009, Using ellipticity information for site characterisation: NERIES JRA4 ‘Geotechnical Site Characterisation’. task B, section 2.
- Fäh, D, Wathelet, M, Kristekova, M, Havenith, H, Endrun, B, Stamm, G, Poggi, V, Burjáněk, J and Cornou, C 2009, Using ellipticity information for site characterisation: NERIES deliverable JRA4D4, Final Report, <www.neries-jra4.geopsy.org>.
- Foti S, Parolai S, Albarello D and Picozzi M 2011, Application of surface wave methods for seismic site characterisation: *Surveys in Geophysics*: v. 32, no. 6, p. 777–825.
- Foti, S, Hollender, F, Garofalo, F, Albarello, D, Asten, M, Bard, PY, Comina, C, Cornou, C, Cox, B, Di Giulio, G and Forbriger, T 2018, Guidelines for the good practice of surface wave analysis: a product of the InterPACIFIC project: *Bulletin of Earthquake Engineering*, v. 16, p. 2367–2420.
- Ghasemi, H and Allen, T 2021, Engineering ground-motion database for western and central Australia: Australian Earthquake Engineering Society 2021, Virtual Conference.
- Ghasemi, H and Allen, T 2022, Selection of ground-motion models for National Seismic Hazard Assessment of Australia: Australian Earthquake Engineering Society 2022 Conference, Mount Macedon, Victoria.
- Ghasemi, H and Allen, T 2023, Development of a web portal for Australian ground-motion data: Australian Earthquake Engineering Society 2022 Conference, Brisbane, Queensland.
- Gordon, FR and Lewis, J D 1980, The Meckering and Calingiri earthquakes October 1968 and March 1970: Geological Survey of Western Australia, Bulletin 126, 229p.
- Hobiger, M, Bard, PY, Cornou, C and Le Bihan, N 2009, Single-station determination of Rayleigh wave ellipticity by using the random decrement technique (RayDec): *Geophysical Research Letters*, v. 36, no. 14, p. 1–5.
- Hobiger, M, Cornou, C, Wathelet, M, Giulio, GD, Knapmeyer-Endrun, B, Renalier, F, Bard, PY, Savvaidis, A, Hailemichael, S, Le, BN and Ohrnberger, M 2013, Ground structure imaging by inversions of Rayleigh wave ellipticity: sensitivity analysis and application to European strong-motion sites: *Geophysical Journal International*, v. 192, no. 1, p. 207–229.
- McPherson, AA 2017, A revised seismic site conditions map for Australia: Geoscience Australia, Record 2017/12, 40p., doi:10.11636/Record.2017.012.
- McVerry, GH, Zhao, JX, Abrahamson, NA and Somerville, PG 2006, New Zealand acceleration response spectrum attenuation relations for crustal and subduction zone earthquakes: *Bulletin of the New Zealand Society for Earthquake Engineering*, v. 39, no. 1, p. 1–58.
- Miller, MS, Pickle, R, Murdie, RE, Yuan, H, Allen, TI, Gessner, K, Kennett, BLN and Whitney, J 2023, Southwest Australia Seismic Network (SWAN): Recording earthquakes in Australia’s most active seismic zone: *Seismological Research Letters*, v. 94, p. 999–1011, doi:10.1785/0220220323.
- Moghadasi, N. and Shabani, E 2022, Impact of distribution of seismic ambient noise sources on surface wave characteristics: *Iranian Journal of Geophysics*, v. 15, no. 4, p. 1–14.
- Murdie, R, Pickle, R., Yuan, H, Love, D, Dent, V, Miller, M Whitney, J 2022, Observations from the 2022 Arthur River, Western Australia, Earthquake Swarm, in 2022 National Conference proceedings; Australian Earthquake Engineering Society, National Conference, Mount Macedon, Victoria, 24–25 November.
- Murdie, R, Gessner, K, Miller, M, Salmon, M, Yuan, H, Whitney, J, Gray, S and Allen, T 2020, Geological Survey of Western Australia: SWAN takes off – a new seismic monitoring project in Western Australia: Preview, v. 208, p. 28–29, doi:10.1080/14432471.2020.1828423.
- Nakamura, Y 1989, A method for dynamic characteristics estimation of subsurface using microtremor on the ground surface: *Railway Technical Research Institute, Quarterly Reports*, v. 30, no. 1, p. 25–33.
- Nakamura, Y 2000, January. Clear identification of fundamental idea of Nakamura’s technique and its applications, in *Proceedings of the 12th world conference on earthquake engineering*, v. 2656, p. 1–8.
- Nakamura, Y 2019, What is the Nakamura method?: *Seismological Research Letters*, v. 90, no. 4, p. 1437–1443.
- National Earthquake Hazards Reduction Program (US) and Building Seismic Safety Council (US), 2001, NEHRP Recommended Provisions (National Earthquake Hazards Reduction Program) for Seismic Regulations for New Buildings and Other Structures: Building Seismic Safety Council, <https://www.fema.gov/node/nehnp-recommended-seismic-provisions-new-buildings-and-other-structures>.
- Poggi, V and Fäh, D 2010, Estimating Rayleigh wave particle motions from three-component array analysis of ambient vibrations: *Geophysical Journal International*, v. 180, p. 251–267.
- Sambridge, M, 1999a, Geophysical inversion with a neighbourhood algorithm – I. Searching a parameter space: *Geophysical Journal International*, v. 138, p. 479–494.
- Sambridge, M, 1999b, Geophysical inversion with a neighbourhood algorithm – II. Appraising the ensemble: *Geophysical Journal International*, v. 138, p. 727–746.
- Standards Australia 2007, AS 1170.4—2007 Structural design actions, Part 4: Earthquake actions in Australia: Standards Australia, Sydney, New South Wales, <www.standards.org.au/standards-catalogue/standard-details?designation=AS-1170-4-2007-Amd-2-2018>.
- Standards Australia 2018, AS 3600:2018 Concrete structures: Standards Australia, Sydney, New South Wales, <www.standards.org.au/standards-catalogue/standard-details?designation=as-3600-2018>.
- Standen, S Dentith, M and Clark, D 2021, A geophysical investigation of the 2018 Lake Muir earthquake sequence: reactivated Precambrian structures controlling modern seismicity: *Australian Journal of Earth Sciences*, v. 68, no. 5, p. 717–730, doi:10.1080/08120099.2021.1848924.
- Vantassel, JP and Cox, BR 2021, SWinvert: a workflow for performing rigorous 1-D surface wave inversions: *Geophysical Journal International*, v. 224, no. 2, p. 1141–1156.
- Vogfjörð, KS and Langston, CA 1987, The Meckering earthquake of 14 October 1968: a possible downward propagating rupture: *Bulletin of the Seismological Society of America*, v. 77, p. 1558–1578, doi:10.1785/bssa0770051558.
- Wald, DJ and Allen, TI 2007, Topographic slope as a proxy for seismic site conditions and amplification: *Bulletin of the Seismological Society of America*, v. 97, p. 1379–1395.
- Wathelet, M 2005, Array recordings of ambient vibrations: surface-wave inversion: PhD dissertation, Liège University, 177p.
- Wathelet, M 2008, An improved neighborhood algorithm: parameter conditions and dynamic scaling: *Geophysical Research Letters* v. 35, L09301, doi:10.1029/2008GL033256.
- Wathelet, M, Guillier, B, Roux, P, Cornou, C and Ohrnberger, M 2018, Rayleigh wave three-component beamforming: Signed ellipticity assessment from high-resolution frequency-wavenumber processing of ambient vibration arrays: *Geophysical Journal International*, v. 215, no. 1, p. 507–523, doi:10.1093/gji/gyg286.
- Zhao, JX, Irikura, K, Zhang, J, Fukushima, Y, Somerville, PG, Asano, A, Ohno, Y, Oouchi, T, Takahashi, T and Ogawa, H 2006, An empirical site-classification method for strong-motion stations in Japan using H/V response spectral ratio: *Bulletin of the Seismological Society of America*, v. 96, no. 3, p. 914–925.

An updated Fourier spectral attenuation model for southwestern Western Australia

TI Allen¹

1. Geoscience Australia, Symonston ACT 2609

Abstract

Earthquake ground motion data recorded on the South West Australia (seismic) Network (SWAN) are augmented to existing ground motion datasets for the southwest Western Australian region to develop an updated Fourier spectral amplitude attenuation model for the region. The model is applicable for the moment-magnitude range of $2.5 \leq M_w < 5.3$, hypocentral distances less than 500 km, and for 150 logarithmically spaced frequencies from $0.1 \leq f < 36$ Hz. The data collected through the SWAN improves the constraint on the near-source attenuation of Fourier spectral amplitudes and will enable improved characterization of earthquake sources. Site-specific amplification effects are evaluated, and these will be used in concert with measurements of the seismic site properties to develop models reference seismic site classes. Stochastic simulations using the Fourier attenuation model will be used in the future to improve ground motion models for large-magnitude earthquakes that are applied in probabilistic seismic hazard analyses for the region.

KEYWORDS: attenuation, earthquakes, earthquake magnitude, natural hazards, seismicity

Lay abstract

Earthquake ground motion data recorded on the South West Australia (seismic) Network (SWAN) are used to develop a model to estimate how an earthquake's energy attenuates as it propagates through the Earth's crust. This model will be used to simulate the ground motions of large-magnitude earthquakes that could affect the built environment and cause societal harm. This information will inform national and site-specific earthquake hazard assessments. These assessments are important across a broad range of policy and regulatory settings, and contribute to engineering design practice, risk modelling, insurance underwriting, community safety and resilience planning.

Introduction

The Southwest Seismic Zone (SWSZ) in southwestern Western Australia is characterized by some of the highest rates of earthquake activity in Australia; consequently, it is rated among the highest hazard regions in the continent (Allen et al., 2020, 2023). Furthermore, of the nine surface rupturing earthquakes to have been documented in Australia, five have occurred within the SWSZ (Clark et al., 2020). The SWSZ lies fully within the Archean Yilgarn Craton, which is characterized by metavolcanic and metasedimentary rocks, granites and granitic gneiss that formed principally between c. 3.73 and 2.62 Ga (Nutman et al., 1991; Cassidy et al., 2006). Despite the high rates of earthquake activity, information on the attenuation of seismic-wave energy through the Yilgarn Craton that is of use for seismic hazard applications is limited. Allen et al. (2006) developed a model of Fourier spectral attenuation using data from the 2001–02 Burakin earthquake sequence (Leonard, 2002). A recent study of Wei et al. (2017) has also modelled the L_g -wave attenuation characteristics on a national scale. However, this model has limited applicability for near-source attenuation effects, which are of primary importance to seismic hazard.

Earthquake hazard studies (e.g. Allen et al., 2020; 2023) rely on the use of models that forecast the likely ground motion amplitudes for a given earthquake magnitude, source–receiver distance and site condition. These ground motion models (GMM) are characterized for a range of ground motion intensity measures, including peak ground acceleration (PGA), peak ground velocity (PGV) and 5%-damped response spectral accelerations for a range of vibratory periods (e.g. Chopra, 2007). In active tectonic regions, there are often sufficient empirical data with which to develop these GMMs (e.g. Bozorgnia et al., 2014). However, in stable continental regions such as Australia, the development of these GMMs relies on characterizing the source and attenuation properties of small-magnitude earthquakes, and applying these seismological models to simulate ground motions for larger-magnitude events (e.g. Somerville et al., 2009; Allen, 2012; Bayless et al., 2023).

In Australia, earthquake ground motions are now recorded by several permanent and temporary monitoring networks at regional and local scales across the continent. The backbone of the national monitoring system is the Australian National

Seismograph Network (ANSN; Geoscience Australia, 2021); a network of over 100 independent (i.e. not including small-aperture arrays) seismic stations across Australia, islands in the Pacific, Southern and Indian Oceans, and the Australian Antarctic Territory. The seismic data collected by the ANSN are complemented by data from the Australian Seismometers in Schools (AuSIS) seismic network (Balfour et al., 2014; Salmon et al., 2022). Recent enhancements in permanent monitoring networks, together with chance observations by temporary monitoring networks (e.g. Saygin and Lumley, 2018; Murdie et al., 2022b; Miller et al., 2023), have allowed for the augmentation of ground motion datasets of use for improved attenuation models for southwest Western Australia.

This study augments existing ground motion data (Ghasemi and Allen, 2021) with new data collected through the South West Australia (seismic) Network (SWAN; Miller et al., 2023) to develop an updated Fourier spectral attenuation model for southwest Western Australia.

Event selection and source parameters

To obtain a list of candidate earthquakes from which to assess digital waveform data recorded since 1990, a combination of earthquake magnitude and distance from the closest seismograph station likely to have recorded the earthquake was used (Table 8). The magnitude–distance criteria used are defined in Allen et al. (2024), with a maximum distance of 500 km applied in the data compilation for this study. Additionally, data for all earthquakes of M_L 2.95 and above have been extracted for the period of the SWAN deployment (Pickle et al., 2024).

Earthquake source parameters (i.e. locations and magnitudes) have largely been taken from existing national catalogues, summarized in the documentation for the 2018 National Seismic Hazard Assessment earthquake catalogue (Allen et al., 2018). To date, some earthquake locations determined using aftershock deployments have not been translated to the official Geoscience Australia catalogue and these locations supplant Geoscience Australia parameters where appropriate. Specifically, these include data from the 2001–02 Burakin (Allen et al., 2006) and 2016 Norseman, Western Australia, earthquake sequences. Special studies that have carefully relocated some earthquakes have also been considered as preferred parameters (e.g. Clark et al., 2020; Dent and Collins, 2020). Epicentres from earthquakes during the SWAN deployment are taken from Pickle et al. (2024).

The preferred magnitude type for calibrating seismological models based on Fourier spectra is moment magnitude, M_W . Moment magnitudes are not calculated in routine observational practice in Australia; often, magnitude conversions must be applied (e.g. Allen et al., 2018, 2023). Where available,

Table 8 Distance to nearest seismometer required for event selection

Magnitude range*	Minimum site distance (km)
$M \geq 4.25$	n/a
$4.0 \leq M < 4.25$	150
$3.75 \leq M < 4.0$	100
$3.5 \leq M < 3.75$	50
$3.0 \leq M < 3.5$	20

M_W estimates for earthquakes in the current dataset are taken from Allen (2024, unpublished data). Otherwise, they are taken from the present study, to be described in the **Magnitude term** section. Figure 57 shows the magnitude–distance distribution of the dataset used to develop the Fourier attenuation model in the present study. Considering the selected earthquakes located within the SWAN array of magnitude M_L 2.95 and greater (Pickle et al., 2024), 911 additional high-quality ground motion recordings augment the 1585 recordings available from existing temporary-deployment datasets and permanent monitoring networks¹. This represents a more than 50% increase in data than would have been available without the SWAN deployment.

1 Data count based on recordings with a minimum signal-to-noise ratio of 4.0 at a frequency of 2 Hz.

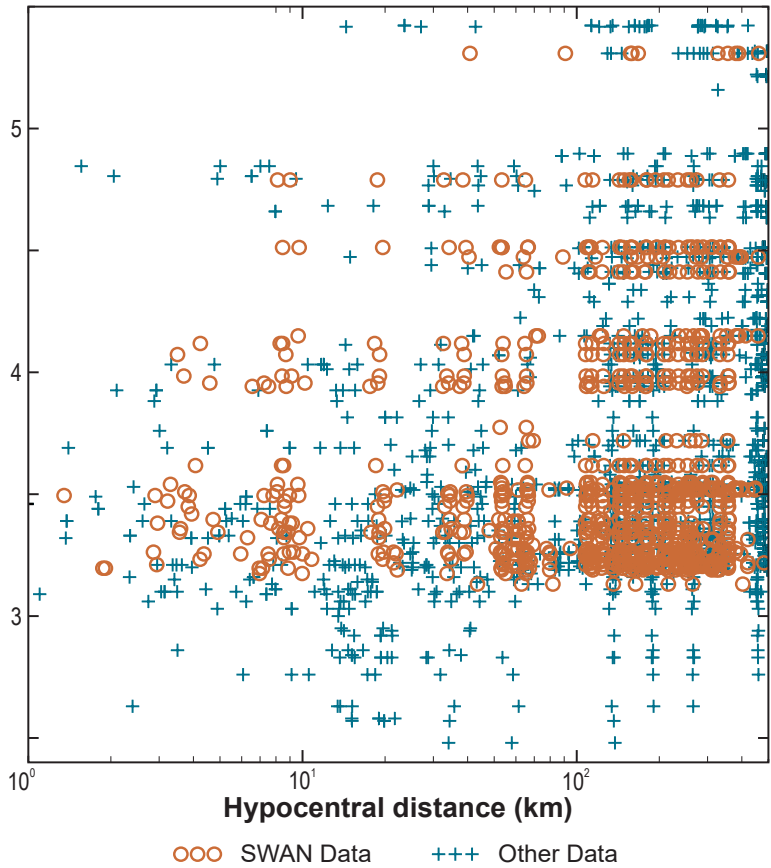


Figure 57. Magnitude–hypocentral distance distribution of the SWWA dataset. The SWAN data (Miller et al., 2023) is shown to augment existing datasets for the region

Data processing

The vertical-component noise spectra were determined from the pre-event recordings using at least two minutes of continuous data (exceptions were made for high-quality triggered data with little pre-event data). The vertical-component event data are taken from the start of the S-phase and included the *Lg*-phase. The end times for signal analysis were manually picked to exclude large-amplitude *Rg* phases generated from shallow-focus events (e.g. Kafka, 1990), which are common in earthquakes in the southwest Western Australia region (e.g. Allen et al., 2006; Somerville et al., 2009). Both the signal and noise spectral data were smoothed and resampled to 150 frequencies logarithmically spaced from 0.1 to 36 Hz. Vertical-component Fourier amplitude spectra were then screened by applying a minimum signal-to-noise ratio of 4.0. Frequency-specific data below this value were excluded from further analysis.

Model regression

The attenuation of ground motion is often characterized in the Fourier spectral domain. In practice, the observed shear-wave displacement amplitude spectrum, $Y(M_w, R, f)$, for a magnitude M_w , hypocentral distance R and frequency f can be generalized as the convolution of several factors: the earthquake point-source spectrum; the propagation path that incorporates both geometrical and anelastic attenuation; and path-independent site effects such that:

$$\log_{10} Y(M_w, R, f) = F_M(M_w, f) + F_P(R, f) + F_S(f) \quad (1)$$

where Y represents the median Fourier displacement spectral intensity measure for frequency f , F_M is the magnitude-scaling term, F_P is the path-scaling term, and F_S is the site term. In this study, the available data (Y) are regressed to determine F_P and F_S , with the aim of resolving F_M . The following sections describe the mixed-effects regression for these terms. The coefficients for the model are available at the link to data and models provided in the **Introduction** of this Report.

Path term

Within-event Fourier amplitude data are grouped into 0.1 log-spaced hypocentral distance bins and the event term, $F_M(M_w, f)$, is removed by normalizing the data using the average amplitude determined from the distance bin with a median distance of 200 km (i.e. $178 \leq R < 224$ km). All normalized data for each event were stacked (for a given frequency) to determine the average attenuation for the propagation path, $F_P(R, f)$.

The piecewise functional form of the attenuation model is given by:

$$F_P(R, f) = c_0 \cdot \log_{10}(R_h) \text{ for } R \leq R_1 \text{ km} \quad (2a)$$

$$F_P(R, f) = c_0 \cdot \log_{10}(R_h) + c_1 \cdot (R - R_1) \text{ for } R > R_1 \text{ km} \quad (2b)$$

Where c_0 to c_1 are parameters to be determined through regression, $R_1 = 60$ km, and:

$$R_h = \sqrt{R^2 + R_{ref}^2} \text{ for } R \leq R_1 \text{ km} \quad (3a)$$

$$R_h = \sqrt{R_1^2 + R_{ref}^2} \text{ for } R > R_1 \text{ km} \quad (3b)$$

where R_{ref} is the reference distance for the near-source saturation of ground motion assigned as 5 km. Figure 58 shows the fits to normalised Fourier spectral data for 2.0 and 5.0 Hz respectively.

Site term

With the determination of the average path parameters, the site terms F_S for each station j could then be resolved. This was done in two stages.

1. A regional high-frequency model parameter, κ_0 (e.g. Ktenidou et al., 2014), was determined such that average source spectra modelled the Brune (1970) ω^{-2} source spectrum. The median value of κ_0 across all stations in southwest Western Australia, relative to the F_P parameter, is estimated to be -0.062 . Representative station-specific examples are shown in Figure 59.

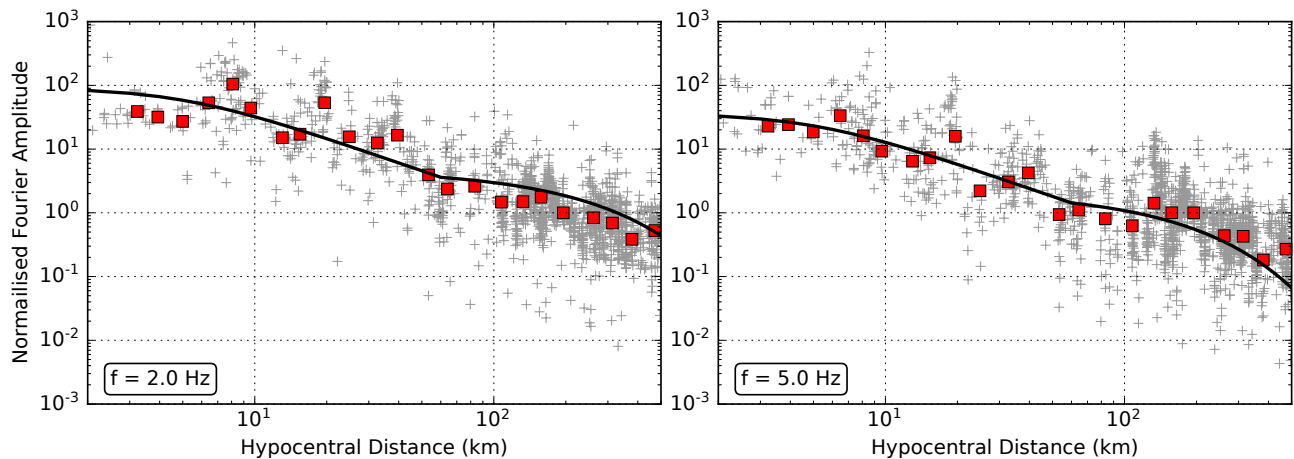


Figure 58. Example fit to normalized Fourier spectral amplitude data for 2.0 and 5.0 Hz respectively. Red squares indicate median values binned in 0.1 log-space distance bins

2. The path- and κ_0 -corrected spectra for each station j were averaged to determine the source spectrum for each event i . These average source spectra were fitted by the theoretical Brune (1970) ω^{-2} source spectrum and the misfit of each station's spectra to this theoretical spectrum was recorded such that a station-specific frequency-dependent site term was derived.

The full site term is thus defined by:

$$F_s(f) = -\pi f \kappa_0 + S_j(f) \quad (4)$$

where $S_j(f)$ is the frequency-dependent term for site j . Figure 60 shows some $S_j(f)$ correction terms for representative sites. Some stations demonstrated pronounced site resonance effects and, without careful review, these stations could potentially bias the characterization of earthquake source parameters, including earthquake magnitude.

Magnitude term

To determine the magnitude-scaling term, M_W for each event on the dataset must first be assigned or calculated. Moment-magnitude estimates determined from national-

scale assessments (Allen, 2024, unpublished data) are preferred. However, for many events within the current dataset, there are no corresponding estimates of M_W in Allen (2024, unpublished data). Armed with the path- and site-correction terms, data are source-corrected. The mean source spectrum for each event i is then fitted with the theoretical Brune (1970) ω^{-2} source model, which enables the estimation of seismic moment, M_0 , and M_W (e.g. Allen, 2012). The source-corrected Fourier amplitude spectra could then be regressed against M_W . As no magnitude saturation was identified in the magnitude and frequency range of interest, given the small-to-moderate-sized earthquakes considered here, the magnitude-scaling term could be approximated by a simple linear regression, such that:

$$F_M(f) = m_0 \times M_W + m_1 \quad (5)$$

where m_0 and m_1 are frequency-dependent coefficients to be regressed. Some stations demonstrated significant frequency-dependent site effects, and these may have affected the estimation of earthquake magnitudes as determined in this study. This aspect of this study thus requires further investigation.

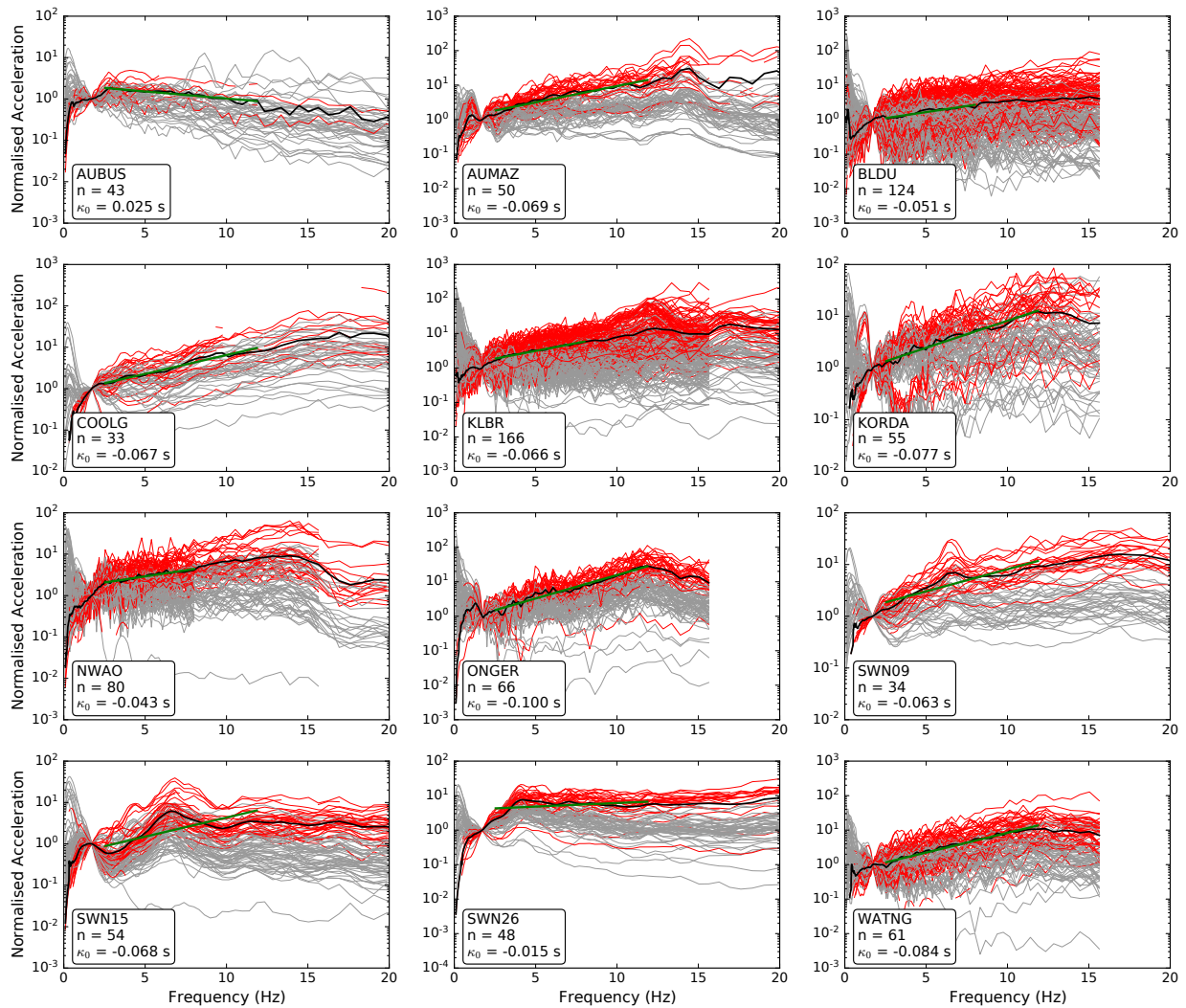


Figure 59. Fourier acceleration spectra passing signal-to-noise tests, corrected for path effects and normalized at 2.0 Hz (thin red lines) for selected stations. Stacked spectra are regressed between 4.0 and 12.0 Hz to model the high-frequency site effect, κ_0 proportional to the gradient of the acceleration spectrum (thick green line). Spectra that do not pass signal-to-noise tests are plotted as thin grey lines. The number of recordings used and site-specific κ_0 values are indicated. Note, a shorter regression window of 4.0 to 8.0 Hz is used where lower sample rate data are present

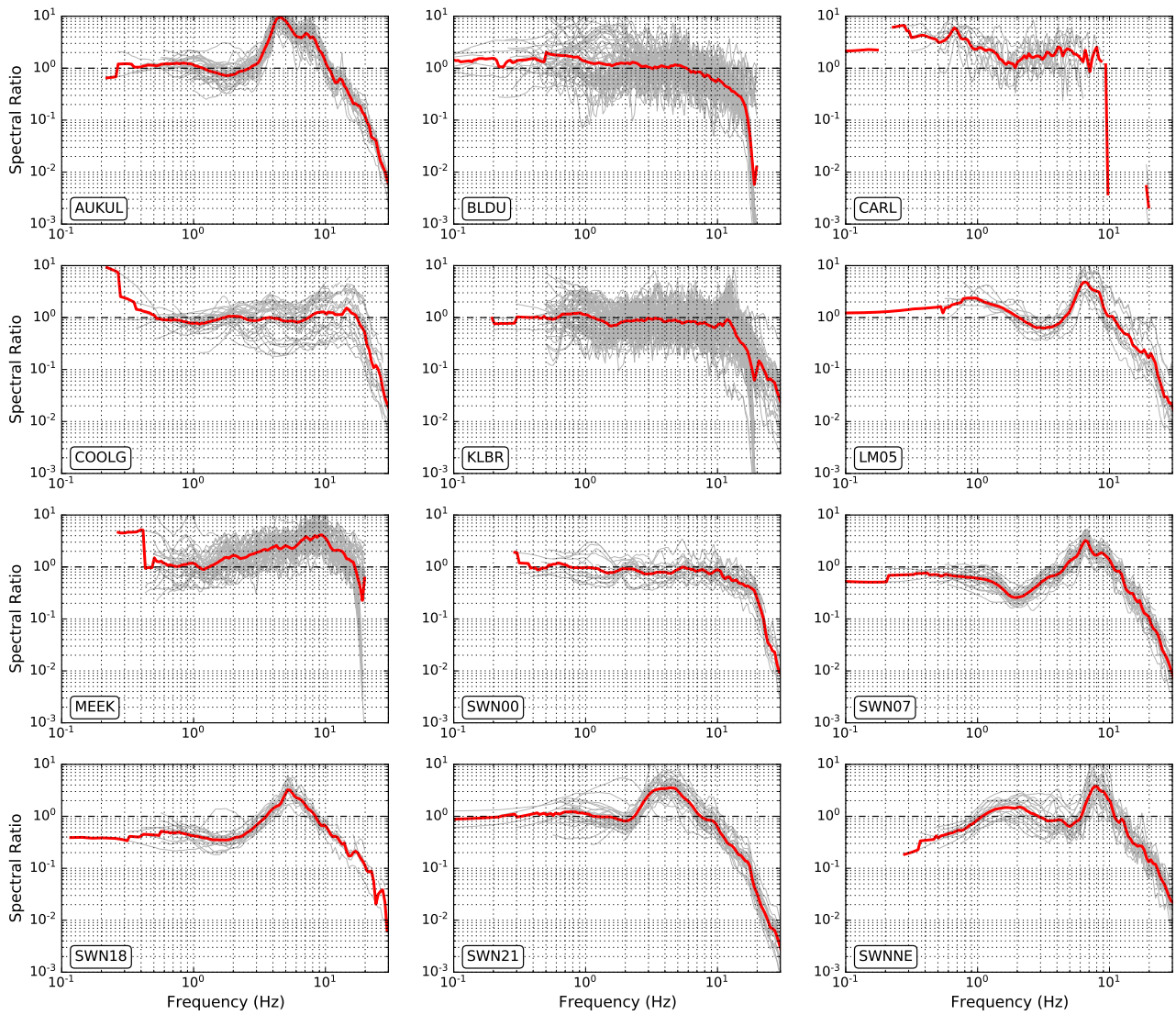


Figure 60. Frequency-dependent site-correction terms for representative stations. Heavy red line is the mean site correction $S(f)$ calculated from the individual recording misfits (thin grey lines) from the Brune (1970) ω^{-2} source spectrum. The thin dashed line is equivalent to a ratio of 1.0

Model residuals

With the evaluation of the magnitude, path and site terms, a value of $\log Y(M_w, R, f)$ can be estimated for magnitude–distance couples equivalent to each observation, and the model residuals can subsequently be calculated. Figure 61 shows the model residuals for 2.0 and 5.0 Hz. Although there are some systematic patterns present in these residuals, this preliminary model generally appears to be unbiased with distance assuming the simplified functional form.

Comparison of Fourier attenuation models

It is useful to now compare the Fourier amplitude attenuation model with previous models developed for Australia, together with models for other stable continental regions. Figure 62 compares the attenuation of Fourier displacement amplitudes for an earthquake of M_w 5.0 for 0.5 and 5.0 Hz from this study with the attenuation models of: Allen et al. (2006) developed from the 2001–02 Burakin

earthquake sequence data; Allen et al. (2007) developed using southeastern Australian data; and Atkinson (2004a,b) for eastern North America (ENA). At low frequencies, the present study is similar to previous studies in Australia, particularly the study that used the Burakin earthquake sequence data. This should be expected since this study augments the Burakin dataset and considers an almost identical geographical and geological terrane. It should also be expected that low-frequency spectral models may be similar in the near-source region (i.e. $R < 100$ km), given that an earthquake's magnitude is defined by these low-frequency amplitudes.

The current study also includes a near-field saturation term, which reduces spectral amplitudes in the near-field relative to other models at very short distances (e.g. $R < 10$ km). The lower spectral amplitudes at higher frequencies relative to the other models suggests that events in the southwest Western Australia region possess low stress drops relative to earthquakes in eastern Australia, as noted previously (Allen et al., 2004, 2007; Miller et al., 2023). The ENA model of Atkinson (2004a,b) shows consistently larger spectral amplitudes over all distances and frequencies.

The low-frequency comparison of the ENA model with the Australian models does begin to converge when smaller magnitudes are used. This suggests a potential inconsistency between the empirical magnitude scaling developed in these respective studies.

Discussion and conclusions

Data collected through the SWAN deployment (Murdie et al., 2020; Miller et al., 2023) augment existing ground motion datasets for the southwest Western Australia region (Ghasemi and Allen, 2021). Considering earthquakes located within the SWAN of magnitude M_L 2.95 and greater (Pickle et al., 2024), 911 additional high-quality ground motion recordings have been gathered, in addition to the 1585 data from existing temporary datasets and permanent monitoring networks for the region. It should be noted that including events smaller than M_L 2.95 recorded within the SWAN would further increase the number of records. Nevertheless,

the SWAN dataset spans a wide magnitude range and has benefited from the occurrence of several moderate-sized earthquakes within the network during its deployment (e.g. Murdie et al., 2022a).

The combined dataset has enabled a more holistic assessment of near-source Fourier spectral attenuation for the southwest Western Australia region and improves on the study of Allen et al. (2006), which relied only on data recorded during the 2001–02 Burakin earthquake sequence. The model excludes the effects of large-amplitude R_g phases – largely considered a path effect for shallow-focus earthquakes – so that the attenuation of body waves could be prioritized for seismic source characterization. Seismic hazard assessments consider all ground shaking effects, irrespective of how the seismic energy is propagated from the source. Consequently, these R_g -phase effects will need to be reconsidered in any ground motion model used for forecasting seismic hazard (e.g. Somerville et al., 2009).

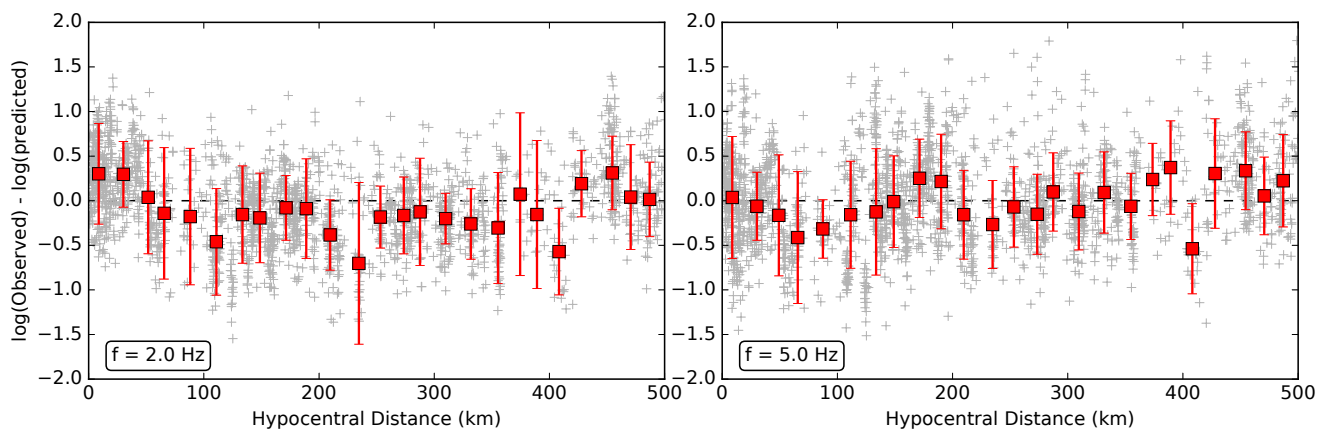


Figure 61. Logarithm (base 10) of residuals (observed – predicted) for 2.0 and 5.0 Hz, respectively, for the assembled dataset of southwest Western Australia earthquakes. Grey crosses indicate residuals for each individual observation. Red squares are mean and standard deviation of the residuals windowed in 20-km bins

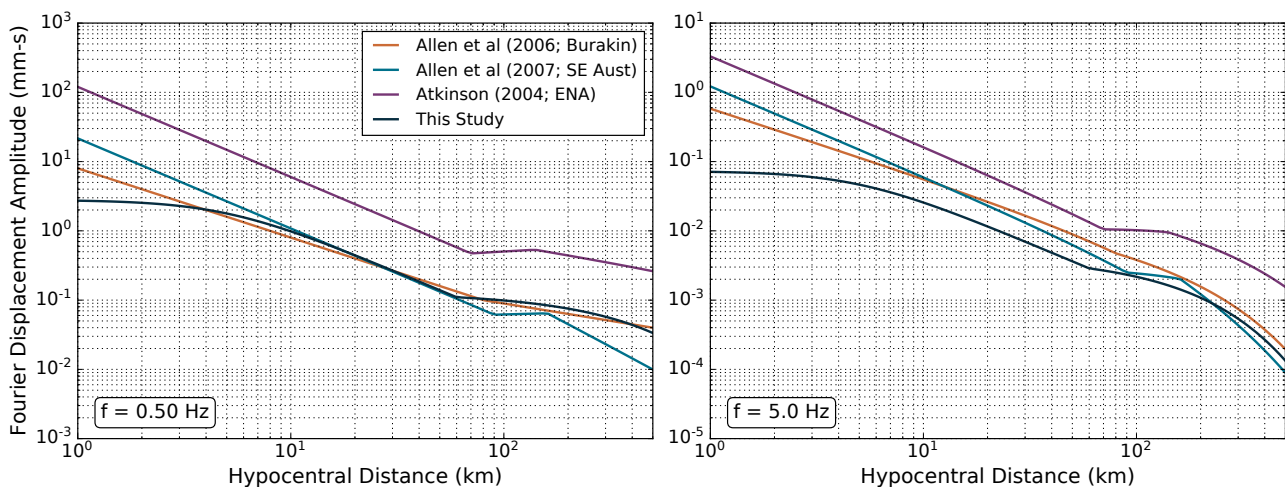


Figure 62. Comparison of Fourier displacement amplitude models for 0.50 and 5.0 Hz. The subplots compare empirical models developed from the Burakin dataset (Allen et al., 2006) for an earthquake of M_w 5.0, as well as models for southeastern Australia (Allen et al., 2007) and eastern North America (Atkinson, 2004a,b)

As noted in the **Site term** section, some stations demonstrated pronounced site-response effects and, without careful review, these stations will bias the characterization of earthquake source parameters, including magnitude. This initial study has treated all data uniformly and has not excluded data from the computation of earthquake source parameters. Consequently, the results of Ebrahimi and Allen (2024), which characterize the seismic site condition for the SWAN sites, will be critical to provide an attenuation model that is calibrated to a reference site condition appropriate to the southwest Western Australia. This will improve the accuracy of estimates for seismic-source parameter using this dataset. Furthermore, these site characterization data will inform how earthquake ground motions may be modified as the energy transitions from the Yilgarn Craton into the high-exposure Perth Basin.

Additional seismic stations being installed in Western Australia, including the WA Array (Murdie et al., 2024), will provide further data that can be used to characterize the attenuation of Fourier spectral amplitudes in southwest Western Australia. Ultimately, these attenuation models will be used to underpin ground motion simulations for large-magnitude earthquakes in order to develop new, regionally-specific response spectral ground motion models that can be used in probabilistic seismic hazard studies.

Acknowledgements

The author is grateful to the collaborators involved in the SWAN project, in particular, Meghan Miller, Ruth Murdie, Robert Pickle and Huaiyu Yuan, who led the data collection and management. Robert Pickle is especially thanked for providing a copy of his new earthquake catalogue (Pickle et al., 2024) in advance of the publication of this Report. The author thanks Reza Ebrahimi, Klaus Gessner, Hadi Ghasemi and Thuany Costa de Lima for their respective reviews of this chapter. Finally, the author publishes with the permission of the Chief Executive Officer of Geoscience Australia.

References

- Allen, TI 2012, Stochastic ground-motion prediction equations for southeastern Australian earthquakes using updated source and attenuation parameters: *Geoscience Australia Record* 2012/69, Canberra, 55p.
- Allen, TI, Cummins, PR, Dhu, T and Schneider, JF 2007, Attenuation of ground-motion spectral amplitudes in southeastern Australia: *Bulletin of the Seismological Association of America*, v. 97, p. 1279–1292, doi:10.1785/0120060172.
- Allen, TI, Cummins, PR, Leonard, M and Collins, C 2004, Low stress drop swarm events in the Yilgarn Craton, Western Australia: AGU Fall Meeting, San Francisco, California.
- Allen, TI, Dhu, T, Cummins, PR and Schneider, JF 2006, Empirical attenuation of ground-motion spectral amplitudes in southwestern Western Australia: *Bulletin of the Seismological Association of America*, v. 96, p. 572–585, doi:10.1785/0120040238.
- Allen, TI, Ghasemi, H and Ebrahimi, R 2024, Seismology down under: developing engineering ground-motion databases in regions of low seismicity and sparse monitoring networks: 18th World Conference on Earthquake Engineering, Milan, Italy.
- Allen, TI, Griffin, JD, Clark, DJ, Cummins, PR, Ghasemi, H and Ebrahimi, R 2023, The 2023 National Seismic Hazard Assessment for Australia: model overview: *Geoscience Australia, Record* 2023/53, 152p., doi:10.26186/148969.
- Allen, TI, Griffin, JD, Leonard, M, Clark, DJ and Ghasemi, H 2020, The 2018 National Seismic Hazard Assessment of Australia: quantifying hazard changes and model uncertainties: *Earthquake Spectra*, v. 36, p. 5–43, doi:10.1177/8755293019900777.
- Allen, TI, Leonard, M, Ghasemi, H and Gibson, G 2018, The 2018 National Seismic Hazard Assessment for Australia: earthquake epicentre catalogue: *Geoscience Australia, Record* 2018/30, Canberra, 51p., doi:10.11636/Record.2018.030.
- Atkinson, GM 2004a, Empirical attenuation of ground-motion spectral amplitudes in southeastern Canada and the northeastern United States: *Bulletin of the Seismological Association of America*, v. 94, p. 1079–1095, doi:10.1785/0120030175.
- Atkinson, GM 2004b, Erratum - Empirical attenuation of ground-motion spectral amplitudes in southeastern Canada and the northeastern United States: *Bulletin of the Seismological Association of America*, v. 94, p. 1079–1095.
- Balfour, NJ, Salmon, M and Sambridge, M 2014, The Australian Seismometers in Schools Network: education, outreach, research, and monitoring: *Seismological Research Letters*, v. 85, p. 1063–1068, doi:10.1785/0220140025.
- Bayless, J, Somerville, P, Thio, HK and Ramos-Sepúlveda, ME 2023, Updates to the Somerville et al. (2009) ground motion model for Australia using broadband ground-motion simulations: Australian Earthquake Engineering Society 2023 Conference, Brisbane, Queensland.
- Bozorgnia, Y, Abrahamson, NA, Al Atik, L, Ancheta, TD, Atkinson, GM, Baker, JW, Baltay, A, Boore, DM, Campbell, KW, Chiou, BS-J, Darragh, R, Day, S, Donahue, J, Graves, RW, Gregor, N, Hanks, T, Idriss, IM, Kamai, R, Kishida, T, Kottke, A, Mahin, SA, Rezaeian, S, Rowshandel, B, Seyhan, E, Shahi, S, Shantz, T, Silva, W, Spudich, P, Stewart, JP, Watson-Lamprey, J, Wooddell, K and Youngs, R 2014, NGA-West2 research project: *Earthquake Spectra*, v. 30, p. 973–987, doi:10.1193/072113EQS209M.
- Brune, JN 1970, Tectonic stress and the spectra of seismic shear waves from earthquakes: *Journal of Geophysical Research*, v. 75, p. 4997–5009, doi:10.1029/JB075i026p04997.
- Cassidy, KF, Champion, DC, Krapež, B, Barley, ME, Brown, SJA, Blewett, RS, Groenewald, PB and Tyler, IM 2006, A revised geological framework for the Yilgarn Craton, Western Australia: *Geological Survey of Western Australia, Record* 2006/8, 8p.
- Chopra, AK 2007, Elastic response spectrum: a historical note, *Earthquake Engineering & Structural Dynamics*, v. 36, p. 3–12, doi:10.1002/eqe.609.
- Clark, DJ, Brennand, S, Brenn, G, Garthwaite, MC, Dimech, J, Allen, TI and Standen, S 2020, Surface deformation relating to the 2018 Lake Muir earthquake sequence, southwest Western Australia: new insight into stable continental region earthquakes: *Solid Earth*, v. 11, p. 691–717, doi:10.5194/se-11-691-2020.
- Dent, VF and Collins, CDN 2020, The extent of the epicentral zone for events associated with two M_L 5 events in March 2002 near Burakin, Western Australia – a review of field and epicentral data: Australian Earthquake Engineering Society 2020, Virtual Conference.
- Ebrahimi, R and Allen, TI 2024, Site classification and V_{s30} determination for seismic hazard evaluation in the SWAN seismic network, Western Australia, in *South West Australia Network (SWAN): passive seismic imaging and hazard analysis compiled by RE Murdie and MS Miller*: Geological Survey of Western Australia, Report 255, p. 58–67.
- Geoscience Australia 2021, Australian National Seismograph Network Data Collection (Version 2.0, September 2018): Commonwealth of Australia (Geoscience Australia), doi:10.26186/144675.
- Ghasemi, H and Allen, T 2021, Engineering ground-motion database for western and central Australia: Australian Earthquake Engineering Society 2021, Virtual Conference.
- Kafka, AL 1990, R_g as a depth discriminant for earthquakes and explosions: a case study in New England: *Bulletin of the Seismological Association of America*, v. 80, p. 373–394.

- Ktenidou, O-J, Cotton, F, Abrahamson, NA and Anderson, JG 2014, Taxonomy of κ : a review of definitions and estimation approaches targeted to applications: *Seismological Research Letters*, v. 85, p. 135–146, doi:10.1785/0220130027.
- Leonard, M 2002, The Burakin WA earthquake sequence Sept 2000 – June 2002: Australian Earthquake Engineering Society 2002 Conference, Adelaide, South Australia.
- Miller, MS, Pickle, R, Murdie, R, Yuan, H, Allen, TI, Gessner, K, Kennett, BLN and Whitney, J 2023, Southwest Australia Seismic Network (SWAN): recording earthquakes in Australia's most active seismic zone: *Seismological Research Letters*, v. 94, p. 999–1011, doi:10.1785/0220220323.
- Murdie, R, Gessner, K, Miller, M, Salmon, M, Yuan, H, Whitney, J, Gray, S and Allen, T 2020, SWAN takes off – a new seismic monitoring project in Western Australia: *Preview*, v. 208, p. 28–29, doi:10.1080/14432471.2020.1828423.
- Murdie, R, Yuan, H, Miller, MS, Pickle, R, Salmon, M and Whitney, J 2022a, Rapid deployment for earthquake aftershock monitoring in southwest Western Australia – the Arthur River swarm 2022: *Preview*, v. 217, p. 39–41, doi:10.1080/14432471.2022.2057678.
- Murdie, R, Yuan, H and O'Donnell, JP 2022b, WA-Array takes off, Australian Earthquake Engineering Society 2022 Conference, Mount Macedon, Victoria.
- Murdie, RE, Yuan, H, O'Donnell, JP, Johnson, SP, Ebrahimi, R and Rashidifard, M 2024, WA Array: a high-resolution passive-source seismic survey to image the west Australian lithosphere: *Seismological Research Letters*, v. 95, p. 3093–3108, doi:10.1785/0220230415.
- Nutman, AP, Kinny, PD, Compston, W and Williams, IS 1991, SHRIMP U–Pb zircon geochronology of the Narryer Gneiss Complex, Western Australia: *Precambrian Research*, v. 52, p. 275–300, doi:10.1016/0301-9268(91)90084-N.
- Pickle, R, Miller, MS, Murdie, RE and Allen, TI 2024, A detailed earthquake catalogue for southwest Australia 2020–23 using data from the SWAN and WA Array networks, in *South West Australia Network (SWAN): passive seismic imaging and hazard analysis compiled by RE Murdie and MS Miller*: Geological Survey of Western Australia, Report 255, p. 22–29.
- Salmon, M, Mousavi, S and Sambridge, M 2022, 10 years of Australian Seismometers in Schools – education, outreach and research: Australian Earthquake Engineering Society 2022 National Conference, Mount Macedon, Victoria.
- Saygin, E and Lumley, D 2018, Passive seismic investigations at the SW Hub: University of Western Australia Australian National Low Emissions Council (ANLEC) R&D Project Number 7-0215-0244, Perth, Western Australia.
- Somerville, P, Graves, R, Collins, N, Song, S-G, Ni, S and Cummins, P 2009, Source and ground motion models for Australian earthquakes: Australian Earthquake Engineering Society 2009 Conference, Newcastle, New South Wales.
- Wei, Z, Kennett, BLN, and Zhao, L-F 2017, Lg-wave attenuation in the Australian crust: *Tectonophysics*, v. 717, p. 413–424, doi:10.1016/j.tecto.2017.08.022.

The importance of contemporary earthquake knowledge to inform emergency management

M Zanini¹ and A Brannigan¹

1. Department of Fire and Emergency Services, Western Australia

Abstract

Effective management of emergencies requires a sound understanding of hazards and the risks they pose. This is especially the case for those that can cause widespread, almost instantaneous impacts to life, property and critical infrastructure.

Given the frequency of earthquakes in Western Australia, it is important to enhance the knowledge of seismic hazard and better understand potential exposures and vulnerabilities to ground shaking events. The deployment of seismic stations across Western Australia's southwest, as part of the SWAN project, has enhanced knowledge and awareness of earthquake risk, while contributing to emergency manager and community focused guidance to improve our state's management of this hazard.

KEYWORDS: earthquake risk, emergency management, hazard management

Developing a baseline understanding of seismic risk in Western Australia

Unlike other natural hazards, earthquakes cannot be predicted, do not have a season, often occur without warning and may occur as a single event or in a sequence of several events. Large earthquakes are infrequent but potentially catastrophic, with immediate and lasting effects to people and the built environment. The 'Western Australia's Natural Hazards Risk Profile 2017' (SEMC, 2017a) identified that, of all the hazards considered, earthquakes pose some of the highest risks to Western Australia's built environment, and the 'Metropolitan Emergency Management Districts Risk Assessment Report' (SEMC, 2017b) determined that earthquakes have the highest overall risk for the Perth region. With the Department of Fire and Emergency Services (DFES) having responsibilities for the management of the adverse effects of an earthquake emergency across the prevention, preparedness, response and recovery spectrum, contemporary knowledge of seismic hazard is required to effectively manage this phenomenon.

Southwest Western Australia has been the most seismically active region in continental Australia over the last five decades and has over 90% of the state's population. The region has hosted moderate earthquakes (Clarke et al., 2020), significant earthquake swarms (Leonard, 2002; Murdie et al., 2022), and larger damaging earthquakes in the 20th century (Gordon and Lewis, 1980; Allen et al., 2023). The effects of the 1968 Meckering magnitude 6.5 earthquake remain visible in the towns of Meckering and York more than fifty years after this event (Clarke and Edwards, 2018). However, the reason for this seismic activity is not yet well understood. One limitation to developing this understanding

is the low number and sparse coverage of permanent seismic stations across this area.

Given Western Australia's risk and frequency of earthquakes, there is a clear impetus to develop and improve awareness on the part of the emergency manager and community of the people, systems and functions that could be affected by the hazard (exposure) and their susceptibility to injury, harm, damage or loss (vulnerability) to determine the potential impacts (Wehner et al., 2020). DFES, in partnership with Geoscience Australia and the Geological Survey of Western Australia (GSWA), have developed guidance aimed at both the community and emergency management sectors. The 'Western Australia Earthquake Preparedness Guide' is focused on improving earthquake awareness among community, while providing practical information on earthquake safety and what they can do before during and after an event (Fig. 63). Enhanced community awareness is complemented by the development of 'Understanding Earthquakes for Emergency Managers', which is designed to provide emergency managers with the information they need to better understand earthquakes, the risk of one occurring, and what they should do before, during and after an event (Fig. 63). The SWAN project will enhance our understanding of Western Australia's earthquake hazard and enable DFES to enhance sector-wide guidance that improves our state's management of this hazard.

Enhancing our understanding of seismic risk in Western Australia's southwestern region

The temporary deployment of seismic stations under the SWAN project is crucial to comprehending the earthquake

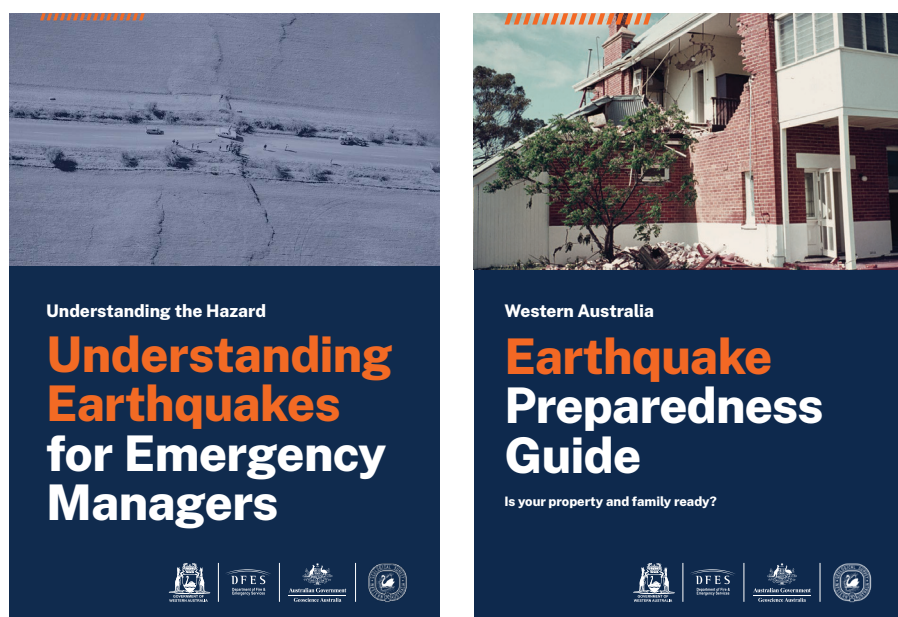


Figure 63. Western Australia's earthquake hazard guidance publications

ground motion hazard and the reasons behind the high seismic rates in southwest Western Australia.

Population centres in southwest Western Australia, such as Geraldton, Perth, Bunbury and Busselton, will benefit from improved hazard forecasts, thanks to a deeper understanding of seismic-wave propagation within this area using the collected data (Miller et al., 2023; Allen, 2024). This, in turn, will contribute to enabling more accurate earthquake hazard assessments. These assessments will inform updated hazard guidance, regional risk profiles and engagement material that improves awareness by emergency managers and community.

The SWAN project has already played an important role in enhancing local awareness of earthquake hazards in Western Australia's emergency management sector. Many of the seismic stations deployed for this project were installed at Volunteer Bush Fire Brigade stations. The installation at a Bush Fire Brigade station near Manjimup in 2020 also served as a 2nd anniversary reminder of the 2018 Lake Muir earthquake (Clarke et al., 2020). This was an important catalyst for the cooperation between Geoscience Australia, the Geological Survey of Western Australia, The Australian National University, DFES, and other affiliated bodies and institutions throughout the SWAN project.

DFES plans to develop additional information and supporting materials, informed by the latest research, to further improve awareness and preparedness. This project has fostered greater involvement in other earthquake-related research activities and established a strong, collaborative network of experts whose knowledge will enhance the emergency sector's ability to respond to earthquakes. This work translates to better on-the-ground awareness for the emergency management sector about the risk of earthquakes, which is crucial for effectively communicating with the community to keep them safe before and after such events. It also means greater confidence in planning for such incidents in the emergency management sector. For earthquake specialists, it provides a greater sense of contribution to the community through the application and dissemination of their important research. Ultimately, this work gives communities a better chance of staying safe.

References

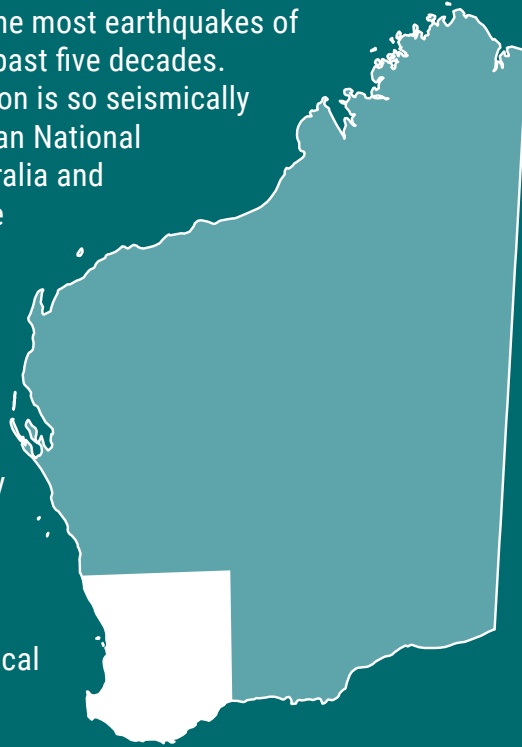
- Allen, TI, Griffin, JD, Clark, DJ, Cummins, PR, Ghasemi, H and Ebrahimi, R 2023, The 2023 National Seismic Hazard Assessment for Australia: model overview: *Geoscience Australia Record* 2023/53, 152p, doi:10.26186/148969.
- Allen, TI, 2024, An updated Fourier spectral attenuation model for southwestern Western Australia, *in* South West Australia Network: passive seismic imaging and hazard analysis *compiled by* RE Murdie and MS Miller: Geological Survey of Western Australia, Report 255, p. 68–75.
- Clark, D and Edwards, M 2018, 50th Anniversary of the 14th October 1968 M_w 6.5 (M_s 6.8) Meckering Earthquake: Australian Earthquake Engineering Society Pre-conference Field Trip, Meckering, 15 November 2018: Geoscience Australia, Record 2018/39, doi:10.11636/Record.2018.039.
- Clark, DJ, Brennand, S, Brenn, G, Garthwaite, MC, Dimech, J, Allen, TI and Standen, S 2020, Surface deformation relating to the 2018 Lake Muir earthquake sequence, southwest Western Australia: new insight into stable continental region earthquakes: *Solid Earth*, v. 11, no. 2, p. 691–717, 27p., doi:10.5194/se-11-691-2020.
- Gordon, FR and Lewis, JD 1980, The Meckering and Calingiri earthquakes October 1968 and March 1970: Geological Survey of Western Australia, Bulletin 126, 229p.
- Miller, MS, Pickle, R, Murdie, RE, Yuan, H, Allen, TI, Gessner, K, Kennett, BLN and Whitney, J 2023, Southwest Australia Seismic Network (SWAN): Recording earthquakes in Australia's most active seismic zone: *Seismological Research Letters*, v. 94, p. 999–1011, doi:10.1785/0220220323.
- Murdie, RE, Pickle, R, Yuan, H, Love, D, Dent, V, Miller, MS and Whitney, J 2022, Observations from the 2022 Arthur River, Western Australia, Earthquake Swarm, *in* 2022 National Conference proceedings, Mount Macedon, Victoria, 24–25 November: Australian Earthquake Engineering Society, 11p.
- SEMC 2017a, Western Australia's Natural Hazards Risk Profile 2017: State Emergency Management Committee, Government of Western Australia.
- SEMC 2017b, Metropolitan Emergency Management Districts Risk Assessment Report: State Emergency Management Committee, Government of Western Australia.
- Wehner, M, Ryu, H, Griffith, M, Edwards, M, Corby, N, Mohanty, I, Vaculik, J and Allen, Y 2020, Earthquake mitigation of WA regional towns York case study: final report: Bushfire and Natural Hazards CRC Report TBC, 190p.

SOUTH WEST AUSTRALIA NETWORK (SWAN):
PASSIVE SEISMIC IMAGING AND HAZARD ANALYSIS

RE Murdie and MS Miller (compilers)

The southwest of Western Australia has had the most earthquakes of any region in continental Australia during the past five decades. To improve our understanding of why this region is so seismically active, a group of scientists from The Australian National University, Geological Survey of Western Australia and Geoscience Australia, in collaboration with the Department of Fire and Emergency Services, deployed a temporary network of seismic instruments for approximately 3.5 years from mid-2020 until late 2023. This Southwest Australia Seismic Network (SWAN) project consisted of a temporary network of 27 broadband seismometers that continuously recorded ground motions from both nearby earthquakes and distant earthquakes.

This report provides descriptions of the data processing, models produced which include local seismicity catalogue, crustal seismic velocity models, and mantle imaging. This research is equally critical from a scientific standpoint and from an emergency management standpoint: it aims to increase our knowledge about Earth's evolution and will ultimately lead to enhanced safety, in terms of earthquake hazard, for the Western Australian community.



Further details of geoscience products are available from:

First Floor Counter
Department of Energy, Mines, Industry Regulation and Safety
100 Plain Street
EAST PERTH WESTERN AUSTRALIA 6004
Phone: +61 8 9222 3626 Email: publications@demirs.wa.gov.au
www.demirs.wa.gov.au/GSWApublications